

The ESO supernovae type Ia progenitor survey (SPY)[★]

The radial velocities of 643 DA white dwarfs

R. Napiwotzki^{1,2}, C.A. Karl², T. Lisker^{2,3}, S. Catalán⁴, H. Drechsel², U. Heber², D. Homeier⁵, D. Koester⁶, B. Leibundgut⁷, T.R. Marsh⁴, S. Moehler⁷, G. Nelemans⁸, D. Reimers⁹, A. Renzini¹⁰, A. Ströer², and L. Yungelson¹¹

¹ Centre for Astrophysics Research, University of Hertfordshire, Hatfield, AL10 9AB, UK
e-mail: r.napiwotzki@herts.ac.uk

² Dr. Remeis-Sternwarte & ECAP, Universität Erlangen-Nürnberg, Sternwartstr. 7, D-96049 Bamberg, Germany

³ Astronomisches Rechen-Institut, Zentrum für Astronomie der Universität Heidelberg, Mönchhofstr. 12-14, 69120 Heidelberg, Germany

⁴ Department of Physics, University of Warwick, Coventry CV4 7AL, UK

⁵ Georg-August-Universität, Institut für Astrophysik, Friedrich-Hund-Platz 1, 37077, Göttingen, Germany

⁶ Institut für Theoretische Physik und Astrophysik, Universität Kiel, D-24098 Kiel, Germany

⁷ European Southern Observatory, Karl-Schwarzschild-Str. 2, D-85748 Garching, Germany

⁸ Institute for Astronomy, KU Leuven, Celestijnenlaan 200D, B-3001 Leuven, Belgium

⁹ Hamburger Sternwarte, Gojenbergsweg 112, 21029, Hamburg, Germany

¹⁰ INAF - Osservatorio Astronomico di Padova, vicolo dell'Osservatorio 5, 35122, Padova, Italy

¹¹ Institute of Astronomy of the Russian Academy of Sciences, 48 Pyatnitskaya Str., 119017 Moscow, Russia

Received ??; accepted ??

ABSTRACT

Close double degenerate binaries are one of the favoured progenitor channels for type Ia supernovae, but it is unclear how many suitable systems there are in the Galaxy. We report results of a large radial velocity survey for double degenerate (DD) binaries using the UVES spectrograph at the ESO VLT (ESO SNIa Progenitor survey – SPY). Exposures taken at different epochs are checked for radial velocity shifts indicating close binary systems. We observed 689 targets classified as DA (displaying hydrogen-rich atmospheres), of which 46 turned out to possess a cool companion. We measured radial velocities (RV) of the remaining 643 DA white dwarfs. We managed to secure observations at two or more epochs for 625 targets, supplemented by eleven objects meeting our selection criteria from literature. The data reduction and analysis methods applied to the survey data are described in detail. The sample contains 39 double degenerate binaries, only four of which were previously known. 20 are double-lined systems, in which features from both components are visible, the other 19 are single-lined binaries. We provide absolute RVs transformed to the heliocentric system suitable for kinematic studies. Our sample is large enough to sub-divide by mass: 16 out of 44 low mass targets ($\leq 0.45 M_{\odot}$) are detected as DDs, while just 23 of the remaining 567 with multiple spectra and mass $> 0.45 M_{\odot}$ are double. Although the detected fraction amongst the low mass objects ($36.4 \pm 7.3\%$) is significantly higher than for the higher-mass, carbon/oxygen-core dominated part of the sample ($3.9 \pm 0.8\%$), it is lower than the detection efficiency based upon companion star masses $\geq 0.05 M_{\odot}$. This suggests either companion stars of mass $< 0.05 M_{\odot}$, or that some of the low mass white dwarfs are single.

Key words. Techniques: radial velocities – binaries: close – binaries: spectroscopic – Supernovae: general – white dwarfs

1. Introduction

Type Ia supernovae (SNe Ia) play an outstanding role in the study of cosmic evolution, for instance, they served as standardizable candles in the studies that led to the discovery of the acceleration of the Universe's expansion (e.g. Riess et al. 1998; Perlmutter et al. 1999). There is general consensus that SNe Ia events are due to thermonuclear explosions in degenerate matter (Hoyle & Fowler 1960). However, the nature of their progenitors, as well as explosion mechanisms and origin of different subclasses still pose serious problems.

Hoyle & Fowler suggested that explosion occurs when a critical mass (likely the Chandrasekhar limit, $1.4 M_{\odot}$) is reached. The most natural candidates for explosions are then white

dwarfs in binaries accreting matter from non-degenerate hydrogen companions via stable Roche-lobe overflow (Schatzman 1963; Wheeler & Hansen 1971; Whelan & Iben 1973) or stellar wind capture (Truran & Cameron 1971; Tutukov & Yungelson 1976). This is the earliest “classical” so-called single-degenerate (SD) scenario.

Another “classical” scenario is the “double-degenerate” (DD) one, in which explosion is, hypothetically, the outcome of the merger of two white dwarfs of (super)-Chandrasekhar total mass (Webbink 1979; Tutukov & Yungelson 1979, 1981; Webbink 1984; Iben & Tutukov 1984). The merger of components is due to the orbital shrinkage because of the loss of angular momentum via gravitational wave radiation and subsequent unstable mass loss. Initially, it was envisioned that the lighter of two white dwarfs fills its Roche lobe first since $R_{WD} \propto M_{WD}^{-1/3}$ and, by virtue of the same $M - R$ relation, in systems with mass ratios $\gtrsim 2/3$, the merger occurs on the dynamical time scale

[★] Based on data obtained at the Paranal Observatory of the European Southern Observatory for programs No. 165.H-0588, 167.D-0407, 71.D-0383, 72.D-0487

(comparable to few orbital periods). The disrupted white dwarf transforms into a “heavy disc” or “envelope” from which the matter accretes onto the central object. This inference was confirmed by Smooth Particle Hydrodynamics (SPH) calculations by Benz et al. (1990) and in many other theoretical studies.

Later, it was realised that the stability of the mass transfer depends also on the efficiency of spin-orbit coupling, which affects the variation of accretion rate as the merger takes place (Marsh et al. 2004). SPH-calculations using a physical equation of state, showed that the lighter component disrupts within about 100 orbital periods and the merger may proceed either via a disk or direct impact, depending on the mass ratio of the components (D’Souza et al. 2006; Dan et al. 2009).

Currently, two possible DD scenarios are commonly discussed. In “violent” (a.k.a. “prompt”) mergers the matter of the lighter WD, may, even before its complete disruption, start to accrete onto the surface of the companion on a dynamical timescale. Detonation is supposed to be initiated in a He+C+O mixture at the interface of the merging white dwarfs. Helium detonation produces a shock wave, which propagates and focusses towards the center of the accretor and results in ignition of carbon and explosion (Livne 1990; Livne & Glasner 1991).

If the explosion does not occur promptly (at lower mass ratios than required for violent merger, see, e.g., discussion by Sato et al. (2016)), an object consisting of a cold virtually isothermal core, a pressure-supported envelope, a Keplerian disc, and a tidal tail forms (Guerrero et al. 2004). A He or C+O mixture may explode in the envelope which is the hottest part of the object and lead to the detonation of carbon at the periphery of the accretor. If two C/O white dwarfs gradually merge, depending on the rate of settling of the envelope matter onto the core, either central ignition of carbon and a SN Ia happens or a neutron star or a massive Oxygen-Neon (O/Ne) white dwarf forms (Nomoto & Iben 1985; Mochkovitch & Livio 1990).

In both varieties of the DD scenario, explosion of the C/O core, which may have a sub- M_{Ch} mass, results in the disruption of the entire configuration. The major fraction of the accretor mass burns to radioactive Ni, which determines the optical luminosity and the spectrum of the SN, while the donor burns to intermediate mass elements which define the observational manifestations of SNe at maximum brightness (Shigeyama et al. 1992; Sim et al. 2010).

An advantage of the DD scenario is that it produces a delay-time distribution (DTD) which overlaps with the Hubble time, while in the SD channel delays are shorter than ≈ 3 Gyr (see, e. g., Yungelson 2010; Bours et al. 2013). If mergers of carbon/oxygen core white dwarf pairs (C/O+C/O), as well as mergers of C/O white dwarf and massive He and hybrid (C/O core + thick He mantle) white dwarfs are taken into account, population synthesis studies can reasonably reproduce the current Galactic SNe Ia rate as well as the slope of their observationally inferred delay time distribution (e.g., Yungelson & Kuranov 2017).

We refer the interested reader for further details concerning evolution of close binaries leading to the formation of progenitors of SNe Ia and the physical processes involved in explosions of SN Ia and their observational manifestations to a number of recent reviews (e.g. Hillebrandt et al. 2013; Postnov & Yungelson 2014; Maoz et al. 2014; Ruiz-Lapuente 2014; Branch & Wheeler 2017; Taubenberger 2017; Livio & Mazzali 2018; Röpke & Sim 2018, and references therein).

The significance of the DD scenario relies upon the existence in nature of a sufficient number of DDs prone to merge and the physical parameters of their components. A given Galactic SN

Ia rate and pre-supernova lifetime implies a specific number of progenitors in the Galaxy. Searches for DDs thus test them as progenitors of Type Ia SNe, but also provide benchmarks for testing the theory of binary star evolution, since in the process of formation, DDs pass through two to four very badly understood stages of common envelope evolution.

The first known DD, L870-2, was discovered by chance in the 1980s (Saffer et al. 1988), but its orbital period of 1.55 days is too long for it to merge within a Hubble time and thus be representative of the putative DD progenitors of present-day Type Ia supernovae, which must have periods of less than 10 to 15 hours. Systematic surveys of the same decade (Robinson & Shafter 1987; Foss et al. 1991) failed to find any DDs among 44 and 25 targets, respectively. A sure-fire DD as well as some candidates were found by Bragaglia et al. (1990) among 54 objects. The (premature) conclusion of these studies was that the space density of DDs was below that required for reproducing the observed rate of SNe Ia. The low masses ($M_{\text{tot}} < M_{\text{Ch}}$) of the confirmed and candidate DDs as well as their long merger timescales were raised as further arguments against the DD scenario.

In the 1990s, more successful targeted searches were made, focusing upon low mass (helium) white dwarfs, which primarily form via binary evolution (Marsh 1995; Marsh et al. 1995; Moran et al. 1997; Maxted et al. 2000b). By the year 2000, around 180 white dwarfs had been checked for RV variations yielding a sample of 18 DDs with $P < 6^{\text{d}3}$ (Marsh 2000; Maxted et al. 2000a). None of the 18 discovered DD systems seemed massive enough to qualify as a SN Ia precursor. However, by this time, theoretical simulations suggested that less than a percent of all potentially observed white dwarfs are close DDs qualifying as SN Ia progenitors (Iben et al. 1997; Nelemans et al. 2001b), and so the failure to find a clear progenitor in 180 white dwarfs is not a surprise.

The observational focus of the 1990s on low mass white dwarfs as more promising targets for DDs worked against the chances of finding potential Type Ia progenitors. Still, given the ubiquity of white dwarfs, the number of DDs found showed that there is a large population of these binaries within the Galaxy. Clearly a definitive test of DDs as SNe Type Ia progenitors requires (a) a larger sample of targets, and (b) one not selected by mass. We therefore embarked upon a large spectroscopic survey of white dwarfs using the UVES spectrograph at the ESO VLT UT2 (Kueyen) to search for white dwarfs and pre-white dwarfs with variable RVs (ESO SN Ia Progenitor survey – SPY). There have been a number of introductory articles to SPY (Napiwotzki et al. 2003, 2001a, 2005) and many results (Napiwotzki et al. 2002; Pauli et al. 2003; Napiwotzki et al. 2004; Nelemans et al. 2005; Koester et al. 2005b; Napiwotzki et al. 2007, to name a few), but there has been no full write-up of the original radial velocity survey. In this paper our aim is to accomplish this for the (majority) hydrogen-atmosphere DA white dwarfs.

Since the completion of the SPY survey, there have been many discoveries of DDs dominated by the light of “extremely low mass” (ELM) white dwarfs (Brown et al. 2010, 2012, 2016a,b), many of which will merge well within a Hubble time (Kilic et al. 2012). These discoveries post-date the SPY survey since ELM white dwarfs were missed in earlier surveys for white dwarfs due to their low gravities which makes them hard to distinguish from early-type main-sequence stars. Some of the ELM binaries host massive white dwarfs hidden in the glare of the ELM components (Kulkarni & van Kerkwijk 2010; Marsh et al. 2011; Brown et al. 2013). If the mass ratio of components in ELM DDs allows stable mass exchange, they will

turn into ultracompact cataclysmic variables of the AM CVn type (Faulkner et al. 1972; Nelemans et al. 2001a). In these systems, the accretors can in principle very occasionally reach the Chandrasekhar mass (Solheim & Yungelson 2005). Otherwise, unstable mass transfer may lead to the merger of components with formation of subdwarf B, subdwarf O or R CrB stars; explosive events are not expected because of the small mass of the donors (Dan et al. 2014).

In this paper we present results of the SPY survey for the radial velocities of white dwarfs spectral type DA (hydrogen dominated spectra). The project was conceived for being operationally (and scientifically) advantageous with observations in service mode at the VLT that could be executed when the telescope would otherwise have been idle (Renzini 1999). Our sample overlaps strongly with the 615 SPY DAs analysed by Koester et al. (2009). Koester et al. performed a model atmosphere analysis of SPY spectra and determined the fundamental parameters effective temperature (T_{eff}) and surface gravity ($\log g$). Our focus is upon radial velocities, but we present additional fundamental parameter estimates to provide a uniform set of data for future comparison with theoretical models. The sample selection for SPY, observations, and data reduction are described in Sect. 2. Our method of RV measurement is outlined in Sect. 3. Sect. 4 presents the results including the detected DDs. In Sect. 5 we discuss our results in the context of previous surveys and implications for the evolution of DDs.

2. Observations and data analysis

2.1. Sample selection

Targets for SPY were drawn from five sources: the WD catalogue of McCook & Sion (1999), the Hamburg ESO Survey (HES; Wisotzki et al. 2000; Christlieb et al. 2001), the Hamburg Quasar Survey (HQS; Hagen et al. 1995; Homeier et al. 1998), the Montreal-Cambridge-Tololo survey (MCT; Lamontagne et al. 2000), and the Edinburgh-Cape survey (EC; Kilkenny et al. 1997). Our selection criteria were spectroscopic confirmation as a white dwarf (at least from objective prism spectra) and $B, V \leq 16.5$ (depending on what information was available) for the region south of $\delta = +15^\circ$. The limit was chosen in order to generate a sample size of order 1000 as thought necessary to uncover a potential SN Ia progenitor (DD with $M_{\text{tot}} \geq M_{\text{Ch}}$, Nelemans et al. 2001b). We extended the survey region later to include the region $+15^\circ \leq \delta \leq 25^\circ$, but imposed a brightness limit of $B, V \leq 15.5$.

The sample of white dwarfs catalogued by McCook & Sion (1999) incorporates various sets plagued with different selection effects. While early surveys for white dwarfs typically based their selection on proper motions (Luyten 1979; Giclas et al. 1978), later catalogues of white dwarfs are usually a waste-product of surveys for galaxies and quasars at high galactic latitude. One important early example is the Palomar-Green survey (Green et al. 1986) which used blue colour besides the galactic latitude as criterion. Similar approaches were used by the MCT and EC surveys mentioned above. Since photographic prism spectra are available for the HQS and HES surveys the presence of strong Balmer lines could be incorporated in the selection process (Christlieb et al. 2001) and the colour criterion could be somewhat relaxed. Other white dwarfs were identified because they showed up in EUV/X-ray surveys (e.g. Pounds et al. 1993). While these approaches have somewhat complementary selection effects, there does remain a significant deficit of white dwarfs in the Galactic plane (Fig. 1). A small selection of

our own was to avoid stars that satisfied our selection criteria but which had already been observed by Maxted et al. (2000a). Three of them ended up being re-observed during our survey, leaving an addition of seven to the SPY sample¹. We account for these stars later when discussing the detection efficiency of the SPY sample.

We had to create a large data base of accurate coordinates and finder charts at short notice to start the service mode observations for SPY. To speed up this process we initially focussed on catalogues with good coordinates and/or good finder charts. Important sources of the SPY observations reported in Koester et al. (2001) and Koester et al. (2009) were the PG, HES, EC, and MCT surveys, which are all biased toward hot objects. Additional sources were the proper motion selected white dwarfs of Giclas et al. (1978, 1980) as catalogued in McCook & Sion (1999). Napiwotzki et al. (2005) reported on results from a “bright” sub-sample of SPY, which covers 93% of all known white dwarfs in the survey area. This sample should be virtually free of any SPY-related selection effects. In Fig. 1 we show the Aitoff projection in galactic coordinates of the DA white dwarfs observed by the SPY project. This figure shows the paucity of white dwarfs in the Galactic plane that we referred to above.

2.2. Observations

Spectra were taken with the UV-Visual Echelle Spectrograph (UVES) of the UT2 telescope (Kueyen) of the ESO VLT. UVES is a high resolution Echelle spectrograph, which can reach a resolution of 110,000 in the red region with a narrow slit (cf. Dekker et al. 2000, for a description of the instrument). Our instrument setup (Dichroic 1, central wavelengths 3900 Å and 5640 Å) uses UVES in a dichroic mode with a 2048 × 4096 EEV CCD windowed to 2048 × 3000 in the blue arm, and two CCDs, a 2048 × 4096 EEV and a 2048 × 4096 MIT-LL, in the red arm. Nearly complete spectral coverage from 3200 Å to 6650 Å with only two ≈ 80 Å wide gaps at 4580 Å and 5640 Å is achieved. In the standard setting used for our observations UVES is operated with an 8'' decker in the blue arm and an 11'' decker in the red arm. The slit was rotated to the parallactic angle.

SPY was implemented as a service mode program. It took advantage of observing conditions which were not usable by most other programs (moon, bad seeing, clouds), and was run when other programs were not feasible. A wide slit (2.1'') was used to minimise slit losses and a 2×2 binning applied to the CCDs to reduce read out noise. Our wide slit reduced the spectral resolution to $R = 18\,500$ (0.36 Å at H α) or better, if seeing disks were smaller than the slit width. Depending on the brightness of the objects, exposure times of 5 min or 10 min were chosen. The S/N per binned pixel (0.044, and 0.032 Å for the blue and red channel respectively) of the extracted spectrum is usually 15 or higher. Due to the nature of the project, two spectra at different, “random” epochs separated by at least one day were observed.

Although our program was carried out during periods of less favourable observing conditions, the seeing was often smaller than the selected slit width of 2.1''. This can, in principle, cause wavelength shifts, if the star is not placed in the centre of the slit. However, since according to the standard observing procedure the star was first centred on a narrow slit before the exposure with the broader slit was started, it can be expected that the star is usually relatively well centred in the slit. We used telluric lines present in the red region of some spectra to estimate the size

¹ WD0401+250, WD0752–146, WD0950–572, WD0954+247, WD0954–710, WD1407–475, WD2151–015

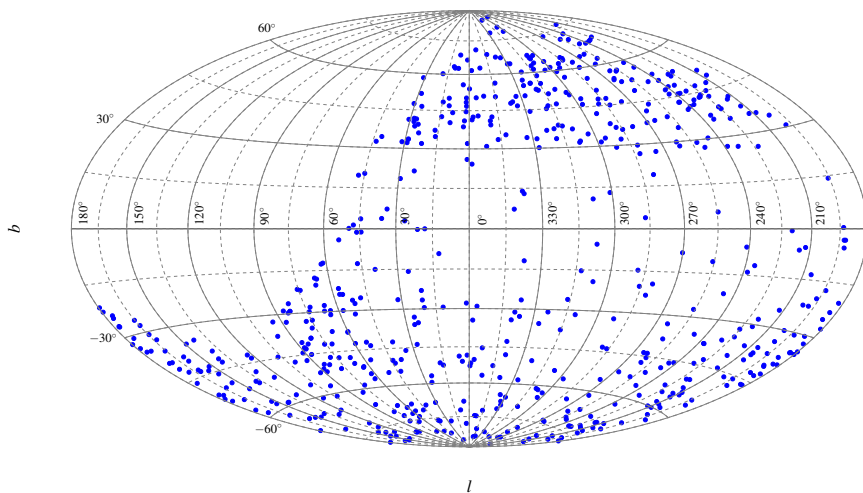


Fig. 1. Aitoff projection in Galactic coordinates of the DA white dwarfs observed by SPY.

of the resulting wavelength shifts (Sect. 2.4) and estimated an additional RV scatter of 0.67 km s^{-1} .

2.3. Data reduction

ESO provided at the time of the SPY observations (commencing in 2000) a data reduction pipeline for UVES, based on MIDAS procedures. The quality of the reduced spectra is in most cases good and we made extensive use of the pipeline reduced spectra for selecting targets for follow-up observations and the model atmosphere analysis of Koester et al. (2001). However, sometimes the reduction pipeline produced artefacts of varying strength, e.g. a quasi-periodic pattern in the red region similar in appearance to a fringing pattern. In a few cases either the blue or the red part of the pipeline reduced spectrum had extremely strong artefacts of unknown origin.

Therefore we created a semi-automatic “SPY pipeline” to perform the final reduction of the spectra. Our procedure makes use of several routines of the “UVES” context of MIDAS, which provides reduction routines adapted for the UVES spectrograph. The reduction is done individually for the blue (3200–4500 Å), lower red (4600–5600 Å), and upper red (5700–6650 Å) region of the spectrum. The position of the individual orders on the CCD is defined automatically tracing the order definition flatfield. However, usually the star is not perfectly centred on the slit along the spatial axis in all wavelength regions. The offset from the centre is determined and accounted for manually, along with the width of the stellar spectrum and the corresponding sky background area.

After accounting for cosmic ray hits and bad CCD pixels, bias and interorder background are subtracted. Wavelength calibration is then performed automatically using the Th-Ar reference spectrum. This is followed by the extraction of one dimensional spectra for each order of the sky background, flatfield, and object frames. For each spectrum, sky background subtraction and flatfielding are performed, and finally the orders are merged. Now, the resulting spectrum is divided by a smoothed spectrum of a DC WD, which by definition shows no spectral features at all and therefore provides an excellent means of correcting for the instrumental response. We checked a number of white dwarfs classified DC for the absence of spectral features even at our high resolution and selected two feature free ones (WD 0000–345 and WD 1520–340).

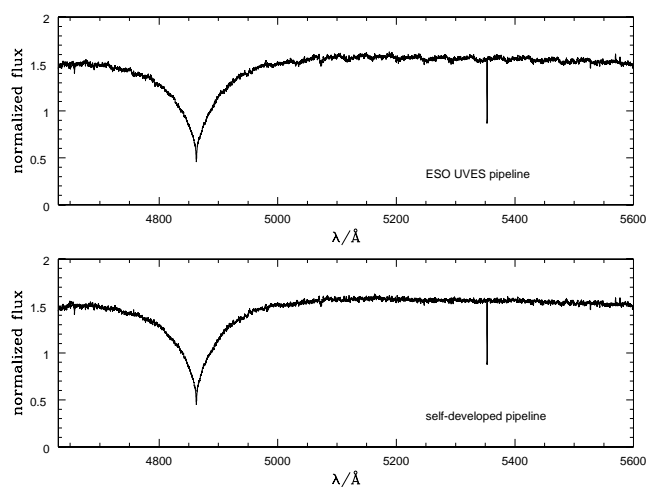


Fig. 2: The ripple problem and its solution. The top spectrum shows the reduced and merged spectrum of a DA WD. It displays a strong quasi-periodic pattern. The lower spectrum resulted after application of our “shift correction”.

A number of merged spectra did not appear smooth, but instead displayed a quasi-periodic ripple pattern over the whole wavelength range or at least over a significant part (Fig. 2). The appearance is similar to the effect mentioned above seen in some of the pipeline reduced spectra. Obviously, this behaviour is due to a mismatch in the flux levels of the corresponding ends of adjacent orders. Such effects should in principle be accounted for by the flatfield division. We do not find a relation as to *when* flatfield division is performed, since the ripples remain unchanged if we first divide the (two-dimensional) object and flatfield frames, and then extract the individual orders. In order to investigate this problem, we chose several stars where the signal-to-noise was large enough that we could extract each order with the width of only one pixel, and still obtain a useful resulting spectrum. The flatfield orders were extracted in the same way, but with an *offset perpendicular to the dispersion direction* (hereafter *separation*). We now went through a range of separations, and found that the ripples first disappear, then appear again with different shape. However, the separation which yields the smoothest spectrum is not always zero and the ideal separation changes with wavelength. To summarise, it is apparent that for each ‘pixel row’ of the two dimensional object spectrum, there is only one flatfield

pixel row which fits ideally, but this can change as one moves along the order.

Given that we do not understand the problem’s cause, it would seem unreasonable to construct a complex algorithm which would take these findings into account. However, without direct relation to the former, we found that the reduction can be improved significantly by *shifting* the flatfield orders with respect to the object orders a few pixels in the dispersion direction (as opposed to the perpendicular separation discussed above). This appears counterintuitive, but it produced the desired result and the practical implementation was easier.

The offset needed changed from night to night and sometimes between spectra taken the same night. This was taken into account in the reduction routine, which automatically went through a range of shift values. We selected spectral regions without strong features. For each shift, the reduced spectrum was fitted by a low-order polynomial, and a χ^2 was computed from the difference between the spectrum and the fit. The best shift was chosen to be the one which led to the lowest χ^2 value. Note that for each star, the shift was computed individually, although it was then applied to the flatfield, which is the same for all stars of one night. We emphasise that this does *not correspond to a real wavelength shift of the spectra*. This is demonstrated by our assessment of the stability of the wavelength scale in the Sect. 2.4.

The procedure outlined above works very well for the DAs (Fig. 2), which are the topic of this article, and for most other white dwarf spectral classes as well. However, for stars of other spectral types, e.g. helium-sdOs which show a large number of spectral lines, the automatic determination of the shift does not yield a useful result because the spectrum is too crowded with features. For these stars we determined the best shift manually by comparing the reduction results for various shifts. The determined shift values show no correlation with quantities like airmass or observing time. Although usually the overall shift varies only slightly during one night, there can be stars with completely different shift values, which do not stand out by position, observing time, or any other quantity. We therefore conclude that the observed effect must be intrinsic to the object frames, not to the flatfield which is only taken once per night. However, we could not identify an obvious reason for the origin of this problem.

We also included the observations from the later run 072.D-0487(A), taken during January, February and March 2004. This last set of data was reduced using the Reflex pipeline (Freudling et al. 2013). Reflex is an environment that was developed to provide an easy and flexible way to reduce VLT/VLTI science data using the ESO pipelines. The output data after using the pipeline are wavelength and flux calibrated spectra. Note that the ripple problem occurs less often in the latest pipelines.

2.4. Telluric lines

A number of telluric absorption features are known in the red spectral range. In the $H\alpha$ region these are mostly caused by water in the atmosphere. Overall Paranal is a very dry place and thus the water features in our UVES spectra are usually weak. However, since the SPY spectra were taken preferentially during periods of relatively poor weather conditions, stronger telluric absorption is present in a number of spectra. Since the RV determination can be skewed if a strong telluric feature coincides with the stellar $H\alpha$ core, we corrected the telluric contribution.

For this purpose we produced a telluric UVES template, which was created from 50 UVES spectra selected from the complete SPY data set of ≈ 2000 spectra on the basis of strong water absorption and simple spectral appearance in the red range. This

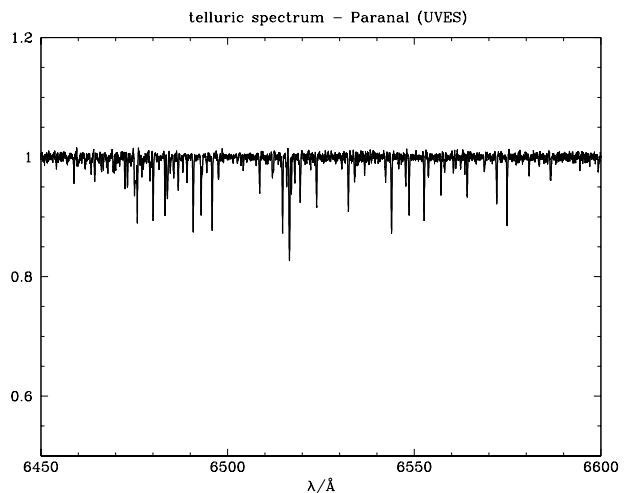


Fig. 3: Telluric template spectrum in the $H\alpha$ region.

included white dwarfs of spectral types DA, DB, DBA, and DC. For each spectrum the local continuum was evaluated in an iterative procedure. The spectra were convolved with a Gaussian of 1 Å FWHM. Data points more than $3\times$ the noise level below the continuum were clipped. This procedure was repeated until the number of clipped wavelength points remained constant. The noise level was estimated from neighbouring featureless parts of the spectra. The inner line cores of $H\alpha$, if present, were excluded by hand. Since the white dwarf sample covers a large range of RVs, this does not produce gaps in the final co-added spectrum. Finally each spectrum was divided by the smoothed continuum. The individual spectra were rebinned to a common wavelength scale and the absorption was scaled to a “normalised telluric absorption strength”. Afterwards all 50 individual telluric spectra were co-added to the template spectrum shown in Fig. 3.

To correct the telluric contamination of the stellar spectra, we measured the strength of the telluric features in the 6450 Å to 6500 Å interval. No sharp stellar lines are present in this range. The template was scaled accordingly and the correction was done by dividing the stellar spectrum by the scaled template.

The presence of telluric lines complicates the analysis of the stellar spectra. However, there is a bright side as well. Telluric absorption lines can be used to measure RV velocities to very high precision (Griffin 1973). We checked the RV stability of the UVES/SPY observations by cross-correlating the template with individual spectra with strong telluric features. The resulting scatter is equivalent to $\pm 0.67 \text{ km s}^{-1}$ indicating good stability; this number was added in quadrature to the radial velocity uncertainties described in the next section when it came to judging evidence for radial velocity variability.

3. Radial velocity measurement

The radial velocities (RVs) of DA can be most accurately measured from the sharp line cores of the Balmer lines. These are most pronounced in $H\alpha$, and to a lesser extent in $H\beta$ (Fig. 4). These line cores are formed in high layers of the stellar atmosphere, where the density is low and pressure broadening small². The low densities allow the occupation numbers

² Halenka et al. (2015) carried out theoretical calculations and claimed that pressure shift can mimic RV shifts of tenth of km s^{-1} , if the inner line wings of $H\beta$ are measured. The authors found negligible effects

to deviate from local thermal equilibrium (LTE) and allow for NLTE effects, which are responsible for the strength of the cores (Greenstein & Peterson 1973). Since most white dwarfs are slow rotators (Koester & Herrero 1988; Heber et al. 1997b; Koester et al. 1998), the line cores are basically Gaussian with widths corresponding to the temperature in the formation layer.

Radial velocities of stars are often measured using cross-correlation algorithms. Observed spectra are correlated against model spectra or observed template spectra. The advantages of this method are the flexibility and its straightforward usage. As discussed in Napiwotzki et al. (2001a), the broad line wings of the Balmer lines cause complications if the traditional cross-correlation method is applied to white dwarfs. Thus we developed a modification of the cross-correlation method, which is based on a χ^2 test (Napiwotzki et al. 2001a) and measured the relative RV shifts between the observed spectra. This proved to be a quick and flexible way to select RV variable stars for follow-up observations (e.g. Napiwotzki et al. 2001b). However, experience showed that this method has its drawbacks (error estimates are not always reliable and sometimes spurious results are produced, especially for stars with weak line cores), and thus we developed more sophisticated methods for the final analysis. Another motivation for a different approach to the RV measurements was our interest to use the absolute RVs for a study of the space velocities of the white dwarfs in the SPY sample (Pauli et al. 2003, 2006; Richter et al. 2007).

Several investigations (Saffer et al. 1988; Foss et al. 1991; Marsh et al. 1995; Maxted & Marsh 1999) modelled the line profiles with Lorentzians or Gaussians. However, these functions describe the line profiles only approximately and combinations of three or four functions can be necessary for an accurate modelling (Maxted & Marsh 1999). Model atmosphere line profiles on the other hand can reproduce the observed Balmer lines of DA white dwarfs quite accurately (Heber et al. 1997b), if the NLTE effects are taken into account. Koester et al. (2001) determined fundamental parameters of about 200 white dwarfs observed during the first nine months of the SPY observations, 163 of them of spectral type DA (compiled in their Table A.1). Koester et al. (2009) obtained the parameters of a much larger sample (including 615 DA white dwarfs). Thus, all the necessary information to apply line profile fits is available for our sample.

3.1. Model atmospheres

Radial velocities are derived by fitting the profiles of the $H\alpha$ and $H\beta$ Balmer lines with model spectra and computing the optimum RV. In the few cases with a clear detection of photospheric Ca II H&K lines, these were also included. White dwarfs with temperatures above 20 000 K were analysed with the grid of self consistent pure hydrogen NLTE model atmospheres for DA white dwarfs of Napiwotzki et al. (1999). Cooler white dwarfs were analysed with the grid described in Koester et al. (1998). These model spectra used NLTE line formation physics as applied to the LTE atmosphere models of D. Koester.

Fundamental parameters are derived from the spectral analysis of the complete Balmer series as described in Koester et al. (2009) for the SPY DA sample. The input physics of the model grids used for determining the RVs is not exactly the same as for the models used for the Koester et al. (2009) analysis. Thus we redetermined the fundamental parameters temperature and gravity with the grids actually used for the RV measurement and the

for $H\alpha$. Our empirical test presented in Appendix A indicates a much smaller effect, if present at all.

fitting programme FITSB2 described below. This ensures that the fitting process is self-consistent.

In the case of double-lined systems, temperatures and gravities of both components were determined. This was an iterative process with a first fit carried out using first guess RVs. The estimated fundamental parameters were then used for determining RVs from fitting the $H\alpha$ and $H\beta$ lines. These initial estimates were refined by refitting temperature/gravity and RVs until parameter changes in subsequent steps became negligible. Model spectra for the two parameter sets were coadded after scaling them accordingly using the mass-radius relations derived from the tracks of Benvenuto & Althaus (1999) complemented by the Hamada & Salpeter (1961) zero temperature models for the highest masses. During these fits, the white dwarf mass-radius relation was used as a constraint to reduce parameter degeneracy.

3.2. FITSB2 and the fit process

The programme FITSB2 can fit line profiles and measure RVs. It was originally developed to analyse the spectra of double-lined (SB2) systems, but can be applied to spectra of single-lined systems (RV variable or not) as well.

The basic philosophy for fitting line profiles follows the FITPROF program described in Napiwotzki et al. (1999). Both, the observed and theoretical Balmer line profiles are normalised to the local continuum in a consistent manner. Wavelength shifts are calculated for the actual RV estimate for each spectrum. The synthetic spectra are convolved to the observational resolution with a Gaussian and interpolated to the actual parameters with bi-cubic splines and interpolated to the observed wavelength scale.

Parameters are determined by minimising χ^2 . The optimisation is done by means of a simplex algorithm, which is based on the AMOEBA routine of Press et al. (1992). The advantages of this approach are a high degree of stability and flexibility. New functions and parameters can be easily integrated. One disadvantage is that the convergence of simplex algorithms is not very fast and thus CPU time intensive. However, in practice this is not a major limitation for line profile fitting with FITSB2.

FITSB2 offers a number of options for fitting line profiles: model spectra, Gaussians, Lorentzians, and polynomials or a combination of these four. Most white dwarf spectra were simply fitted using model profiles calculated for the appropriate parameters. The default fit interval was $\pm 15 \text{ \AA}$ relative to the line centre. However, sometimes it was appropriate to use larger wavelength intervals. The intervals were adjusted according to the measured RVs. In a number of cases the model line profiles did not give a satisfactory fit of the observed spectra, potentially compromising the accuracy of the measured RV. If that happened Gaussians, Lorentzians and/or polynomials were used to improve the fit; see Sect. 4 for a discussion and examples.

Our observational set-up results in vastly oversampled spectra. Moreover, Doppler broadening results in a substantial broadening of the NLTE line cores of the $H\alpha$ and $H\beta$ (the Doppler width of $H\alpha$ at 10 000 K is 2.2 \AA). This allowed us to use a simple method to estimate the local noise. A moving parabola was fitted to 20 pixels and the standard deviation computed. This was repeated for all pixels. Afterwards, the pixel by pixel standard deviations were smoothed by a 50 pixel boxcar.

Radial velocity errors were calculated using bootstrapping. This method randomly selects N points of the N points of the observed spectra. Points can be selected more than once, which has

the effect that on average $1 - e^{-1}$ points of the original spectrum are represented in the new spectrum. Radial velocities are re-fitted using the bootstrapped spectrum. This process is repeated and the errors are computed from the standard deviation of the derived parameters. Error estimates using bootstrapping are better at taking into account uncertainties resulting from imperfections of the input data (e.g. hot or dead pixels) and non-Gaussian noise than standard estimates from the co-variance matrix.

Error estimates from bootstrapping are subject to statistical fluctuations and a sufficient number of bootstraps need to be done. The bias-corrected three step method of Andrews & Buchinsky (2000) is applied to estimate the number of necessary iterations. We required that the probability of the error estimates being wrong by more than 10% is less than 1%. The number of bootstraps depends on the distribution of bootstrapped parameters with long tails requiring more bootstrap steps to achieve the required accuracy. Our accuracy requirements resulted in a minimum of 332 bootstraps. Note that the parameters describing Gaussians, Lorentzians and polynomials modifying the model spectrum are treated as free parameters and thus enter the error budget.

4. Results

Survey spectra were taken for a total of 689 targets classified as DA. It turned out that the spectra of 46 stars revealed the presence of red companions (Koester et al. 2009), almost all M type main sequence stars, but also at least one brown dwarf (Maxted et al. 2006). The DA+dM nature of most of these targets was not known at the time they were scheduled for observations. For many of the white dwarfs only low quality classification spectra of the blue range existed, which did not allow the detection of the cool companion.

A further 18 targets could not be checked for RV variations, because only one spectrum was taken, leaving 625 white dwarfs we could analyse for RV variations and the presence of a compact companion. Our RV measurements of the 643 DAs without a cool companion are summarised in Table B.1. We applied heliocentric corrections to the velocities, but no corrections for gravitational redshift. The latter can exceed 100 km s^{-1} for high mass white dwarfs and need to be taken into account when calculating space velocities, but in this study the emphasis is on velocity variations.

We used the same criterion for variability as used by Maxted et al. (2000a). For each star a weighted mean of the RVs is computed. We then calculate χ^2 from the deviations of the individual RVs from the mean. χ^2 measures the goodness of fit of the “model assumption” of a constant RV. The comparison with a χ^2 distribution with the appropriate number of degrees of freedom yields the probability p of obtaining the observed value of χ^2 or higher from random fluctuations. The computed values of χ^2 and $\log p$ are tabulated in Table B.1 and the distribution of $\log p$ is displayed in Fig. 5. We chose a detection threshold of $p < 10^{-4}$, i.e. white dwarfs with p values below this value are considered to be binaries (indicated as “DD”) in Table B.1. This limit corresponds to 0.1 expected false detections due to random chance in the complete SPY sample of ≈ 1000 white dwarfs and pre-white dwarfs. Two targets, WD0032-317 and WD1241-010, have $p < 10^{-3}$, indicative of a higher-than-average chance of their being binaries, but do not meet our $p < 10^{-4}$ criterion. WD1241-010 is in fact a known DD (Marsh et al. 1995); WD0032-317 could reward future study. Three targets did not show RV variations exceeding our detection threshold, but visual inspection identified them as double-lined systems, consist-

ing of two white dwarfs. They are indicated by “dd” in Table B.1. See Sect. 4.4 for a discussion of individual objects identified this way.

When a combination of model atmosphere spectra with Gaussians, Lorentzians, and/or polynomials is used for the line profiles fitting this is marked in the comments column of Table B.1. See Sect. B for a detailed description of the table.

4.1. Peculiarities

As stated above, the fits of the $H\alpha$ and $H\beta$ line make use of model atmosphere profiles. These are computed for the fundamental parameters derived from the fit of the entire Balmer line series as outlined in Koester et al. (2009). Thus in an ideal world the only free parameters during the fitting procedure would be the RVs. This worked well for about half of the programme stars (e.g. for HS 0002+1635 in the top left panel of Fig. 4). However, the fit between observed and synthetic line profiles was less than perfect for very hot and for cool white dwarfs.

Very hot white dwarfs. The hottest stars in the SPY sample displayed stronger emission cores than predicted by the models (example WD 2146–433; Fig. 4, top right). The problems are probably explained by the presence of metals in the atmosphere, which modify the atmospheric structure and thus the line profiles (Werner 1996). However, Latour et al. (2015) report that discrepancies still persist, if the correct abundances are adopted for model calculations and a good fit can only be achieved with arbitrarily increased abundances. We took the pragmatic approach of amending the cores of our model spectra by adding Gaussians and/or Lorentzians to achieve a good fit.

Cool white dwarfs. Many cool DAs showed broader and stronger line cores than predicted by the models (e.g. WD 0126+101; Fig. 4, bottom left). Koester et al. (1998) reported on the presence of flat bottom profiles of the cores of $H\alpha$ for pulsating white dwarfs of the ZZ Ceti type. The reason for these flat cores is very likely the velocity field associated with the pulsations (Koester & Kompas 2007). Similar and even stronger effects are present in our sample for a number of cool white dwarfs outside the ZZ Ceti instability strip (WD 0126+101 has a temperature of 8557 K; Koester et al. 2009). One can speculate that the reason of this discrepancy are violent convective motions in the atmospheres as seen in hydrodynamic models (Tremblay et al. 2013a).

A more detailed comparison with models could give interesting insights, but here we took again a pragmatic approach and combined the model atmosphere spectra with Gaussians, Lorentzians, and/or polynomials to achieve a good fit of the line cores.

Magnetic white dwarfs. The SPY sample includes ten magnetic white dwarfs, most of them new discoveries based on the Zeeman splitting of the Balmer lines (Koester et al. 2009). Our model spectra do not include the effects of magnetic fields. We simply modelled the observed spectra as well as possible using combinations of Gaussians and Lorentzians (see WD1300–098; Fig. 4, bottom right). This is a rather crude and unphysical approach, but once a good reproduction of the line profiles is achieved, accurate RV velocities can be measured. Note that the absolute velocities measured this way, should be treated with caution. For that the measurements should be repeated with a

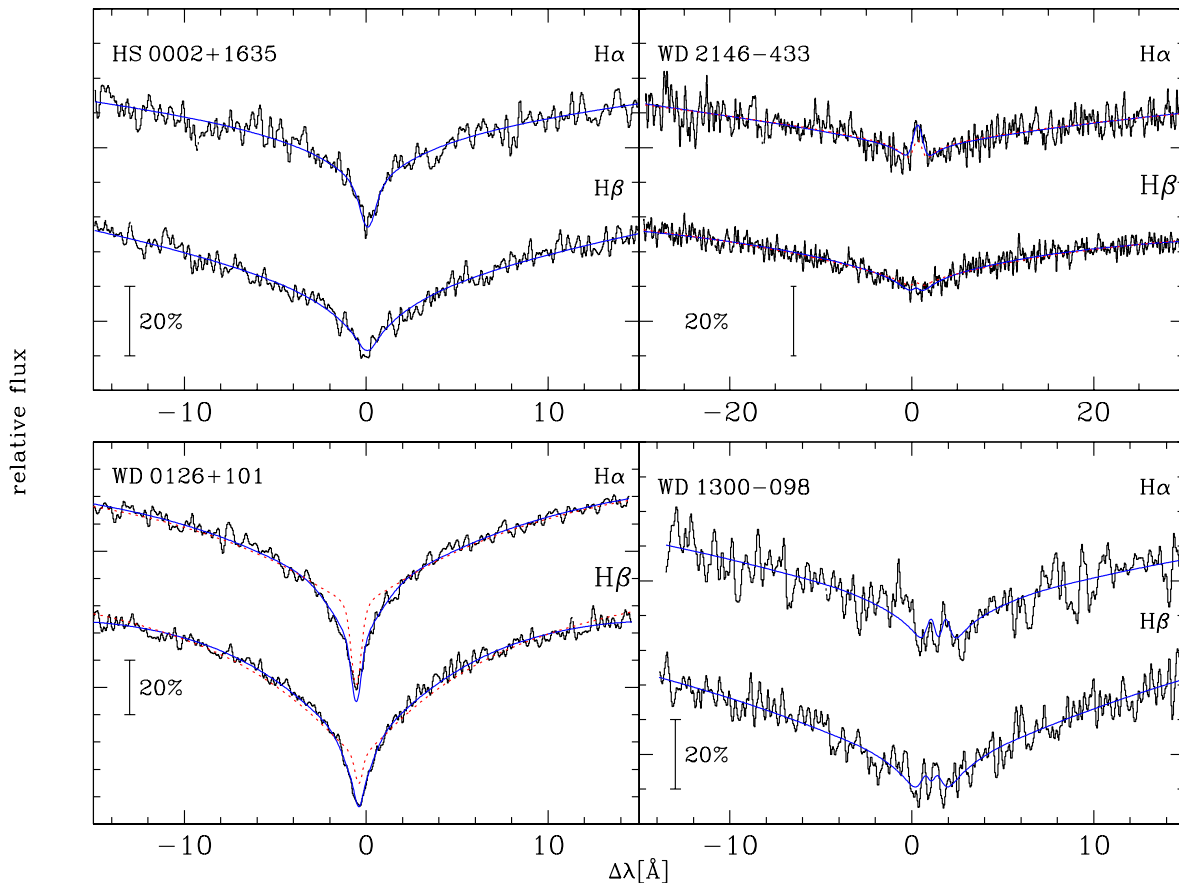


Fig. 4: Observed $H\alpha$ and $H\beta$ profiles compared to the fitted model spectrum. The graph shows one observed spectrum for each binary and the best fitting model spectrum (blue smooth line). Here and in the following figures we display the observed spectra smoothed with a Gaussian of 0.15 \AA FWHM, hardly affecting the spectral resolution. $\Delta\lambda$ is the wavelength offset relative to the laboratory wavelengths of $H\alpha$ and $H\beta$, respectively. *Top left*: HS 0002+1635, fitted with model spectra without modifications. *Top right*: WD 2146-433, a hot DA with a Gaussian added to better reproduce the central emission core (model spectrum without correction shown as dashed red line.) *Bottom left*: WD 0126+101, one of the cool DAs displaying a broader and stronger central core than predicted by the models (model spectrum without correction shown as dashed red line.). *Bottom right*: WD 1300-098, one of the magnetic white dwarfs.

proper treatment of the magnetic fields. None of the magnetic white dwarfs displayed any RV variation.

Spectral types DAB and DAO. Four of the white dwarfs in our sample are of spectral type DAB and two of spectral type DAO (HE 1106-0942³ and WD 1305-017) showing lines of He I or He II, respectively in addition to the hydrogen lines. We used NLTE atmospheres computed for a mix of hydrogen and helium for analysing the DAOs.

HS 0209+0832 is a genuine DAB white dwarf showing helium line profile variations (Heber et al. 1997a). Two other DABs (WD 0128-387 and WD 0453-295) were analysed by Wesemael et al. (1994), who showed that a consistent fit of lines and spectral energy distribution is only achievable with a composite spectrum combining a hydrogen-rich and a helium-rich WD. Similarly, Bergeron & Liebert (2002)

³ This star is amongst the hottest and is the most luminous star in our sample. Stroeger et al. (2007) classified it as a subluminescent O star (sdO) and derived atmospheric parameters similar to those listed in Table C.2.

found WD 1115+116 to be a DA+DB double-lined binary system from a model atmosphere analysis. This was confirmed by Maxted et al. (2002)'s measurement of a 30 day orbital period, the longest measured for any DD. A detailed decomposition of the spectrum is beyond the aims of this investigation and the He I lines are weak. We fitted the hydrogen-rich component with a DA model atmosphere and used Gaussians to fit He I lines. We included only the 4713.3 \AA , 5015.7 \AA and 5875.8 \AA lines not displaying strong forbidden components. Results for the DABs will be discussed in Sect. 4.4.

4.2. Detection efficiency

The mean detection efficiency of the SPY sample is plotted in Fig. 6. For each star observed, the detection probability was evaluated as a function of orbital period using the same times and radial velocity uncertainties as observed along with the 0.67 km s^{-1} uncertainty added in quadrature that we discussed earlier. The probabilities were obtained by calculating the critical orbital inclination i_c for which our $\log p = -4$ threshold was met, and

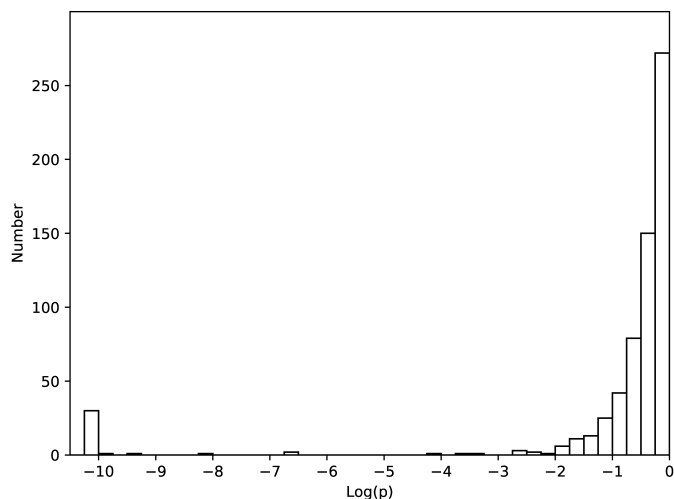


Fig. 5: Distribution of $\log p$ from Table B.1. The peak on the right represents statistical noise only. Our detection threshold is $\log p < -4$. Two systems have $-4 < \log p < -3$; the bin at $\log p = -10$ summarises all objects with $\log p \leq -10$; many of them have $\log p$ much less than this value.

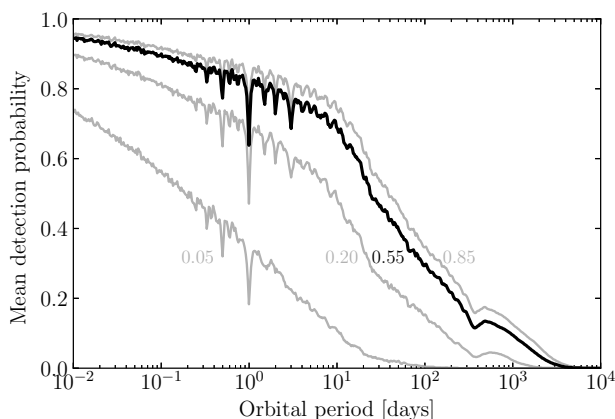


Fig. 6: The mean detection efficiency of the 632 targets with more than one RV in our sample as a function of orbital period, including 7 additional targets from Maxted et al. (2000a) that satisfy the SPY survey criteria. Dips in efficiency at e.g. $P = 1$ d correspond to typical time intervals between exposures. The calculations account for randomly inclined orbits and orbital phases and were based on the assumption that the visible white dwarf has a mass of $0.55 M_{\odot}$ and companion masses of 0.05 (brown dwarf), 0.20 (ELM), 0.55 (typical white dwarf) and $0.85 M_{\odot}$ (Chandrasekhar mass system) as indicated on the plot.

then using $P(i \geq i_c) = \cos(i_c)$ on the assumption of randomly inclined orbits. Random orbital phase offsets were accounted for by averaging over a uniform grid of 20 initial orbital phases in each case. We included the radial velocities measured by Maxted et al. (2000a) for 10 targets that fulfil the SPY criteria but which we had excluded from the survey because of the earlier study. Three of these targets were in fact re-observed in SPY and so the combined datasets were used for these. The remaining seven were a small addition to overall sample, to give a total of 632 targets.

The detection probability of a given DD depends upon the masses of the component stars. We assumed a mass of $M_1 = 0.55 M_{\odot}$ for the dominant primary star, while the assumed companion mass M_2 differentiates the different lines plotted in Fig. 6; the lines shown are invariant for constant values of $M_2^2/(M_1 + M_2)^2$. The key point of the plot is that SPY has good sensitivity over all of the known range of DD orbital periods. For typical orbital periods of DDs of around a day and normal mass white dwarf companions, the detection probability is of order 80%, while it exceeds 90% for periods of a few hours or less. The high precision of the SPY velocities means that there is even significant sensitivity to orbital periods as long as 100 days or more. Low mass companions cause lower amplitude RV changes, and so the detection probability drops significantly for brown dwarf mass companions ($M_2 \sim 0.05 M_{\odot}$), but, since all known examples of unresolved white dwarf/brown dwarf binaries are of short period (Parsons et al. 2017), ~ 10 hours or less, SPY has significant sensitivity to such systems as well. Calculations such as those of Fig. 6 could be used to correct for DDs missed in SPY (WD1241-010 is one such system; Marsh et al. 1995), but we refrain from doing this as the correct approach is a more nuanced multi-dimensional problem that allows for multiple selection effects when comparing theoretical and observational populations, which we discuss in more detail in Section 5.2.

4.3. DA white dwarfs with Ca II lines

A number of DA white dwarfs observed by SPY display Ca II absorption lines (Koester et al. 2005b) and are thus of spectral type DAZ. The most prominent features are the Ca II H and K resonance lines. These lines are much narrower than the H α and H β Balmer lines used by us and the Ca K line is well suited for accurate RV measurements. The other component of the doublet, Ca H, is usually too strongly disturbed by the near-by strong He I line to be useful.

The Ca II lines are broadened by quadratic Stark (and eventually neutral) broadening, which both lead to small asymmetries and line shifts. This could be a potential problem in particular, when lines are very strong, but if χ^2 is small then we can be confident that the impact is too small to make a noticeable effect.

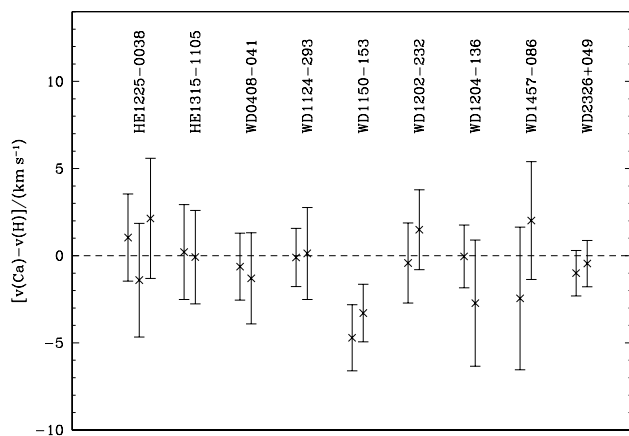
Nine of the DA white dwarfs of the sample presented show detectable Ca II lines of photospheric origin. This was established by Koester et al. (2005b) from a comparison of the RV measured from the calcium lines and the Balmer lines. Interstellar Ca lines are present in the spectra of some hotter white dwarfs.

Here we will use the photospheric Ca lines to check the internal consistency of the RV measurements. While the H α and H β lines are registered with the two CCDs in the red channel of UVES, the Ca K lines are observed with the third CCD in the blue channel. CCD specific problems or systematic errors during the spectral reduction process and RV measurement should show up in a comparison.

Results for the Ca K line and the corresponding Balmer line measurements are listed in Table 1 and a plot of the resulting differences is shown in Fig. 7. The agreement is very good. Only two values out of the 19 in Fig. 7 show deviations exceeding the 1σ limits computed from the individual error limits. The resulting reduced χ^2 amounts to 0.72, well in agreement with purely statistical scatter. We conclude that SPY was routinely able to measure radial velocities of white dwarfs at the few km s^{-1} level, and, on brighter targets, to well below 1 km s^{-1} .

Table 1: Radial velocities $v(\text{Ca})$ measured from photospheric Ca K lines compared to the Balmer line values $v(\text{H})$.

object	date	UT	$v(\text{Ca})$ km s ⁻¹	$v(\text{H})$ km s ⁻¹
WD 0408–041	15/09/00	09:28	19.2±1.5	19.8±1.3
	02/09/01	09:17	17.4±2.0	18.7±1.7
WD 1124–293	23/04/00	03:55	29.4±1.5	29.5±0.7
	17/05/00	02:07	29.3±2.2	29.2±1.5
WD 1150–153	23/04/00	04:27	23.7±1.1	28.4±1.5
	19/05/00	01:23	19.3±0.9	22.6±1.4
WD 1202–232	23/04/00	04:44	22.6±2.3	23.1±0.3
	17/05/00	03:08	25.1±2.3	23.6±0.4
WD 1204–136	23/04/00	04:54	37.5±1.1	37.5±1.4
	17/05/00	03:31	35.3±1.7	38.1±3.2
HE 1225–0038	22/04/00	02:44	11.6±2.4	10.6±0.7
	17/05/00	03:44	10.7±3.0	12.1±1.4
	04/07/00	23:28	13.2±3.4	11.1±0.6
HE 1315–1105	23/04/00	01:30	32.1±2.5	31.9±1.0
	19/05/00	03:08	31.4±2.3	31.5±1.3
WD 1457–086	13/07/00	04:07	20.5±3.6	22.9±2.0
	16/07/00	02:03	21.4±3.0	19.4±1.6
WD 2326+049	06/08/00	04:18	43.4±0.7	44.4±1.1
	17/09/00	04:02	39.3±0.5	39.8±1.2

Fig. 7: Differences between $v(\text{Ca})$ and $v(\text{H})$ for the individual spectra as listed in Table 1. Error limits are computed by combining the error estimates for the lines in quadrature.

4.4. Double degenerates

Our RV measurements are summarised in Table B.1. RV variable DDs are indicated by “DD”. We detected a total of 39 DDs (see Table 2 for more details). Of these, 19 are single-lined (SB1) and 20 double-lined (SB2). For ten of the SB2 systems radial velocity curves have been measured and masses of the components derived. Ten SB2 systems are still awaiting follow-up spectroscopy. Similarly, for nine SB1 systems radial velocity curves have been measured and minimum masses of the components derived. Four of these DDs have been published in previous works not related to SPY, while three others have orbits presented in papers unrelated to SPY but subsequent to their detection as DDs in SPY – see Table 2 for references.

Fig. 8 shows the distribution of our white dwarf sample in the $T_{\text{eff}}/\log g$ plane with single white dwarfs shown in the upper

panel and DDs shown in the lower panel. The atmospheric values have been taken from Koester et al. (2009). For $T_{\text{eff}} < 12\,500$ K the values of $T_{\text{eff}}/\log g$ from 1D models are not accurate and hence we applied the corrections between 1D and 3D models of Tremblay et al. (2013b) for a mixing length parameter $ML2/\alpha=0.6$, which is the value used in the Koester models.

4.4.1. Double-lined systems

In Fig. 9 we show spectra of 18 of the 20 double-lined DDs found in the survey, excluding only the two DAB white dwarfs, WD0128-387 and WD1115+166, which we discuss below. Double-lined systems are of particular interest since, once fully characterised, they deliver mass ratios and fundamental parameters for both stars and thus are of special importance for the understanding of the prior evolution of the systems. We now discuss special cases.

WD 2020–425: The spectrum shown in Fig. 9 appears to show only the $H\alpha$ core of one object. However, comparison of the two spectra taken at different epochs (Fig. 10) demonstrates the existence of a second component. This white dwarf is in the parameter range described before (Sect 4.1), in which $H\alpha$ has neither an absorption nor an emission core. WD 2020–425 has parameters, which make it a possible SN Ia progenitor (Napiwotzki et al. 2005). Its period is short enough to let it merge within a Hubble time and the combined mass of both white dwarfs is very close to the Chandrasekhar limit. However, the lack of a sharp core of the second, high mass, white dwarf results in relatively high uncertainties, so that a mass below Chandrasekhar can not be ruled out.

HS 0237+1034 No second epoch survey spectrum exists for HS 0237+1034. However, it is a double-lined DD consisting of two DA white dwarfs (Fig. 9).

MCT 0136–2010: Two spectra were taken for this target. The RV shift measured between the two spectra is not significant. The reason for us to classify it as DD is its double-lined spectrum. This is not too obvious at a first glance at Fig 9. However, the two spectra taken at different epochs (Fig. 11) are clearly different and the χ^2 difference between a fit with and without a second component is 130.5, highly significant. Figure 11 shows the $H\alpha$ profile fitted with a single model.

The small RV offsets in both epochs makes a small RV amplitude and thus a long period likely. Although it is thus unlikely to qualify as SN Ia progenitor, it appears to have a high mass. The fundamental parameters derived by Koester et al. (2009) from a single-lined fit are $T_{\text{eff}} = 8416$ K and $\log g = 8.405$, making it an interesting object for further follow-up.

Spectral types DAB and DAO: Two of the DABs (WD 0453–295 and WD 1115+166) show large RV variations and are clearly short period DDs. The spectrum of WD 0453–295 shows two $H\alpha$ components making this a DA+DBA binary. No second $H\alpha$ component is visible in WD 1115+166 and it is thus a DA+DB binary, in agreement with the detection of the binary period and anti-phased motion in the hydrogen and helium lines by Maxted et al. (2002). The RV shift measured for WD 0128–387 has barely 1σ significance. However, we noted that in our spectra the He I lines of the DB com-

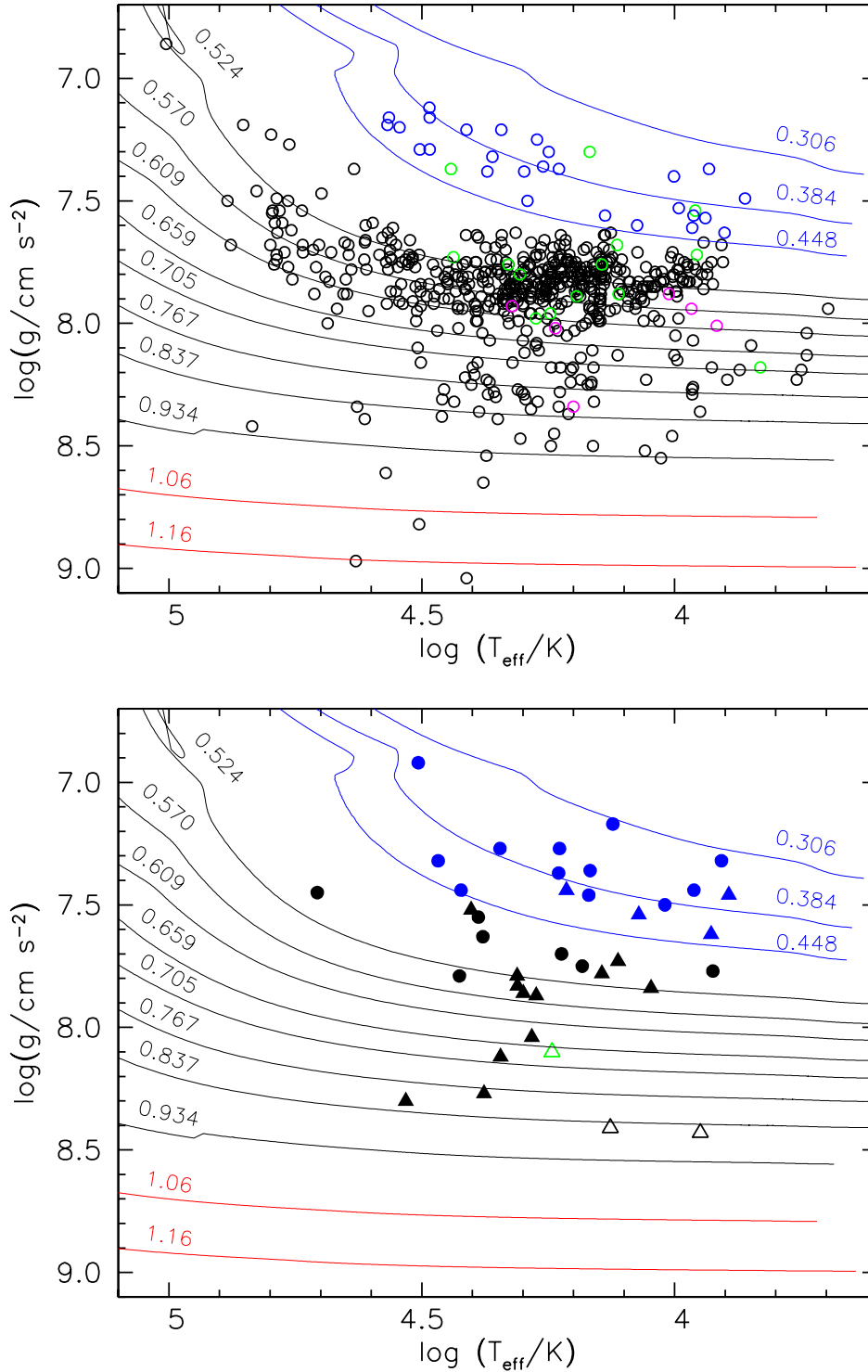


Fig. 8: Comparison of the SPY sample to evolutionary tracks for He-core (blue, Panei et al. 2007), C/O core (black, Renedo et al. 2010) and O/Ne core white dwarfs (red, Althaus et al. 2005) in the $T_{\text{eff}} - \log g$ plane. The tracks are labelled with their mass. Upper panel: Position of all stars in Table C.2 excluding the DD white dwarfs and stars without a mass determination. Magnetic white dwarfs are shown in magenta, those with only one spectrum in Table B.1 in green. The hot, low gravity star HE1106–0942, the high gravity DA WD0346–011, and the magnetic, high gravity DA WD2051–208 are off-scale. Lower panel: same for DDs. SB1 systems (19) are shown as filled circles and SB2 systems (19) as triangles; the SB2 WD0135-052 is not shown as we were not able to determine masses for it. Filled triangles mark systems that are RV variable, while open ones label SB2 systems that were found by visual inspection of their spectra, but are not considered RV variable (WD0128–387 and MCT0136–2010) or where only one spectrum was taken (HS0237+1034). The parameters of the brighter component were used. The gravity of HE0225–1912 has been offset by -0.05 dex to improve visibility.

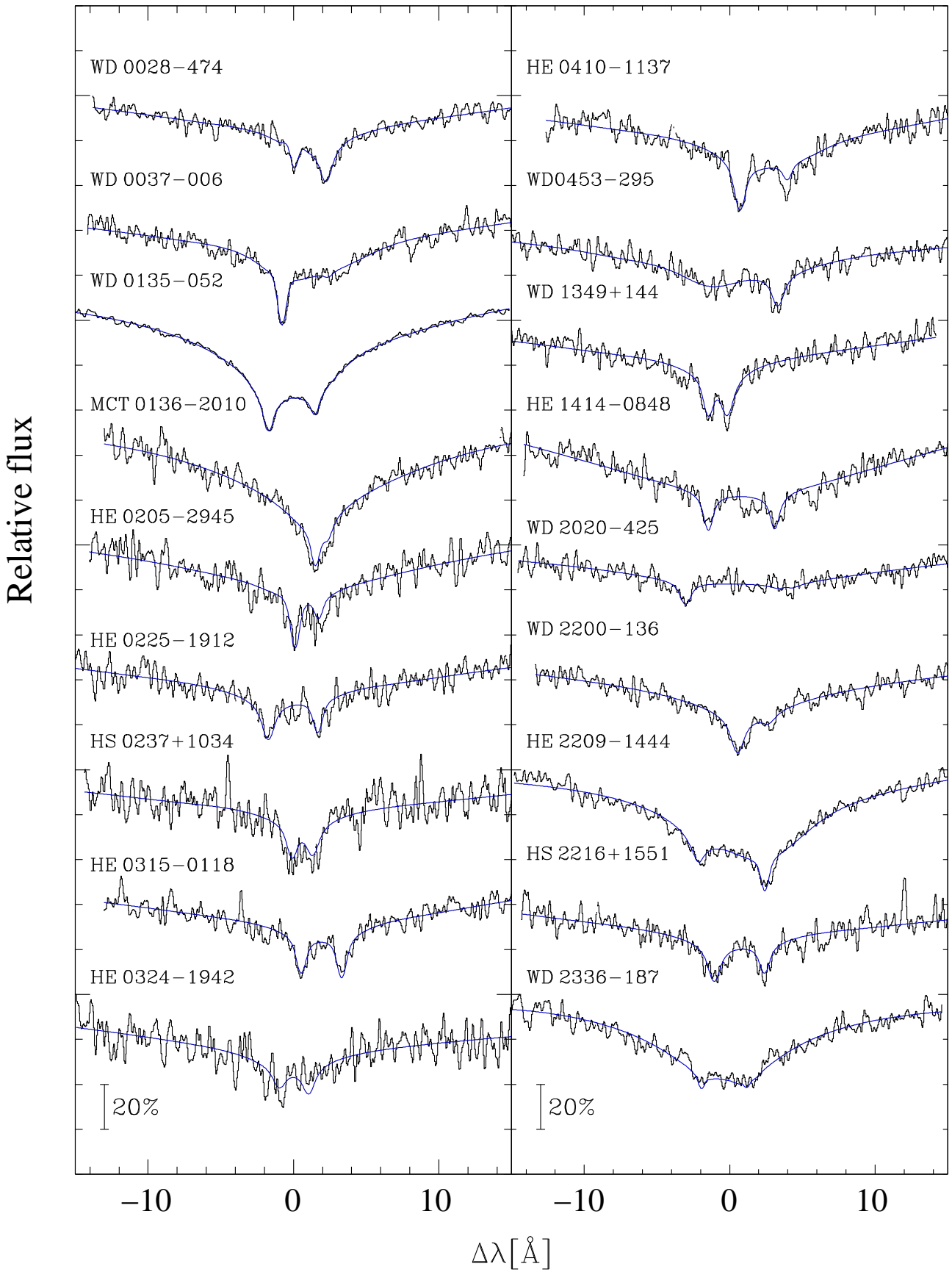


Fig. 9: $H\alpha$ region of 18 of the 20 the double-lined systems detected in the survey. Each system shown displays two $H\alpha$ cores; the two systems excluded, WD0128-387 and WD1115+166, are DABs and show only a single component at $H\alpha$. The figure shows one observed spectrum for each binary along with the best fitting model spectrum (blue smooth line). The observed spectra were smoothed with a Gaussian with 0.15 Å for display. $\Delta\lambda$ is the wavelength offset relative to the laboratory wavelength of $H\alpha$.

Table 2: List of the DDs identified in this survey. References are provided for those that have previously been identified as DDs, in many cases from the SPY survey. The mass of the primary M_1 is given (see appendix C). M_2 and P are secondary masses and periods determined by follow-up observations.

Object	$\log p$	Type	M_1 (M_\odot)	M_2 (M_\odot)	P (d)	References
WD0028–474	< –100	SB2	0.54	≥ 0.46	0.39	SPY: Koester et al. (2009), Napiwotzki et al. (2007). Rebassa-Mansergas et al. (2017)
WD0037–006	< –100	SB2	0.51			
WD0101+048	–17.54	SB1	0.49			
WD0128–387	–0.48	SB2	0.85			
HE0131+0149	–9.47	SB1	0.50			
WD0135–052	< –100	SB2			1.56	Mass could not be derived (see Sect. C); Saffer et al. (1988), Bergeron et al. (1989)
MCT0136–2010	–0.39	SB2	0.86			
HE0205–2945	–4.07	SB2	0.41			
WD0216+143	–6.75	SB1	0.54			
HE0225–1912	–28.02	SB2	0.55	0.23	0.22	SPY: Napiwotzki et al. (2007)
HS0237+1034	0.00	SB2	0.67			
HE0315–0118	< –100	SB2	0.50	0.49	1.91	SPY: Koester et al. (2009); Napiwotzki et al. (2007). Rebassa-Mansergas et al. (2017)
HE0320–1917	–42.87	SB1	0.31	≥ 0.45	0.86	SPY: Nelemans et al. (2005), Koester et al. (2009)
HE0324–1942	–8.18	SB2	0.78			
HE0325–4033	–9.86	SB1	0.49			
WD0326–273	< –100	SB1	0.36	≥ 0.96	1.88	SPY: Nelemans et al. (2005), Koester et al. (2009)
WD0341+021	< –100	SB1	0.38			Probably long period, Maxted et al. (2000a)
WD0344+073	–19.26	SB1	0.39			
HE0410–1137	–40.63	SB2	0.49	0.36	0.51	SPY: Napiwotzki et al. (2007). Rebassa-Mansergas et al. (2017)
WD0453–295	< –100	SB2	0.40	0.44	0.36	SPY: Karl (2004), Napiwotzki et al. (2007)
HE0455–5315	–66.18	SB1	0.47			
WD1013–010	–39.55	SB1	0.32	≥ 0.62	0.44	SPY: Nelemans et al. (2005), Koester et al. (2009)
WD1022+050	< –100	SB1	0.37	>0.28	1.16	Maxted & Marsh (1999), Morales-Rueda et al. (2005), Nelemans et al. (2005)
HS1102+0934	–47.41	SB1	0.38	≥ 0.45	0.55	SPY: Nelemans et al. (2005), Koester et al. (2009). Brown et al. (2013)
WD1115+166	–22.28	SB2	0.69	≥ 0.52	30.1	Maxted et al. (2002)
WD1124–018	< –100	SB1	0.49			
WD1210+140	< –100	SB1	0.33	≥ 0.44	0.64	SPY: Nelemans et al. (2005), Koester et al. (2009)
HS1334+0701	–6.51	SB1	0.35		0.23:	SPY: Karl (2004), period ambiguous
WD1349+144	–53.30	SB2	0.53	0.33	2.21	SPY: Nelemans et al. (2005), Koester et al. (2009)
HE1414–0848	< –100	SB2	0.52	0.74	0.52	SPY: Napiwotzki et al. (2002), Morales-Rueda et al. (2005), Nelemans et al. (2005)
HE1511–0448	–17.85	SB1	0.50	≥ 0.67	3.22	SPY: Nelemans et al. (2005), Koester et al. (2009)
WD1824+040	< –100	SB1	0.40	≥ 0.73	6.27	Saffer et al. (1998), Morales-Rueda et al. (2005), Nelemans et al. (2005)
WD2020–425	< –100	SB2	0.81	0.54	0.30	SPY: Koester et al. (2009); Napiwotzki et al. (2007)
WD2200–136	< –100	SB2	0.46			
HE2209–1444	–38.47	SB2	0.43	0.72	0.28	SPY: Karl et al. (2003), Morales-Rueda et al. (2005), Nelemans et al. (2005)
HS2216+1551	–99.25	SB2	0.64			
WD2330–212	–27.79	SB1	0.45			
WD2336–187	–16.23	SB2	0.36			
HE2345–4810	–15.62	SB1	0.43			

ponent are blueshifted by $60 \dots 70 \text{ km s}^{-1}$ relative to the Balmer lines. The Balmer lines show a weaker blueshifted component, too. This could be explained by gravitational redshift, if the DA were the more massive white dwarf in the system. However, according to the model atmosphere analysis of Wesemael et al. (1994) the DB has higher gravity ($\log g = 9.0$) than the DA

($\log g = 8.5$) thus ruling out gravitational redshift as explanation. We conclude that, although the evidence is somewhat circumstantial, WD 0128–387 is a close DD system consisting of a DA and a DBA. No significant RV variations were detected for the two DAOs HE 1106–0942 and WD 1305–017 included in the SPY sample.

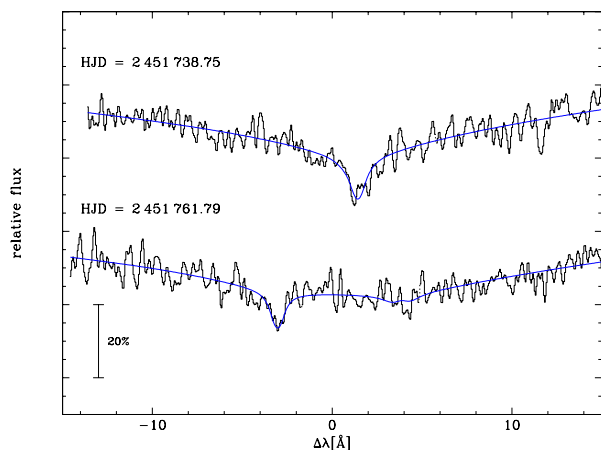


Fig. 10: $H\alpha$ region of the two spectra of WD 2020–425 taken at different epochs.

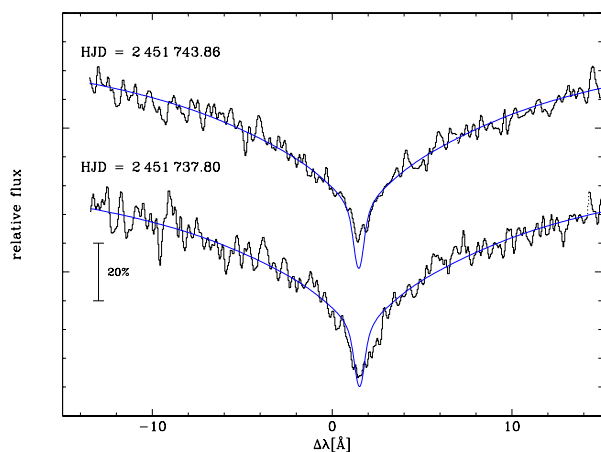


Fig. 11: $H\alpha$ region of the two spectra of MCT 0136–2010 taken at different epochs fitted assuming a single-lined spectrum.

4.5. Notes on individual objects

WD 1845+019: This object is listed as a white dwarf with a cool companion candidate in Hoard et al. (2007). The authors find this white dwarf has a near-IR excess in Two Micron All Sky Survey (2MASS, Skrutskie et al. 2006). Maxted & Marsh (1999) found spectroscopic evidence for a long-period, red companion inferred from the presence of narrow, stationary emission near the core of $H\alpha$. The SPY spectra show similar emission at $H\alpha$, whereas Schmidt & Smith (1995) did not report any sign of such emission from spectra which also covered $H\alpha$. It is not known whether the close neighbour star described by Debes et al. (2005) is gravitationally bound to the white dwarf and whether it is the same as the companion star inferred by Maxted & Marsh (1999). This object was erroneously listed in Koester et al. (2009) as a double degenerate. We measured RVs modelling $H\alpha$ as a composite of a DA spectrum and a Gaussian emission. Our measurements have small error bars and are consistent with constant velocities.

WD 2359–434: The line cores of this white dwarf have a strange flat profile with a weak narrow component already re-

ported in Koester et al. (1998). Koester et al. (1998) speculated that WD 2359–434 is magnetic and that what they see is only the unshifted component of the Zeeman triplet, with the other components shifted outside their observed spectral range or smeared out due to the inhomogeneity of the field. Aznar Cuadrado et al. (2004) included this object in their spectropolarimetric observations and discovered a weak magnetic field of 3 kG. However, our spectra do not show any shifted Zeeman components. A complicated field structure could smear out the shifted components, but a 3 kG field would be too weak to produce smearing over the necessary wavelength range.

Landstreet et al. (2012) reanalysed UVES and FORS data of this object and detected a non-uniform magnetic field in the range 3.1–4.1 kG. On the other hand, Kawka & Vennes (2012) obtained a magnetic field of 9.8 kG from spectropolarimetric observations.

Infrared spectroscopy puts very tight constraints on any cool main sequence or substellar companion (Dobbie et al. 2005). Even brown dwarfs with a spectral type earlier than T8 (corresponding to a mass of $0.05 M_{\odot}$ for an age of 10 Gyr) can be ruled out. No sign of an infrared excess produced by warm circumstellar dust can be seen in the J, H and K bands.

For our RV measurements we modelled the flat bottom line profiles assuming fast rotation and broad Lorentzians, i.e. the narrow component was ignored. Our assumption of fast rotation is only an attempt to model the profile and does not imply that WD 2359–434 is really a fast rotator. Our spectra, taken four days apart, do not show a significant RV shift.

4.5.1. Magnetic white dwarfs

Ten magnetic white dwarfs have been identified in the SPY survey by Zeeman splitting. WD 0058–044 and WD 0239+109 were already published by Koester et al. (2001). HS 0051+1145, HE 1233–0519 and WD 2051–208 were first identified in SPY and details can be found in Koester et al. (2009). Three other magnetic white dwarfs (WD 0257+080, WD 1953–011 and WD 2105–820) were studied by SPY, confirming their magnetic nature, but were already published in previous works. More information on these objects can be found in Koester et al. (2009). Further to these objects in this work we have also identified two other magnetic white dwarfs that were already published (WD 1300–098 and WD 1350–090). More details on these two objects are given below.

WD 1300–098: The SPY spectra of this object showed Zeeman splitting in the Balmer lines (Koester et al. 2009). This was later confirmed in Gianninas et al. (2011).

WD 1350–090: This is a well known magnetic white dwarf which was found through spectropolarimetry to have a weak magnetic field of 85 kG (Schmidt & Smith 1994). Wellhouse et al. (2005) studied the NIR values of this object looking for companions, but did not find one. The Zeeman splitting in the Balmer lines of the SPY spectrum of this white dwarf was first reported in Koester et al. (2001).

4.6. Comparison with Maoz & Hallakoun (2017)

Maoz & Hallakoun (2017) presented a similar analysis of a subsample of 439 DAs out of the 615 SPY DAs analysed by Koester et al. (2009). We start from 643 stars of which 18 have

one spectrum only, leaving us with 625 stars. Hence, the sample of Maoz & Hallakoun (2017) is a subset of ours.

The criteria employed to identify radial velocity variables differ significantly between our two studies. While we use the $\log p < -4$ detection threshold (see Sect. 4), Maoz & Hallakoun (2017) prefer $\Delta RV_{\max} > 15 \text{ km s}^{-1}$ to identify a radial velocity variable star and $10 < \Delta RV_{\max} < 15 \text{ km s}^{-1}$ for candidates. We confirm all of the Maoz & Hallakoun (2017)’s detections except for HE0516–1804 ($\log p = -0.72$), HS2046+0044 ($\log p = -2.54$), and WD0032–317, although as discussed earlier, this latter object could well prove to be a DD given its false alarm probability of $\log p = -3.74$.

We find ten stars to be radial velocity variable which are not listed in Maoz & Hallakoun (2017): the known SB2 systems HE0315–0118, WD0453-295 and WD1115+0934, the known SB1 systems WD0216+143, WD0101+048, WD1022+050, and HE1511-0448 as well as the SB1s HE0455-5315, HS1334+0701, and HE2345-4810. These objects are probably among their rejects. In addition, visual inspection of the UVES spectra allowed us to identify MCT0136-2010 and HS0237+1034 as SB2 systems (see Fig. 9).

Amongst Maoz & Hallakoun (2017)’s candidate RV variable objects ($10 < \Delta RV_{\max} < 15 \text{ km s}^{-1}$), we confirm that HS2216+1551 is a radial velocity variable SB2 system, however, all 15 remaining candidates listed in their Table 1 are rejected using our criterion.

In summary, we reject 17 out of the 43 DDs of Maoz & Hallakoun (2017), confirming only 25 of them. Of these, 7 have system parameters published by the SPY consortium before, and 3 from other sources. From our full sample we identified 39 DDs including 20 SB2 systems. We identify 12 SB1 and 13 SB2 systems in the Maoz & Hallakoun (2017) subsample. However, the overall DD fraction in both samples is the same at 6%, if the same variability test is applied.

The ΔRV_{\max} statistic employed by Maoz & Hallakoun (2017) has two intrinsic weaknesses which could perhaps have contributed to the differences between our studies. First it takes no account of the number of spectra – the expected distribution of ΔRV_{\max} from purely statistical fluctuations always shifts towards larger values as the number of spectra considered increases. For instance, we find that a threshold that is only exceeded by chance 1% of the time with two spectra, is breached almost three times as often with three spectra, a purely statistical and spurious effect. There are perhaps indications in Maoz & Hallakoun (2017)’s results of the influence this effect: three of their 16 candidates have three or more spectra in SPY, whereas only one such case would have been expected by random chance. The second problem with ΔRV_{\max} is that it takes no account of varying statistical uncertainties between spectra. These issues are why we employed Maxted et al. (2000a)’s χ^2 -based criterion.

5. Discussion

We have presented RV measurements of a set of 643 DA white dwarfs observed for the SPY programme and remaining after 46 binaries with cool companions were removed from the original sample of 689. We obtained two or more spectra for 625 of these targets, 632 including targets covered by Maxted et al. (2000a). This sample contains 39 DDs (20 of the SB2 type, 19 of the SB1 type), 35 of them new discoveries. The directly detected rate of DDs in SPY is thus $6.2 \pm 1.0\%$ (uncertainty is 1σ from the binomial distribution). There are likely to be an additional 5 or 6 DDs in our sample that we did not detect, given typical

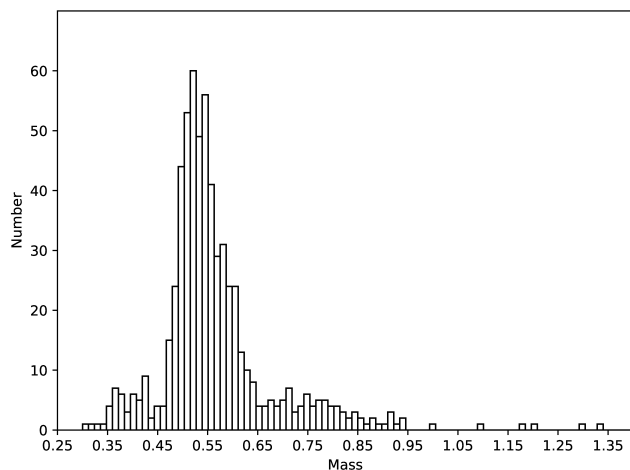


Fig. 12: Mass distribution of the SPY sample.

periods of a day and our mean detection probability (Fig. 6), but a deduction of the space density of DDs requires accounting for much more than just period selection, as we discuss below in section 5.2, so we prefer for simplicity to quote just the numbers as observed.

5.1. Dependence of DD numbers on mass

The SPY sample is large enough to see some significant variations with mass. The limiting mass for a He white dwarf is set by the minimum mass for a helium core flash which increases from 0.43 to 0.49 M_{\odot} (Dorman et al. 1993; Sweigart 1994) with decreasing metallicity, although it is common to adopt a value of 0.45 M_{\odot} . White dwarfs with higher masses usually have cores composed of carbon and oxygen. There are scenarios that lead to the formation of low-mass “hybrid” white dwarfs with C/O cores and thick helium mantles ($\sim 0.1 M_{\odot}$ Iben & Tutukov 1985). Some white dwarfs with masses around 0.45 M_{\odot} may also have evolved via the extreme horizontal branch (EHB), but these objects are also considered to be the product of close binary evolution (e.g. Heber 2009; Kupfer et al. 2015; Heber 2016). So low-mass white dwarfs may not always be helium core white dwarfs, although in all cases evolution within a binary is needed to model the early mass loss that prevents evolution towards a normal C/O WD.

Fig. 12 displays the mass distribution of 615 DA white dwarfs of the SPY sample for which we could derive masses. The distribution may be four populations as suggested by Kepler et al. (2007, cf. their Fig. 8). To examine how DD numbers vary with mass, we consider those targets that (a) have masses in Table C.2 and (b) have two or more spectra and are thus sensitive to DDs. We arrive at the numbers listed in Table 3. All the DDs bar WD0135-052, for which we could not determine a mass from SPY data, contribute to this table, i.e. 38 of the 39 DDs in SPY. We identify the 44 targets with primary masses $M_1 \leq 0.45 M_{\odot}$ (category I) as He white dwarfs. The dominant population II ($0.45 < M_1 \leq 0.65 M_{\odot}$) is identified with C/O-core white dwarfs. A third population of higher masses ($0.65 < M_1 \leq 1.0 M_{\odot}$) should also consist of C/O-core white dwarfs. A few white dwarfs have masses in excess of 1.0 M_{\odot} (population IV) and could include O/Ne-core white dwarfs and mergers in addition to C/O-core stars.

Table 3: Breakdown of targets with two or more spectra into four mutually exclusive sets defined by mass. (Exception: HS0237+1034 has only one spectrum, but is double-lined.) Notation: "[" or "]" – interval includes the limiting value; "(" or ")" – interval excludes the limiting value.

Type	I [0, 0.45]	II (0.45, 0.65]	III (0.65, 1.00]	IV (1.00, 1.40]
all	44	478	83	6
SB1	12	7	0	0
SB2	4	9	6	0

Of the 44 white dwarfs that have a mass below $0.45 M_{\odot}$, 16 show radial velocity variations indicating that they are double degenerates. In terms of detection probability, a set of $0.4+0.4 M_{\odot}$ DDs is comparable to (albeit a little below) the line corresponding to a companion mass of $0.55 M_{\odot}$ in Fig. 6. Thus, assuming periods of order a day, if all 44 were DDs, we would have expected to detect ~ 37 of them as such, ~ 33 if all companions were ELMs or low-mass main-sequence stars, and still ~ 20 to 26 for $0.05 M_{\odot}$ brown-dwarf companions with periods comparable to those discovered to date (Parsons et al. 2017). The observed number of 16 suggests that some of remaining 28 non-detections could be single, or be harbouring very low mass companions. It has been suggested that single low mass white dwarfs result from envelope loss induced by capture and spiral-in of planetary companions (Nelemans & Tauris 1998), or are the cores of red giants stripped by explosions of their companions as supernovae (Justham et al. 2009), or are the products of mergers of components of cataclysmic binaries induced by frictional angular momentum loss following nova eruptions (Zorotovic & Schreiber 2017). All possibilities are interesting and these systems are worth further investigation.

The detection of 16 DDs amongst the 44 He white dwarf primaries is a fraction of $36.4 \pm 7.3\%$. By comparison, the 22 DDs in the remaining 567 systems with $M_1 > 0.45 M_{\odot}$, a fraction of just $3.9 \pm 0.8\%$, is a steep drop. For the dominant population of C/O white dwarfs (set II) the binary fraction is even lower (3.3%), while among the C/O white dwarfs of set III 7.2% are binaries. No binary was found among the white dwarfs with masses exceeding $1 M_{\odot}$ (set 4). The He white dwarf DDs of set I divide 12:4 in favour of single-lined systems, while those of higher mass are skewed 7:15 towards double-lined systems (sets II-IV), in particular for set III, in which all six binary systems are double-lined. The dominant population of C/O white dwarfs (set II) divide almost equally. This is perhaps because low mass white dwarfs are large and will tend to dominate over their companions, but it could also be a consequence of the formation paths that result in these systems. There is useful potential here to constrain evolutionary models.

5.2. Selection effects in the SPY sample.

The current sample of DDs has emerged from searches that often started with mass-dependent selection, following successful searches of the 1990s which concentrated upon low mass white dwarfs (e.g. Marsh et al. 1995). The most extreme example of this strategy is the ELM survey (Brown et al. 2016a) which uncovered targets so low in mass that they were not even recognised as white dwarfs when the SPY survey was undertaken. Such surveys are biased precisely against the high mass systems of most interest as Type Ia progenitors, except to the extent that some may harbour high mass white dwarfs hidden in the

glare of dominant low mass primary stars. They also focus on the extreme low mass wing of the white dwarf mass distribution, which is untypical of most systems. SPY is by far the most sensitive survey without mass selection built in from the start. Precursors to SPY were Bragaglia et al. (1990) and Maxted et al. (2000a) who surveyed 54 and 71 white dwarfs on 2–4 m-class telescopes, uncovering a handful of candidates, although the second of these studies emerged from searches that concentrated in the main upon low mass targets. The Sloan Digital Sky Survey (SDSS), although not designed for radial velocity work, serendipitously provides a very different type of constraint, providing a much larger sample, but also much looser radial velocity constraints. The SDSS is perhaps somewhat superior to SPY for finding massive, short-period Type Ia progenitors (Breedt et al. 2017), but SPY is far more sensitive to the bulk population of longer period and lower mass DDs. Moreover, SPY is particularly efficient in finding double-lined systems because of its high spectral resolution. At lower resolution such as the SDSS spectra, it is far more difficult because the components' line profiles are not resolved and the orbital motion will broaden the combined line profile rather than shifting the unresolved line centre. This is probably why double-lined DDs have not been found directly by the SDSS project. In addition visual inspection of SPY spectra allowed SB2 systems to be discovered that were considered RV non-variable by the detection criterion and, therefore, probably have long orbital periods. Hence, SPY will enable a more complete and reliable calibration of theoretical models. The two surveys are in many ways complementary to each other (Maoz et al. 2018), as can be judged from the detection probability plot for SDSS (Fig. 4; Breedt et al. 2017), comparable to Fig. 6 in this paper. The SDSS detection rate falls below 50% for $P > 0.2$ days, whereas SPY extends over 100 times longer, only dropping below 50% for $P > 30$ days. The numbers of DD detections in each survey corroborate this: the 6396 SDSS targets studied by Breedt et al. (2017) yielded 15 DDs, while we have found 39 DDs in 625 SPY targets. One can deduce ~ 400 other DDs in the SDSS sample that have yet to be detected as such.

The SPY sample was selected without regard to mass, but it inherits the selection effects of the input catalogues it was derived from, and accounting for these will be crucial when making comparisons to theoretical population models. A non-exhaustive list of such effects is: (a) period-dependent selection (Fig. 6), (b) selection by galactic location (Fig. 1), (c) colour selection, (d) selection by kinematics via proper motion surveys, and (e) selection by magnitude limits. All of these can be translated to a greater or lesser extent into mass-dependent selection functions. For instance, selection by temperature favours high mass targets since it takes longer for high mass white dwarfs to cool to 10 000 K than it does low mass white dwarfs, owing to a combination of available thermal energy and surface area. On the contrary, magnitude-limited surveys strongly favour low mass white dwarfs because of their greater size. There are also subtler effects such as mass-dependent kinematics (Wegg & Phinney 2012) which can lead to both proper motions and scale-heights varying with white dwarf mass. The correct way to allow for these effects is to impose them as closely as possible upon theoretically-derived samples rather than attempt to remove them from the observations. To this end we include a compilation of temperatures and gravities of the SPY sample along with Gaia IDs in Appendix C to facilitate future calculations. SPY-like samples can be generated from theoretical populations by selecting targets of similar colours and magnitudes and imposing in addition a similar selection by Galactic latitude. A full calculation would also simulate the detection of DDs

along the lines of Rebassa-Mansergas et al. (2019). Such model-dependent calculations are far beyond our scope here where we aim instead to try to convey a feel for the level of the selection effects affecting the SPY sample, beyond the obvious ones of Galactic latitude and period discussed earlier.

Given the heterogeneous origins of the SPY input catalogue from a multitude of proper-motion, colour and objective prism surveys as well as serendipitous discoveries, it is close to impossible to unravel the selection effects of the original survey papers. Instead, we take advantage of the Gaia DR2 survey (Gaia Collaboration et al. 2018) to quantify the extent of mass-dependent bias within the SPY sample selection as shown in Fig. 13. We do so by choosing an approximately volume-limited sub-sample from Gaia as an approximation of what is naturally produced by population synthesis calculations. Unsurprisingly, the SPY sample⁴ is very differently distributed to the Gaia sample as shown in the Hertzsprung-Russell diagram on the left of Fig. 13. Above all, it is strongly skewed towards blue colours and high temperatures, reflecting the origins of the sample. The temperature selection automatically implies mass-dependent selection because of differential white dwarf cooling rates, as discussed above.

To judge the significance of additional mass-dependent selection biases, particularly that associated with the magnitude-limited input catalogues, we next look at the distribution of magnitudes *across* the main white dwarf cooling track, restricting ourselves to Gaia colours $G_{BP} - G_{RP} < 0$ to avoid a region of bifurcation in the Gaia H-R diagram believed to be associated with helium-dominated atmospheres (Gentile Fusillo et al. 2019). (The differential effect of atmospheric composition in this region can be seen directly in Fig. 13 where our hydrogen-dominated DA sample clusters mainly along the upper of the two branches once $G_{BP} - G_{RP} > 0$.) The restriction in colour builds differential cooling mass-selection into the Gaia-selected reference sample too, so we are looking here for additional effects such as kinematic and magnitude bias. The key result is in the right-hand panel of Fig. 13 which shows that over-luminous targets ($\Delta M_G < -0.5$) are over-represented in SPY compared to a near-volume-limited Gaia sample, whereas faint systems ($\Delta M_G > +1$) are under-represented. This is as one would expect of a magnitude-limited sample, but the bias is slight compared to samples chosen for low mass, which are equivalent to applying the restriction $\Delta M_G < -0.5$ from the start. Translating Fig. 13 into a mass-bias is complex, since, while we can assume that $\Delta M_G > 0$ targets are more massive than average, double-lined systems with equal contributions from both components get a -0.75 magnitude boost, and could be reasonably massive but still end with $\Delta M_G < 0$. Such calculations are beyond our scope here as they would need to be made separately for any model population. The key point perhaps is that although the biases in the SPY sample are small compared to others in the literature, they are still significant and must be accounted for in any calculation of intrinsic DD fractions and merger rates.

Twenty of the 39 binaries found in SPY are double-lined, an astonishingly large fraction. As remarked above, double-lined systems are potentially up to 0.75 magnitudes brighter than single white dwarfs of the same mass, boosting the chance that they are included in a magnitude-limited sample. Since the SPY sample was compiled from a number of catalogues and surveys with

different faint limits, the survey does not have a well defined cut-off magnitude, however we can estimate the significance of the effect from the systems in hand. Figure 14 shows the probability of a white dwarf to be included in SPY. It was derived by comparing the brightness distribution of observed white dwarfs with a population produced using the model described in Napiwotzki (2009). Numbers of observed white dwarfs found in each bin are compared to the model predictions. Only relative probabilities are important. The probability is modeled with a simple linear function and assumed to be one for white dwarfs brighter than 13.55. The fitted probability p is

$$p = \begin{cases} 1.00 & V \leq 13.55 \\ 5.27 - 0.3154V & 13.55 \leq V \leq 16.55 \\ 0.00 & V > 16.55 \end{cases} \quad (1)$$

Fundamental parameters were determined by fitting the spectra with model spectra representing the two components (see appendix C for details). We then calculated the contribution of the secondary star to the combined brightness and from that the brightness of the primary star alone. The probabilities of the system and the primary star alone were calculated using Eq. (1) and used to estimate the probability of the primary alone making it into the SPY sample. Example, if the probabilities are 60% and 30%, respectively, we count the system as 0.5. It turned out that 12.5 of the 20 double-lined binaries (63%) would have appeared in the survey. The total number of detected binaries would have dropped from 39 to 31.5 (81%).

5.3. Implications for SN Ia progenitor scenarios.

Since the initiation of the SPY project, ideas about possible progenitors of SNe Ia have evolved considerably. In particular, the extensive work in following up SNe Ia has revealed a richer diversity than was previously imagined (Taubenberger 2017). The most profound change perhaps has been a move away from the Chandrasekhar mass model, as there now seems to be good evidence for sub-Chandrasekhar ejecta masses in observed SNe Ia (e.g., Scalzo et al. 2014).

We note that among the objects already discovered by SPY there are two systems – WD2020–425 ($M=(0.81+0.54)M_{\odot}$, $P=0.3$ day) and HE2209–1444 ($M=(0.72+0.43)M_{\odot}$, $P=0.28$ day), which may well qualify as candidates for sub-Chandrasekhar SN Ias progenitors. Moreover, the SPY project is not completed, as yet. Out of 39 DDs identified in the survey, only 19 have measured M_2 or lower limits thereof from radial velocity curves. There are 10 SB2 DD still needing follow-up observations by UVES (see Tab. 2). The most interesting SB2 system to follow up is HE0324–1942, because its primary mass ($\approx 0.8 M_{\odot}$) is as high as that of WD2020–425.

The expectation of finding a super-Chandrasekhar pre-SN Ia white dwarf pair in the sample of about 1000 objects brighter than $V \approx 16^m.5$ was based on a count of the number of model systems satisfying the criteria $M_{tot} > M_{Ch}$ and $t_{merger} < t_{Hubble}$, while any selection effects were ignored. However, a numerical experiment modelling observations of a similar sample of white dwarfs by an instrument like VLT/UVES in which the effects of observational selection (orbital inclination, observational strategy, observing conditions, etc.) were taken into account (Rebassa-Mansergas et al. 2019), has shown that finding such a pair of white dwarfs may require a much larger sample of objects – they estimate a factor of ten. Given that the sample size of 643 presented in the paper does not match even the original aim of around 1000 targets (owing in the main to subdwarfs

⁴ Apart from the following seven SPY targets that have either no parallax or no colour in Gaia: PG0922+162A, PG0922+162B, WD1015+076, HE1117–0222, WD1121+216, WD1147+255 and WD1214+032

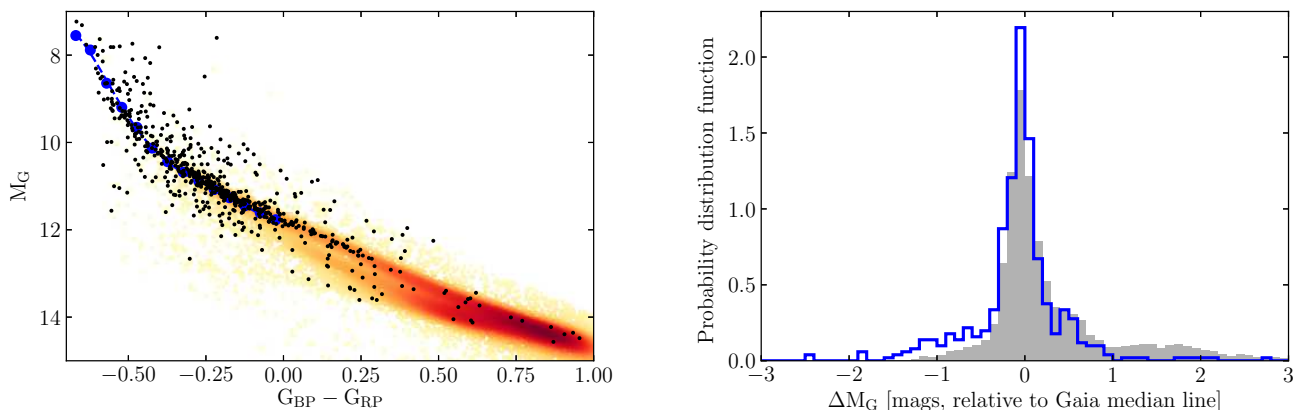


Fig. 13: *Left*: The SPY sample (black dots) plotted in a Hertzsprung-Russell diagram (Gaia absolute magnitude versus Gaia colour) on top of a background of 11 561 white dwarf candidates selected from the Gaia-derived sample of Gentile Fusillo et al. (2019) and colour-coded by plot density. The parallax π and parallax error σ_π were restricted by $\pi > 10$ mas and $\pi > 5\sigma_\pi$ to give a near volume-limited sample to $d = 100$ pc, although there is still incompleteness in the lower part of the plot since $M_G > 14$ at 100 pc corresponds to $G > 19$. The large blue dots on the left mark the main cooling track of the Gaia white dwarfs, avoiding the bifurcation that sets in at $G_{BP} - G_{RP} > 0$. The dashed line represents a polynomial fitted to these that was then subtracted from the Gaia and SPY targets to derive differential absolute magnitude histograms. *Right*: Histograms of the differential magnitudes for Gaia (solid grey) and SPY (outline blue). The SPY sample has relatively more intrinsically bright objects than the Gaia sample, and thus fewer massive white dwarfs.

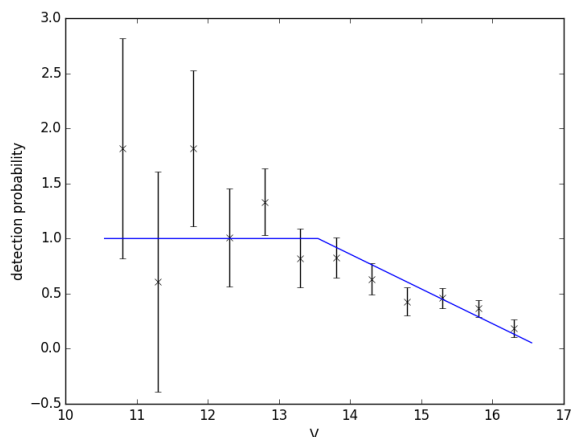


Fig. 14: Relative probability of a white dwarf being included in SPY as a function of brightness. Error bars are derived from the Poisson distribution.

(Lisker et al. 2005; Stroerer et al. 2007) which are hard to distinguish from white dwarfs from colours alone, and not to mind the $\sim 20\%$ detection efficiency loss), the SPY sample may well not deliver a super-Chandrasekhar, short period DD, but with the switch of emphasis towards sub-Chandrasekhar mergers, it nonetheless retains its significance, and is the only large survey sensitive to masses and periods typical of the bulk of the DD population.

The discovery of the DDs presented here is only a first step; the next is the determination of their orbital periods, which has been accomplished already in some cases, and should be a priority in future work on this sample. Once this is accomplished, we should be in a position to be able to compare the properties of DDs in samples generated through binary population synthesis to an observed sample of relatively weak mass bias, and hence

be able to judge on the SNe Ia rate that the Galactic population of DDs can plausibly sustain.

6. Summary

In this paper we have presented the methods and results of radial velocity measurements of 643 DA white dwarfs observed with UVES and the VLT as part of the SPY survey. We find 39 double degenerates in this sample, including 20 double-lined systems which show spectral components from both white dwarfs. One of the double-lined systems (WD 2020–425) is a candidate SN Ia progenitor with a total mass close to the Chandrasekhar limit, but the uncertainties of the mass for this binary are too large to be certain of this at present. The absolute radial velocities we presented will allow for future searches for long-period binarity, while the sample of DDs is well-suited for tests of binary population models.

The overall DD fraction in the SPY sample is 6%. We compared our results to the results of Maoz & Hallakoun (2017), who studied a subsample of the SPY data set and derived a DD fraction of $10\% \pm 2\%$ (1σ , random) $+2\%$ (systematic). We showed that their detection criterion for radial velocity variability is overly optimistic. Applying our detection criterion, we showed that 17 of their candidate DDs are unlikely to be RV variable, reducing their SPY subsample to 25 DDs. Accordingly, the DD fraction in the Maoz & Hallakoun (2017) subsample is in fact 6%, consistent as it should be with our result for the full SPY sample.

Our detected DD fraction among C/O white dwarfs is $3.9 \pm 0.8\%$, below the 10% fraction previously found, perhaps reflecting the prominence of low mass He white dwarfs in literature studies. The detected DD fraction amongst He white dwarfs in SPY is much higher at $36.4 \pm 7.3\%$, although it seems unlikely that all He white dwarfs are binary. We estimated that the number of binaries needs to be corrected by a factor of 0.8 to account for the increased probability of double-lined systems to be included in SPY, but there is a similar factor in reverse because

our detection efficiency is 80 to 90% for typical DD periods, and a full comparison with theoretical models needs to take multiple selection effects into account, despite their being weaker in SPY than in any comparable survey. We provide the data needed to accomplish such a task.

Acknowledgements. We express our gratitude to the ESO staff, for providing invaluable help and conducting the service observations and pipeline reductions, which have made this work possible. TRM and SC were supported under grants from the UK's Science and Technology Facilities Council (STFC), ST/L00073 and ST/P000495/1. LRY is partially supported by Presidium of the Russian Academy of Sciences program P-28 and RFBR grant 19-02-00790. Work on the SPY project in Bamberg is supported by the DFG (grants Na365/2-1, Na365/2-2, HE1356/40-3 and HE1356/40-4). We thank Markus Dimpel for obtaining the Gaia IDs.

References

- Althaus, L. G., García-Berro, E., Isern, J., & Córscico, A. H. 2005, *A&A*, 441, 689
- Andrews, D. W. K. & Buchinsky, M. 2000, *Econometrica*, 68, 23
- Aznar Cuadrado, R., Jordan, S., Napiwotzki, R., et al. 2004, *A&A*, 423, 1081
- Benvenuto, O. G. & Althaus, L. G. 1999, *MNRAS*, 303, 30
- Benz, W., Cameron, A. G. W., Press, W. H., & Bowers, R. L. 1990, *ApJ*, 348, 647
- Bergeron, P. & Liebert, J. 2002, *ApJ*, 566, 1091
- Bergeron, P., Wesemael, F., Liebert, J., & Fontaine, G. 1989, *ApJ*, 345, L91
- Bours, M. C. P., Toonen, S., & Nelemans, G. 2013, *A&A*, 552, A24
- Bragaglia, A., Greggio, L., Renzini, A., & D'Odorico, S. 1990, *ApJ*, 365, L13
- Branch, D. & Wheeler, J. C. 2017, *Supernova Explosions* (Springer-Verlag)
- Breedt, E., Steeghs, D., Marsh, T. R., et al. 2017, *MNRAS*, 468, 2910
- Brown, W. R., Gianninas, A., Kilic, M., Kenyon, S. J., & Allende Prieto, C. 2016a, *ApJ*, 818, 155
- Brown, W. R., Kilic, M., Allende Prieto, C., Gianninas, A., & Kenyon, S. J. 2013, *ApJ*, 769, 66
- Brown, W. R., Kilic, M., Allende Prieto, C., & Kenyon, S. J. 2010, *ApJ*, 723, 1072
- Brown, W. R., Kilic, M., Allende Prieto, C., & Kenyon, S. J. 2012, *ApJ*, 744, 142
- Brown, W. R., Kilic, M., Kenyon, S. J., & Gianninas, A. 2016b, *ApJ*, 824, 46
- Christlieb, N., Wisotzki, L., Reimers, D., et al. 2001, *A&A*, 366, 898
- Dan, M., Rosswog, S., & Brüggen, M. 2009, *Journal of Physics Conference Series*, 172, 012034
- Dan, M., Rosswog, S., Brüggen, M., & Podsiadlowski, P. 2014, *MNRAS*, 438, 14
- Debes, J. H., Sigurdsson, S., & Woodgate, B. E. 2005, *AJ*, 130, 1221
- Dekker, H., D'Odorico, S., Kaufer, A., Delabre, B., & Kotzłowski, H. 2000, in *Society of Photo-Optical Instrumentation Engineers (SPIE) Conference Series*, Vol. 4008, *Optical and IR Telescope Instrumentation and Detectors*, ed. M. Iye & A. F. Moorwood, 534–545
- Dobbie, P. D., Burleigh, M. R., Levan, A. J., et al. 2005, *MNRAS*, 357, 1049
- Dorman, B., Rood, R. T., & O'Connell, R. W. 1993, *ApJ*, 419, 596
- D'Souza, M., Motl, P., Tohline, J., & J. F. 2006, *ApJ*, 643, 381
- Faulkner, J., Flannery, B. P., & Warner, B. 1972, *ApJ*, 175, L79
- Finley, D. S. & Koester, D. 1997, *ApJ*, 489, L79
- Foss, D., Wade, R. A., & Green, R. F. 1991, *ApJ*, 374, 281
- Freudling, W., Romaniello, M., Bramich, D. M., et al. 2013, *A&A*, 559, A96
- Gaia Collaboration, Brown, A. G. A., Vallenari, A., et al. 2018, *A&A*, 616, A1
- Gentile Fusillo, N. P., Tremblay, P.-E., Gänsicke, B. T., et al. 2019, *MNRAS*, 482, 4570
- Giammichele, N., Bergeron, P., & Dufour, P. 2012, *ApJS*, 199, 29
- Gianninas, A., Bergeron, P., & Ruiz, M. T. 2011, *ApJ*, 743, 138
- Giclas, H. L., Burnham, Jr., R., & Thomas, N. G. 1978, *Lowell Observatory Bulletin*, 8, 89
- Giclas, H. L., Burnham, Jr., R., & Thomas, N. G. 1980, *Lowell Observatory Bulletin*, 8, 157
- Grabowski, B., Halenka, J., & Madej, J. 1987, *ApJ*, 313, 750
- Green, R. F., Schmidt, M., & Liebert, J. 1986, *ApJS*, 61, 305
- Greenstein, J. L. & Peterson, D. M. 1973, *A&A*, 25, 29
- Griffin, R. 1973, *MNRAS*, 162, 243
- Guerrero, J., García-Berro, E., & Isern, J. 2004, *A&A*, 413, 257
- Hagen, H.-J., Groote, D., Engels, D., & Reimers, D. 1995, *A&AS*, 111, 195
- Halenka, J., Olchawa, W., Madej, J., & Grabowski, B. 2015, *ApJ*, 808, 131
- Hamada, T. & Salpeter, E. E. 1961, *ApJ*, 134, 683
- Heber, U. 2009, *ARA&A*, 47, 211
- Heber, U. 2016, *PASP*, 128, 082001
- Heber, U., Napiwotzki, R., Lemke, M., & Edelmann, H. 1997a, *A&A*, 324, L53
- Heber, U., Napiwotzki, R., & Reid, I. N. 1997b, *A&A*, 323, 819
- Hillebrandt, W., Kromer, M., Röpke, F. K., & Ruiter, A. J. 2013, *Frontiers of Physics*, 8, 116
- Hoard, D. W., Wachter, S., Sturch, L. K., et al. 2007, *AJ*, 134, 26
- Homeier, D., Koester, D., Hagen, H.-J., et al. 1998, *A&A*, 338, 563
- Hoyle, F. & Fowler, W. A. 1960, *ApJ*, 132, 565
- Iben, I., Tutukov, A. V., & Yungelson, L. R. 1997, *ApJ*, 475, 291
- Iben, Jr., I. & Tutukov, A. V. 1984, *ApJS*, 54, 335
- Iben, Jr., I. & Tutukov, A. V. 1985, *ApJS*, 58, 661
- Jordan, S., Koester, D., Vauclair, G., et al. 1998, *A&A*, 330, 277
- Justham, S., Wolf, C., Podsiadlowski, P., & Han, Z. 2009, *A&A*, 493, 1081
- Karl, C. 2004, PhD thesis, Friedrich-Alexander University Erlangen-Nürnberg
- Karl, C. A., Napiwotzki, R., Nelemans, G., et al. 2003, *A&A*, 410, 663
- Kawka, A. & Vennes, S. 2012, *MNRAS*, 425, 1394
- Kepler, S. O., Kleinman, S. J., Nitta, A., et al. 2007, *MNRAS*, 375, 1315
- Kilic, M., Brown, W. R., Allende Prieto, C., et al. 2012, *ApJ*, 751, 141
- Kilkenny, D., O'Donoghue, D., Koen, C., Stobie, R. S., & Chen, A. 1997, *MNRAS*, 287, 867
- Koester, D., Dreizler, S., Weidemann, V., & Allard, N. F. 1998, *A&A*, 338, 612
- Koester, D. & Herrero, A. 1988, *ApJ*, 332, 910
- Koester, D. & Kompá, E. 2007, *A&A*, 473, 239
- Koester, D., Napiwotzki, R., Christlieb, N., et al. 2001, *A&A*, 378, 556
- Koester, D., Napiwotzki, R., Voss, B., Homeier, D., & Reimers, D. 2005a, *A&A*, 439, 317
- Koester, D., Röllenhagen, K., Napiwotzki, R., et al. 2005b, *A&A*, 432, 1025
- Koester, D., Voss, B., Napiwotzki, R., et al. 2009, *A&A*, 505, 441
- Kulkarni, S. R. & van Kerkwijk, M. H. 2010, *ApJ*, 719, 1123
- Kupfer, T., Geier, S., Heber, U., et al. 2015, *A&A*, 576, A44
- Lamontagne, R., Demers, S., Wesemael, F., Fontaine, G., & Irwin, M. J. 2000, *AJ*, 119, 241
- Landstreet, J. D., Bagnulo, S., Valyavin, G. G., et al. 2012, *A&A*, 545, A30
- Latour, M., Fontaine, G., Green, E. M., & Brassard, P. 2015, *A&A*, 579, A39
- Liebert, J., Bergeron, P., Schmidt, G. D., & Saffer, R. A. 1993, *ApJ*, 418, 426
- Lisker, T., Heber, U., Napiwotzki, R., et al. 2005, *A&A*, 430, 223
- Livio, M. & Mazzali, P. 2018, *Phys. Rep.*, 736, 1
- Livne, E. 1990, *ApJ*, 354, L53
- Livne, E. & Glasner, A. 1991, *ApJ*, 370, 272
- Luyten, W. J. 1979, *LHS catalogue. A catalogue of stars with proper motions exceeding 0"5 annually* (Minneapolis: University of Minnesota, 1979, 2nd ed.)
- Maoz, D. & Hallakoun, N. 2017, *MNRAS*, 467, 1414
- Maoz, D., Hallakoun, N., & Badenes, C. 2018, *MNRAS*, 476, 2584
- Maoz, D., Mannucci, F., & Nelemans, G. 2014, *ARA&A*, 52, 107
- Marsh, T. R. 1995, *MNRAS*, 275, L1
- Marsh, T. R. 2000, *New A Rev.*, 44, 119
- Marsh, T. R., Dhillion, V. S., & Duck, S. R. 1995, *MNRAS*, 275, 828
- Marsh, T. R., Gänsicke, B. T., Steeghs, D., et al. 2011, *ApJ*, 736, 95
- Marsh, T. R., Nelemans, G., & Steeghs, D. 2004, *MNRAS*, 350, 113
- Maxted, P. F. L., Burleigh, M. R., Marsh, T. R., & Bannister, N. P. 2002, *MNRAS*, 334, 833
- Maxted, P. F. L. & Marsh, T. R. 1999, *MNRAS*, 307, 122
- Maxted, P. F. L., Marsh, T. R., & Moran, C. K. J. 2000a, *MNRAS*, 319, 305
- Maxted, P. F. L., Marsh, T. R., Moran, C. K. J., & Han, Z. 2000b, *MNRAS*, 314, 334
- Maxted, P. F. L., Napiwotzki, R., Dobbie, P. D., & Burleigh, M. R. 2006, *Nature*, 442, 543
- McCook, G. P. & Sion, E. M. 1999, *ApJS*, 121, 1
- Mochkovitch, R. & Livio, M. 1990, *A&A*, 236, 378
- Morales-Rueda, L., Marsh, T. R., Maxted, P. F. L., et al. 2005, *MNRAS*, 359, 648
- Moran, C., Marsh, T. R., & Bragaglia, A. 1997, *MNRAS*, 288, 538
- Napiwotzki, R. 1999, *A&A*, 350, 101
- Napiwotzki, R. 2009, in *Journal of Physics Conference Series*, Vol. 172, *Journal of Physics Conference Series*, 012004
- Napiwotzki, R., Christlieb, N., Drechsel, H., et al. 2001a, *Astronomische Nachrichten*, 322, 411
- Napiwotzki, R., Christlieb, N., Drechsel, H., et al. 2003, *The Messenger*, 112, 25
- Napiwotzki, R., Edelmann, H., Heber, U., et al. 2001b, *A&A*, 378, L17
- Napiwotzki, R., Green, P. J., & Saffer, R. A. 1999, *ApJ*, 517, 399
- Napiwotzki, R., Karl, C. A., Nelemans, G., et al. 2005, in *Astronomical Society of the Pacific Conference Series*, Vol. 334, *14th European Workshop on White Dwarfs*, ed. D. Koester & S. Moehler, 375
- Napiwotzki, R., Karl, C. A., Nelemans, G., et al. 2007, in *Astronomical Society of the Pacific Conference Series*, Vol. 372, *15th European Workshop on White Dwarfs*, ed. R. Napiwotzki & M. R. Burleigh, 387
- Napiwotzki, R., Koester, D., Nelemans, G., et al. 2002, *A&A*, 386, 957
- Napiwotzki, R., Yungelson, L., Nelemans, G., et al. 2004, in *Astronomical Society of the Pacific Conference Series*, Vol. 318, *Spectroscopically and Spatially Resolving the Components of the Close Binary Stars*, ed. R. W. Hilditch, H. Hensberge, & K. Pavlovski, 402–410
- Nelemans, G., Napiwotzki, R., Karl, C., et al. 2005, *A&A*, 440, 1087

- Nelemans, G., Portegies Zwart, S. F., Verbunt, F., & Yungelson, L. R. 2001a, A&A, 368, 939
- Nelemans, G. & Tauris, T. M. 1998, A&A, 335, L85
- Nelemans, G., Yungelson, L. R., Portegies Zwart, S. F., & Verbunt, F. 2001b, A&A, 365, 491
- Nomoto, K. & Iben, I. J. 1985, ApJ, 297, 531
- Panei, J. A., Althaus, L. G., Chen, X., & Han, Z. 2007, MNRAS, 382, 779
- Parsons, S. G., Hermes, J. J., Marsh, T. R., et al. 2017, MNRAS, 471, 976
- Pauli, E.-M., Napiwotzki, R., Altmann, M., et al. 2003, A&A, 400, 877
- Pauli, E.-M., Napiwotzki, R., Heber, U., Altmann, M., & Odenkirchen, M. 2006, A&A, 447, 173
- Perlmutter, S., Aldering, G., Goldhaber, G., et al. 1999, ApJ, 517, 565
- Postnov, K. A. & Yungelson, L. R. 2014, Living Reviews in Relativity, 17, 3
- Pounds, K. A., Allan, D. J., Barber, C., et al. 1993, MNRAS, 260, 77
- Press, W. H., Teukolsky, S. A., Vetterling, W. T., & Flannery, B. P. 1992, Numerical recipes in FORTRAN. The art of scientific computing (Cambridge: University Press, 2nd ed.)
- Rebassa-Mansergas, A., Parsons, S. G., García-Berro, E., et al. 2017, MNRAS, 466, 1575
- Rebassa-Mansergas, A., Toonen, S., Korol, V., & Torres, S. 2019, MNRAS, 482, 3656
- Renedo, I., Althaus, L. G., Miller Bertolami, M. M., et al. 2010, ApJ, 717, 183
- Renzini, A. 1999, The Messenger, 96, 13
- Richter, R., Heber, U., & Napiwotzki, R. 2007, in Astronomical Society of the Pacific Conference Series, Vol. 372, 15th European Workshop on White Dwarfs, ed. R. Napiwotzki & M. R. Burleigh, 107
- Riess, A. G., Filippenko, A. V., Challis, P., et al. 1998, AJ, 116, 1009
- Robinson, E. L. & Shafter, A. W. 1987, ApJ, 322, 296
- Röpke, F. K. & Sim, S. A. 2018, Space Sci. Rev., 214, 72
- Ruiz-Lapuente, P. 2014, New A Rev., 62, 15
- Saffer, R. A., Liebert, J., & Olszewski, E. W. 1988, ApJ, 334, 947
- Saffer, R. A., Livio, M., & Yungelson, L. R. 1998, ApJ, 502, 394
- Sato, Y., Nakasato, N., Tanikawa, A., et al. 2016, ApJ, 821, 67
- Scalzo, R., Aldering, G., Antilogus, P., et al. 2014, MNRAS, 440, 1498
- Schatzman, E. 1963, in Star Evolution, ed. L. Gratton, 389
- Schmidt, G. D. & Smith, P. S. 1994, ApJ, 423, L63
- Schmidt, G. D. & Smith, P. S. 1995, ApJ, 448, 305
- Shigeyama, T., Nomoto, K., Yamaoka, H., & Thielemann, F.-K. 1992, ApJ, 386, L13
- Shipman, H. L. & Mehan, R. G. 1976, ApJ, 209, 205
- Sim, S. A., Röpke, F. K., Hillebrandt, W., et al. 2010, ApJ, 714, L52
- Skrutskie, M. F., Cutri, R. M., Stiening, R., et al. 2006, AJ, 131, 1163
- Solheim, J.-E. & Yungelson, L. R. 2005, in Astronomical Society of the Pacific Conference Series, Vol. 334, 14th European Workshop on White Dwarfs, ed. D. Koester & S. Moehler, 387
- Stroerer, A., Heber, U., Lisker, T., et al. 2007, A&A, 462, 269
- Sweigart, A. V. 1994, ApJ, 426, 612
- Taubenberger, S. 2017, The Extremes of Thermonuclear Supernovae, 317
- Tremblay, P.-E., Ludwig, H.-G., Steffen, M., & Freytag, B. 2013a, A&A, 552, A13
- Tremblay, P.-E., Ludwig, H.-G., Steffen, M., & Freytag, B. 2013b, A&A, 559, A104
- Truran, J. W. & Cameron, A. G. W. 1971, Ap&SS, 14, 179
- Tutukov, A. V. & Yungelson, L. R. 1976, Astrophysics, 12, 342
- Tutukov, A. V. & Yungelson, L. R. 1979, Acta Astron., 29, 665
- Tutukov, A. V. & Yungelson, L. R. 1981, Nauchnye Informatsii, 49, 3
- Webbink, R. F. 1979, in IAU Colloq. 53: White Dwarfs and Variable Degenerate Stars, ed. H. M. van Horn & V. Weidemann, 426–447
- Webbink, R. F. 1984, ApJ, 277, 355
- Wegg, C. & Phinney, E. S. 2012, MNRAS, 426, 427
- Wellhouse, J. W., Hoard, D. W., Howell, S. B., Wachter, S., & Esin, A. A. 2005, PASP, 117, 1378
- Werner, K. 1996, ApJ, 457, L39
- Wesemael, F., Bergeron, P., Lamontagne, R. L., et al. 1994, ApJ, 429, 369
- Wheeler, J. C. & Hansen, C. J. 1971, Ap&SS, 11, 373
- Whelan, J. & Iben, Jr., I. 1973, ApJ, 186, 1007
- Wiese, W. L. & Kelleher, D. E. 1971, ApJ, 166, L59
- Wiese, W. L., Kelleher, D. E., & Paquette, V. 1972, Phys. Rev. A, 71, 1132
- Wisotzki, L., Christlieb, N., Bade, N., et al. 2000, A&A, 358, 77
- Yungelson, L. R. 2010, Astronomy Letters, 36, 780
- Yungelson, L. R. & Kuranov, A. G. 2017, MNRAS, 464, 1607
- Zorotovic, M. & Schreiber, M. R. 2017, MNRAS, 466, L63

Table A.1: Systematic shifts measured for the H100 sample

measurement	interval Å	remark	RV shift km s ⁻¹
RV(H β)–RV(H α)	± 15 Å		-0.8 ± 0.4
RV(H β)–RV(H α)	± 30 Å		-2.5 ± 0.4
RV(H β)–RV(H α)	± 30 Å	core smoothed	-8.7 ± 0.6
RV(H α + H β)–RV _{best}	± 30 Å	core smoothed	-3.7 ± 0.3

Notes. The 1σ uncertainty of the average is given, calculated using bootstrapping.

Appendix A: A test of the possible impact of pressure broadening on Balmer lines

The densities in atmospheres of white dwarfs are sufficiently high that pressure shifts of line profiles are a concern. If present, these effects mimic an RV shift. Laboratory experiments by Wiese & Kelleher (1971) and Wiese et al. (1972) measured substantial pressure redshifts for H β , H γ , H δ and to a lesser extent for H α . Shipman & Mehan (1976) included the shifts determined in these experiments and solved the radiation transfer for white dwarf atmospheres. The resulting line profiles were analysed following the procedure applied to observed spectra at that time to determine the line centre. This investigation found that effects for H α and H β were below the 1 km s^{-1} level. A later analysis by Grabowski et al. (1987) revisited the Wiese et al. (1972) data and carried out a more detailed fit of the measurements with three parameters (plus a correction term). Stellar line profiles were computed using model atmospheres and analysed in a fashion similar to the previous investigation by Shipman & Mehan (1976). The new study by Grabowski et al. (1987) confirmed small pressure shifts for H α exceeding $1\text{--}2 \text{ km s}^{-1}$ only for cool, high gravity ($\log g = 9$) white dwarfs. However, for H β the authors find large shifts often in the range $5\text{--}10 \text{ km s}^{-1}$.

A recent study by Halenka et al. (2015) calculated theoretical line profiles using a so-called modified full computer simulation method. This method treats shifts and asymmetries as corrections depending on the local plasma conditions to a simpler first order description of line profiles. The authors compare the new calculations with laboratory data and find improvements to previous attempts. Atmospheric line profiles of H α and H β were calculated using the new theoretical calculations. The result is even smaller pressure shifts for H α than reported in Grabowski et al. (1987). The effect does not exceed 1 km s^{-1} even when the measurement is carried out 25 \AA from the line centre. Contrary to that the new study finds an effect for H β about twice as large as previously, exceeding 10 km s^{-1} at a distance of 15 \AA . The authors point out that the impact on RV measurements should be very small, if the resolved NLTE core of the lines is measured in high resolution spectra. The Doppler core is formed in low density regions of the atmosphere where the Stark effect is of no importance compared to Doppler broadening.

We carried out an empirical test of the possible impact of H β pressure shifts on our RV measurements. We selected a subset of white dwarfs from Table B.1 with clearly visible NLTE core and good spectra, yielding an RV accuracy of 2 km s^{-1} or better. We excluded targets with a gravity below 7.8. Lower gravity white dwarfs have lower density atmospheres, which would result in smaller effects. We selected the first 100 objects fulfilling these criteria from our catalogue with a total of 201 spectra between them (high S/N 100; H100).

Our measurements of the H100 sample are summarised in Table A.1. We first determined the offsets between H α and H β measured over the $\pm 15 \text{ \AA}$ interval, i.e. in the same fashion as our original measurements, only that we then included both lines in a simultaneous fit. The result is a very small systematic difference between both lines of -0.8 km s^{-1} . The offset increased to -2.5 km s^{-1} when we increased the fitted interval to $\pm 30 \text{ \AA}$. It can be expected that the largest signal is still delivered by the resolved Doppler broadened NLTE core. We thus convolved the model spectra with a Gaussian of 3 \AA FWHM, which smoothes the core away and tweaked the fit process to give small weights to the Doppler core. This procedure now gives the results from measuring the Stark broadened wings only. The offset between H β and H α increases to -8.7 km s^{-1} .

Somewhat surprisingly we measure on average smaller RVs for H β than for H α , i.e. blueshifts not redshifts as predicted by Halenka et al. (2015). However, let us keep in mind that the fit process includes a normalisation of model and observed spectrum. It is well possible that this will cancel out, or maybe, even overcompensate line asymmetries. Halenka et al. (2015) carried out a normalisation of their model spectra, but used the true continuum for this exercise. The FITSB2 normalisation process, as applied for our measurements, restricts itself to the fitted region. An asymmetry in the outer wings of the line, if present, will thus result in a tilt.

A detailed investigation is beyond the scope of this article. Our main interest here is an estimate of possible systematic offsets of our RVs. The small RV offset between H α and H β measurements for our H100 sample done the standard way over the $\pm 15 \text{ \AA}$ interval gives us confidence that the systematic RV errors for white dwarfs with well developed NLTE cores is not larger than 1 km s^{-1} . Note also the good agreement between our RVs measured from Balmer lines and the Ca K line (Fig. 7).

We used the best guess RVs (RV_{best}) from Table B.1 as reference point to get an estimate of systematic offsets for RVs measured using the $\pm 30 \text{ \AA}$ interval. We fitted RVs of our H100 sample over $\pm 30 \text{ \AA}$, combining H α and H β , the NLTE core smoothed away. The average difference to RV_{best} is -3.7 km s^{-1} .

We actually do not know RV_{best} for DA targets with weak NLTE cores, for which we needed to use a wider fit interval. However, we made an attempt to measure the differences between H α and H β RVs. Uncertainties are quite substantial due to the weak features of these spectra. These measurements also produced a few outliers, a tendency which is much reduced if both Balmer lines are combined. This is the main reason we included H β for our RV measurements in the first place. To avoid spurious results we excluded spectra with an uncertainty of the RV difference exceeding 15 km s^{-1} . The average of the remaining 31 measurements has an RV offset of $-14.6 \pm 2.6 \text{ km s}^{-1}$. This is larger than what we measured for our H100 sample with smoothed NLTE core. It is plausible that the generally weaker features of these stars increase the impact of line asymmetries or other systematics. Assuming that the pattern observed for the H100 sample holds, we estimate that the systematic error for the simultaneous fit of H α and H β amounts to about -7 km s^{-1} .

In summary we estimate that systematic offsets of the DAs with prominent NLTE cores (the vast majority) should not exceed 1 km s^{-1} , for targets with weak Doppler cores a systematic offset of about 7 km s^{-1} is possible. These are small enough that they will have no impact on the *relative* RV measurements at different epochs, but need to be considered for *absolute* RVs.

Appendix B: Radial velocity measurements for all DA white dwarfs

Table B.1 lists all RV measurements of the DA white dwarfs in the SPY sample.

Column 1 gives the designation. "WD" indicates that this source was selected from the McCook & Sion (1999) version of the WD catalogue. Other designations indicate that other sources were used (see text).

Column 2. Julian date. The dates are for mid-exposure and corrected to heliocentric values.

Column 3. Individual heliocentric RV measurements for the epochs. If photospheric Ca II lines were present, the Ca K lines was included in the measurement. Observations done under poor conditions (usually repeated afterwards) are included in this table. Errors are often large due to poor signal to noise levels, but could carry useful phase information.

Column 4. Wavelengths range used for the RV measurements, shifted according to the measured RV. An empty entry indicates the standard $\pm 15 \text{ \AA}$ interval. Larger values were used, when a sharp line core was missing (see text). Sometimes an asymmetric range was chosen to avoid flaws in the spectra.

Column 5. Weighted average of the RV measurements. The error is computed including the estimate for instrumental systematics calculated from the telluric lines and comparison between Ca and H lines when present.

Column 6. χ^2 values computed for the null hypothesis that RV is constant. Again, our estimates for the systematic errors are included.

Column 7. The next column gives the probability p that χ^2 has a value as high as the measured one or higher for an RV constant star. The smaller the values the higher the confidence that the star is RV variable.

Column 8. A binary is assumed for probability $\log p < -4$ and marked as DD in this column. Double-lined systems not exceeding our RV variation threshold, but identified by visual inspection are marked dd.

Column 9. Comments and observations. Abbreviations:

SB2: Double-lined DD.

G&L: Model spectrum modified using one or more Gaussians and Lorentzians (see text).

polyn.: Model spectrum modified using a low order polynomial.

v_{rot} : Rotation included in fit. That does not necessary indicate that the star is rotating. The aim was to achieve a good match of the observed profiles for fitting RVs without considerations of the physical soundness.

+Ca K: Photospheric Ca II present and included in fit.

Table B.1: RV measurements for the SPY DA white dwarfs.

object	HJD −2 400 000	RV km s ^{−1}	$\Delta\lambda$ Å	\overline{RV} km s ^{−1}	χ^2	$\log p$	comments
WD2359−434	51739.7790 51743.8041	49.6±1.4 47.7±1.5		48.7±1.1	0.40	−0.28	polyn., G&L, v_{rot}
WD2359−324	51740.7447 51742.8050 52799.9168	94.7±5.6 72.6±6.8 79.9±2.7		81.6±2.4	4.36	−0.95	
WD0000−186	51803.7127 51804.6533	25.3±1.7 23.3±1.7		24.2±1.3	0.36	−0.26	
HS0002+1635	52610.5530 52889.7085	18.2±2.1 15.2±1.7		16.4±1.4	0.63	−0.37	
WD0005−163	51803.6565 52490.9246	13.1±2.5 15.5±1.3		14.9±1.3	0.39	−0.27	G&L
WD0011+000	51739.8071 51742.8241	23.2±1.0 26.0±1.4		24.2±1.0	1.12	−0.54	polyn., G&L
WD0013−241	51803.6229 51804.5870	18.6±1.2 16.1±1.1		17.3±0.9	1.08	−0.52	
WD0016−258	51803.6345 51804.5991	50.4±2.2 44.5±3.5		48.7±1.9	1.14	−0.54	polyn., G&L
WD0016−220	51803.7254 51804.6667	16.3±0.8 12.7±0.9		14.7±0.7	3.34	−1.17	polyn.
WD0017+061	52535.6847 52543.8234	−5.5±2.3 −1.7±2.4		−3.7±1.7	0.70	−0.40	
WD0018−339	52532.6001 52535.6130	36.3±0.9 32.5±1.2		34.8±0.8	2.83	−1.03	
WD0024−556	51759.8949 51761.8611	96.1±2.2 90.3±1.0		91.5±1.0	2.97	−1.07	polyn., G&L
WD0027−636	52482.7523 52501.9075	28.1±6.2 32.4±5.7	40.0 40.0	30.4±4.2	0.16	−0.16	
WD0028−474	52212.7174 52272.5402	−45.2±2.8 83.0±1.4		54.0±1.4	885.20	<−100	DD SB2, G&L
WD0029−181	52543.8594 52544.7685	43.5±3.5 44.6±1.5		44.4±1.5	0.05	−0.08	
HE0031−5525	52482.7623 52260.5382	57.1±2.6 57.8±4.1		57.3±2.2	0.01	−0.04	polyn., G&L
MCT0031−3107	51803.6896 52114.9154	56.1±25.8 7.7±13.9	40.0 40.0	18.5±12.2	1.60	−0.69	
HE0032−2744	52532.6336 52535.6383	52.9±2.7 50.5±3.1		51.8±2.1	0.19	−0.18	
WD0032−317	51803.6666 51804.6223	18.6±4.3 48.4±4.2	30.0 30.0	33.8±3.0	14.00	−3.74	
WD0032−175	52535.6469 52542.7792	32.5±0.8 34.9±1.0		33.5±0.8	1.28	−0.59	G&L
WD0032−177	52535.6549 52542.7603	11.0±1.8 17.5±1.5		14.8±1.3	3.78	−1.29	
WD0033+016	52535.7879 52543.8407	88.9±2.1 92.3±1.9		90.7±1.5	0.75	−0.41	G&L
MCT0033−3440	51803.7006 52501.9203	53.0±2.7 52.9±1.2		52.9±1.2	0.00	−0.01	
WD0037−006	52610.5622 52655.5401 52889.7276	−62.6±1.0 71.4±1.6 −26.6±1.1		−22.4±0.8	2327.70	<−100	DD SB2, G&L
HE0043−0318	52610.5695 52655.5744	67.7±1.0 67.5±1.9		67.6±1.0	0.00	−0.02	G&L
WD0047−524	52482.7698 52531.6391	29.9±0.6 31.2±0.7		30.5±0.7	0.54	−0.34	polyn.
HS0047+1903	52536.7020 52544.7386 52889.7178	26.4±10.9 24.3±1.1 24.4±1.5		24.4±1.0	0.03	−0.01	
WD0048−544	52482.7774	32.8±0.9		31.7±0.7	1.03	−0.51	

Table B.1: RV measurements, continued.

object	HJD −2 400 000	RV km s ^{−1}	$\Delta\lambda$ Å	\overline{RV} km s ^{−1}	χ^2	$\log p$	comments
	52531.6468	30.8±0.8					
WD0048+202	52536.7120 52610.5968 52544.7290	31.7±2.1 32.1±1.1 32.4±1.0		32.2±0.8	0.05	−0.01	
HE0049−0940	52543.8699 52544.7781	28.7±0.9 29.6±0.6		29.3±0.7	0.23	−0.20	
WD0050−332	52163.6634 52482.7856 52532.6503 52542.7912	18.0±3.2 19.7±3.1 29.1±2.5 22.6±2.6	30.0 30.0 30.0 30.0	23.1±1.5	5.20	−0.80	
HS0051+1145	52536.7221 52544.7581	41.7±9.6 43.4±3.0		43.3±2.9	0.02	−0.05	G&L, ⁵
WD0052−147	52543.8800 52544.7880	58.1±1.6 59.4±1.6		58.7±1.2	0.17	−0.17	
WD0053−117	52543.8897 52544.7977	28.7±0.7 29.1±0.6		28.9±0.7	0.05	−0.08	G&L
WD0058−044	51738.8042 51741.8086	41.3±2.0 40.2±3.6		41.0±1.9	0.03	−0.07	G&L, ⁶
WD0101+048	52530.8546 52847.9008	48.4±0.6 63.6±0.8		55.0±0.7	75.98	−17.54	DD G&L, v_{rot}
WD0102−185	52675.5315 52849.9046	34.2±4.5 33.6±3.7	12.5/ 15.0	33.8±2.9	0.01	−0.03	⁷
WD0102−142	51761.9167 52529.8719	18.2±1.4 16.6±1.4		17.4±1.1	0.34	−0.25	polyn.
HE0103−3253	52532.6585 52542.7999	39.2±1.5 39.2±1.3		39.2±1.1	0.00	−0.00	
WD0103−278	52532.6684 52536.6069	45.3±0.9 48.3±3.2		45.6±1.0	0.46	−0.30	
MCT0105−1634	51739.7961 51742.8518 52883.6855	15.4±5.7 6.5±7.2 27.5±5.3		18.5±3.4	3.47	−0.75	
WD0106−358	51737.7759 51741.7823	35.3±2.5 36.7±3.1		35.8±2.0	0.07	−0.10	
HE0106−3253	51885.6255 52146.8722	56.6±1.1 55.0±0.7		55.6±0.8	0.59	−0.35	G&L
WD0107−192	51737.7847 51741.7897	−0.9±1.4 0.6±1.5		−0.2±1.1	0.25	−0.21	
WD0108+143	51739.8220 51743.8451	83.9±2.3 86.9±3.0		85.0±1.9	0.36	−0.26	
WD0110−139	51738.8143 51741.7991	40.4±2.3 38.0±2.8		39.4±1.8	0.25	−0.21	
MCT0110−1617	51761.9254 52529.8809	55.5±9.0 44.5±10.2	30.0 30.0	50.7±6.8	0.38	−0.27	
MCT0111−3806	52531.6579 52146.8888	25.2±2.1 32.2±3.1	30.0 30.0	27.5±1.8	1.97	−0.80	G&L
WD0112−195	51737.8432 51740.7732	−13.4±29.2 37.1±27.9	30.0 30.0	13.0±20.2	0.91	−0.47	
WD0114−605	52489.9160 52146.9060	57.4±1.9 62.2±2.3		59.4±1.6	1.36	−0.61	
WD0114−034	51737.8531 51740.7824	−14.5±10.4 0.6±2.7		−0.4±2.7	1.16	−0.55	
WD0124−257	51738.8246 51741.8302	35.4±2.7 30.4±2.2		32.4±1.8	1.12	−0.54	
WD0126+101	51739.8320	4.5±0.9		4.7±0.7	0.02	−0.05	polyn., G&L

⁵ magnetic⁶ magnetic⁷ flaws in 29/07/2003 spectrum

Table B.1: RV measurements, continued.

object	HJD −2 400 000	RV km s ^{−1}	$\Delta\lambda$ Å	\overline{RV} km s ^{−1}	χ^2	log p		comments
	51743.8535	4.8±0.8						
WD0127−050	52536.7368 52544.8056	5.3±2.2 2.8±0.8		3.2±1.0	0.58	−0.35		
WD0128−387	51738.8458 51741.8467	106.5±6.8 94.2±6.7	30.0 30.0	100.2±4.8	0.96	−0.48	dd	DAB, SB2
WD0129−205	51737.7955 51741.8565	62.7±1.9 58.7±1.6		60.4±1.3	1.25	−0.58		
HS0129+1041	52536.7453 52544.8133 53010.5779	56.8±3.3 60.2±1.1 60.5±2.2		59.9±1.1	0.55	−0.12		
HS0130+0156	52547.7017 52143.8779	43.1±12.9 30.0±11.2	40.0 40.0	35.6±8.4	0.35	−0.26		
HE0130−2721	52532.7033 52544.8226	27.3±2.3 34.3±2.2		31.0±1.6	2.59	−0.97		
HE0131+0149	52536.7538 52143.8946	24.4±1.7 6.5±1.0		11.8±1.0	39.46	−9.47	DD	
WD0133−116	51737.8129 51741.9056	98.8±1.4 96.3±1.0		97.3±1.0	0.91	−0.47		polyn., G&L
WD0135−052	51737.8611 51741.8696	−51.0±0.5 87.3±0.5		20.7±0.6	7888.70	<−100	DD	SB2, G&L
MCT0136−2010	51743.8630 51737.8046	91.8±1.7 94.9±2.1		93.1±1.4	0.67	−0.39	dd	SB2, polyn., G&L
MCT0138−4014	51761.8814 52532.8186	45.2±2.6 46.3±3.4		45.6±2.1	0.04	−0.07		
WD0137−291	51738.9372 51741.8785	29.6±2.6 26.9±2.3		28.1±1.8	0.33	−0.25		
WD0138−236	51739.8424 51741.8905	51.1±37.5 9.3±31.9	40.0 40.0	26.9±24.3	0.42	−0.29		
WD0140−392	51739.8513 51741.8996	57.2±0.7 57.0±0.8		57.1±0.7	0.02	−0.05		
WD0143+216	52536.7617 52847.9163	19.9±1.6 22.3±1.6		21.1±1.2	0.57	−0.35		polyn., G&L
WD0145−221	51740.7924 51742.8607	58.6±2.0 52.6±3.2		56.8±1.8	1.40	−0.63		polyn., G&L
WD0145−257	52536.6432 52544.8467	43.2±4.2 37.6±1.5		38.3±1.5	0.89	−0.46		
HS0145+1737	52536.7741 52547.7218 53010.5692	19.8±2.4 25.7±1.1 23.1±0.9		23.7±0.8	3.07	−0.67		
HE0145−0610	52658.5542 52658.5679 52903.6836	58.3±2.9 56.8±4.1 57.6±1.6		57.7±1.4	0.05	−0.01		polyn., G&L
HS0146+1847	52536.7879 52547.7314 53010.5598	−0.7±12.8 14.4±2.7 12.5±3.5		13.3±2.2	0.82	−0.18		polyn., G&L, v_{rot}
HE0150+0045	52675.5430	−0.1±2.8		−0.1±2.9	0.00	0.00		
WD0151+017	51737.8676 51740.8441	60.6±2.0 65.4±1.3		63.9±1.2	2.10	−0.83		
HE0152−5009	52532.8818 52544.8530	53.9±1.1 51.7±1.3		52.9±1.0	0.76	−0.42		polyn.
WD0155+069	52536.7996 52658.5879	1.2±2.3 2.7±1.6		2.2±1.4	0.15	−0.15		
WD0158−227	52537.6611 52544.8324	2.7±5.2 0.5±2.8	30.0 30.0	1.0±2.5	0.08	−0.11		G&L
HE0201−0513	52537.6945	8.6±3.1		8.6±3.1	0.00	0.00		
HS0200+2449	52535.8178 52656.5503	55.0±1.7 52.9±2.1		54.2±1.4	0.31	−0.24		
WD0204−233	51740.8270	98.8±1.0		98.3±1.1	1.06	−0.52		polyn.

Table B.1: RV measurements, continued.

object	HJD −2 400 000	RV km s ^{−1}	$\Delta\lambda$ Å	\overline{RV} km s ^{−1}	χ^2	log p	comments
	51742.8701	93.9±3.4					
HE0204−3821	52165.8909 52527.8696	32.3±3.1 36.8±1.2		36.1±1.3	0.98	−0.49	
HE0204−4213	52532.8917 52537.7137	22.8±2.2 22.1±2.5		22.4±1.7	0.02	−0.06	
WD0204−306	52611.7406 52611.7485 52616.7588 52851.8964	96.1±9.3 92.2±8.6 82.3±5.4 69.0±6.1		81.5±3.4	4.80	−0.73	polyn., G&L, v_{rot}
WD0203−138	51740.8365 51742.8804 53010.6421	28.4±34.7 −13.6±21.4 −44.4±35.4	40.0 40.0 40.0	−10.9±16.2	1.29	−0.28	G&L
WD0205−365	51737.8844 51740.8035	48.9±5.4 39.7±5.6	40.0 40.0	44.4±3.9	0.81	−0.44	G&L
WD0205−304	51802.7396 52175.8668	79.6±1.5 79.9±1.1		79.8±1.0	0.02	−0.05	
HE0205−2945	52175.8788 52532.8291	53.9±5.4 14.2±5.4		34.0±3.9	15.42	−4.07	DD SB2, G&L
WD0208−263	52532.9022 52537.7245	87.3±8.0 70.5±5.5	30.0 30.0	76.0±4.6	1.73	−0.72	
HS0209+0832	51737.8914 51737.8983 51740.8102	80.7±3.9 77.1±3.6 67.8±6.3	30.0 30.0 30.0	77.1±2.5	1.76	−0.38	G&L
HE0210−2012	52174.8880 52527.8802	36.2±1.2 38.4±1.4		37.2±1.0	0.67	−0.38	
HE0211−2824	51885.6492 51947.5400	56.6±0.9 57.1±0.9		56.9±0.8	0.06	−0.09	
WD0212−231	52537.7352 52616.7393	42.9±2.7 44.2±4.3		43.3±2.3	0.04	−0.08	
HS0213+1145	52536.8292 52655.5866 53010.6258	85.8±5.4 71.6±3.9 79.4±3.2		78.0±2.3	2.86	−0.62	
WD0216+143	51802.7697 52522.9057	20.8±2.4 −0.4±1.7		6.7±1.5	27.27	−6.75	DD
HE0219−4049	52139.9124 52522.8971 52165.8662 52171.8893	40.5±1.9 45.5±1.5 41.9±1.9 39.5±1.5		42.1±0.9	4.46	−0.67	
HE0221−2642	52175.8899 51949.5680	42.1±3.3 54.8±6.1	30.0 30.0	45.1±3.0	1.94	−0.79	
WD0220+222	52639.5488	67.6±1.2		67.6±1.4	0.00	0.00	
HE0221−0535	52536.8421 52537.7563	33.1±5.3 45.0±1.7		43.7±1.7	2.59	−0.97	⁸
HE0222−2336	52537.7666 52616.7493	21.4±4.4 25.5±6.1	30.0 30.0	22.8±3.6	0.17	−0.17	
HE0222−2630	52465.8944 51949.5788	59.9±1.4 63.9±3.1		60.7±1.4	0.74	−0.41	
HS0223+1211	52639.5612	−50.9±5.9		−50.9±5.9	0.00	0.00	G&L
HE0225−1912	52544.8831 52537.7775	−115.9±2.1 −66.8±2.5		−95.0±1.7	123.77	−28.02	DD SB2
HS0225+0010	52537.8495 52639.5819	29.7±1.9 27.0±1.9		28.3±1.4	0.55	−0.34	
WD0226−329	52536.6740 52611.7684 52616.7667	20.1±1.6 19.7±1.4 22.9±0.7		21.6±0.7	2.47	−0.54	
WD0227+050	52536.8499 52656.5650	16.8±0.5 15.7±0.5		16.5±0.5	0.74	−0.16	G&L

⁸ H α core corrupted in one spectrum

Table B.1: RV measurements, continued.

object	HJD −2 400 000	RV km s ^{−1}	$\Delta\lambda$ Å	\overline{RV} km s ^{−1}	χ^2	$\log p$	comments
	52882.8934	16.8±0.4					
WD0229−481	51759.9005 51761.8667 53010.6148	37.0±3.5 16.6±5.1 26.4±9.1	40.0 40.0 40.0	30.0±2.8	6.25	−1.36	
WD0230−144	52465.9030 52536.6836	25.5±3.8 24.1±11.2		25.3±3.7	0.01	−0.03	G&L, ⁹
WD0231−054	51737.8733 52523.9105 51740.8171	92.4±1.5 89.3±2.2 85.4±3.0		90.5±1.2	2.65	−0.57	polyn., G&L
HS0237+1034	52537.8687	80.6±4.1		80.6±4.2	0.00	0.00	dd SB2
WD0239+109	51737.9060 51740.8610	6.1±4.3 6.6±4.2		6.3±3.0	0.00	−0.02	G&L, v_{rot} , ¹⁰
HS0241+1411	52537.8789	13.7±2.8		13.7±2.9	0.00	0.00	
WD0242−174	52260.5925 53010.6088	38.8±1.1 39.4±1.1		39.1±0.9	0.06	−0.10	
WD0243+155	52537.8883	27.4±1.7		27.4±1.8	0.00	0.00	
WD0243−026	51949.5403 52530.8611	35.4±1.5 27.5±0.9		30.1±0.9	9.15	−2.60	G&L, v_{rot}
HE0245−0008	52655.6160	75.2±2.2		75.2±2.3	0.00	0.00	
HE0246−5449	52537.7922 52539.7079	29.5±1.9 32.5±1.4		31.4±1.2	0.80	−0.43	
WD0250−026	52465.9164 52536.8655	57.8±0.9 57.1±1.2		57.5±0.9	0.10	−0.13	
WD0250−007	52674.5447 52655.6263	57.0±1.5 53.4±2.3		55.8±1.3	0.94	−0.48	polyn., G&L
WD0252−350	51740.8527 51741.9402	102.1±1.4 95.7±1.0		98.0±0.9	6.10	−1.87	
WD0255−705	51759.9173 51761.8723	85.0±1.5 83.5±1.1		84.1±1.0	0.28	−0.23	G&L
HE0255−1100	51949.5289 52537.8159	−2.5±2.7 −6.5±2.3		−4.8±1.8	0.67	−0.39	
HE0256−1802	52537.8259 52616.7756	20.7±2.5 28.1±3.0		23.7±2.0	1.96	−0.79	
HE0257−2104	52537.8365 52616.7856	33.2±2.0 34.4±1.6		33.9±1.3	0.11	−0.13	
WD0257+080	52535.8275 52639.6042	46.6±2.5 48.5±2.3		47.6±1.7	0.16	−0.16	G&L, ¹¹
HE0300−2313	51884.5990 51885.6615	68.9±1.8 58.7±3.5		66.6±1.7	3.70	−1.26	
WD0302+027	51741.9203 51743.8688	23.2±4.4 37.8±5.3	30.0 30.0	29.2±3.4	2.61	−0.97	
HE0303−2041	52538.7983 52544.8919	42.4±1.7 43.4±1.5		43.0±1.2	0.10	−0.13	G&L
HE0305−1145	51889.6282 51948.5414 51947.5515	47.4±9.5 45.5±3.1 50.9±3.3		48.0±2.3	0.80	−0.17	
WD0307+149	52535.8768 52536.8833	7.8±0.8 1.1±3.3		7.2±1.0	2.17	−0.85	
HS0307+0746	52538.8286 52674.5564	16.2±2.3 13.7±2.1		14.9±1.6	0.34	−0.25	
WD0310−688	52536.8909 52611.7249 52611.7292 52616.7908	63.1±0.4 62.5±0.3 62.5±0.3 62.5±0.3		62.6±0.4	0.26	−0.01	G&L
HE0308−2305	51949.5584	76.6±1.9		74.4±1.5	1.43	−0.63	

⁹ fit without model spectrum¹⁰ magnetic¹¹ magnetic, second component possibly visible in higher Balmer lines

Table B.1: RV measurements, continued.

object	HJD −2 400 000	RV km s ^{−1}	$\Delta\lambda$ Å	\overline{RV} km s ^{−1}	χ^2	$\log p$	comments
	51947.5749	72.0±2.0					
WD0308+188	52538.7370 52656.5728	38.1±0.7 38.7±0.9		38.4±0.7	0.10	−0.12	
HS0309+1001	52332.5254 52530.8718	105.3±3.4 88.8±2.0		93.4±1.8	9.64	−2.72	polyn., G&L
WD0315−332	52538.8455 52539.7208 52852.8993	80.5±18.2 76.2±21.0 6.6±12.2	40.0 40.0 40.0	38.2±9.1	8.98	−1.95	G&L
HS0315+0858	52538.8566 52539.7315	46.4±1.2 47.4±1.2		47.0±1.0	0.16	−0.16	
HE0315−0118	51947.5839 51949.5505	−5.0±1.6 119.8±2.0		46.1±1.3	1220.82	<−100 DD	SB2
HE0317−2120	51946.6365 51947.5922	45.8±3.0 48.6±1.6		47.9±1.5	0.36	−0.26	G&L
WD0317+196	52538.7468 53013.5370	61.8±1.1 62.5±1.1		62.1±0.9	0.08	−0.11	
WD0318−021	52334.5292 52336.5398	40.0±2.1 39.9±2.6		40.0±1.7	0.00	−0.01	G&L
WD0320−539	51759.9224 51761.8889 52851.9080	79.1±5.9 56.6±4.0 56.5±2.7	30.0 30.0 30.0	59.4±2.1	7.32	−1.59	
HE0320−1917	51946.6478 51947.6130	81.9±3.5 12.1±1.4		23.2±1.4	191.70	−42.87 DD	
HE0324−2234	52338.5233 52531.8996	53.4±1.7 53.4±1.9		53.4±1.3	0.00	−0.00	
HE0324−0646	52332.5359 52337.5190	39.9±1.1 41.5±1.6		40.5±1.0	0.30	−0.23	
HE0324−1942	52538.8670 52539.7409	−28.5±8.3 68.7±9.7		12.9±6.3	33.64	−8.18 DD	SB2
HE0325−4033	52538.8773 52539.7503	63.1±2.1 87.7±1.8		77.4±1.4	41.21	−9.86 DD	G&L, ¹²
HS0325+2142	52538.7574 53013.5492	71.8±0.9 70.1±1.0		71.0±0.8	0.62	−0.37	polyn.
WD0326−273	51737.9246 51740.8767	148.6±0.6 −29.0±0.6		56.2±0.6	>10000	<−100 DD	polyn., G&L
WD0328+008	52539.7624 52658.6826	21.3±8.5 −8.8±43.0	30.0 30.0	20.1±8.4	0.28	−0.22	
HE0330−4736	51885.6729 51891.7954	48.5±2.4 42.1±1.7		44.3±1.5	2.55	−0.96	
HS0329+1121	52539.7734 53013.6063	8.4±2.0 10.3±1.3		9.6±1.2	0.32	−0.24	
WD0330−009	52538.6954 52655.5992	5.6±5.8 −0.9±3.8	30.0 30.0	1.1±3.2	0.50	−0.32	
HS0331+2240	52538.7663 52862.9178	35.2±2.3 36.3±1.9		35.8±1.5	0.07	−0.11	
HE0333−2201	51889.6664 51924.6052	55.2±1.6 51.5±1.1		52.9±1.0	1.74	−0.73	
HE0336−0741	52336.5511 52334.5399	67.4±2.3 68.6±3.2		67.8±1.9	0.05	−0.09	
WD0336+040	52539.7831 52695.5555 52853.9183 53013.6166	77.0±4.8 75.8±3.7 68.4±2.2 71.0±2.7		71.3±1.5	2.59	−0.34	G&L
HS0337+0939	52539.7927 52674.5670	73.3±2.1 69.1±2.1		71.2±1.6	1.05	−0.52	
HE0338−3025	52170.8792	16.6±2.1		20.5±1.5	3.38	−1.18	G&L

¹² fit unusually poor, possibly composite spectrum

Table B.1: RV measurements, continued.

object	HJD −2 400 000	RV km s ^{−1}	$\Delta\lambda$ Å	\overline{RV} km s ^{−1}	χ^2	$\log p$	comments
	52171.8989	23.9±2.0					
WD0339−035	51740.8991 52530.8810	82.5±1.2 75.0±1.3		79.2±1.0	8.06	−2.35	polyn., G&L
WD0341+021	52337.5299 52538.7061	−49.0±2.1 73.0±1.3		35.9±1.2	1201.59	<−100	DD
WD0343−007	51889.6787 51891.6840	21.8±23.6 10.4±14.3	40.0 40.0	13.5±12.2	0.10	−0.12	
WD0344+073	52324.5280 52539.8020 52659.6652	−48.2±5.1 39.6±5.0 14.9±9.2		−1.5±3.4	88.72	−19.26	DD polyn., G&L
HS0344+0944	52539.8117 52674.5777	51.3±2.3 51.8±11.1		51.3±2.3	0.00	−0.01	
HE0344−1207	51946.6268 51947.6243	51.3±6.5 26.9±3.4		32.3±3.0	6.48	−1.96	
HS0345+1324	52539.8221 52695.5333	63.1±3.3 66.8±5.8		64.1±2.9	0.18	−0.17	
WD0346−011	51741.9278 51743.8742	171.3±8.8 178.2±5.7	40.0 40.0	176.2±4.8	0.26	−0.21	
HS0346+0755	52674.5878 52695.5445	48.4±2.9 53.3±5.0		49.7±2.6	0.43	−0.29	
HE0348−4445	51802.7774 51804.8405	51.6±3.5 55.0±2.5		53.8±2.1	0.35	−0.26	
HE0348−2404	52166.9007 52167.8889	47.3±1.7 48.2±1.3		47.8±1.1	0.09	−0.11	polyn.
HE0349−2537	51889.6558 51924.5781	15.0±2.4 16.7±2.2		15.9±1.7	0.15	−0.16	
WD0352+049	52658.6570 52674.6257	131.3±22.0 92.6±25.1	40.0 40.0	114.5±16.6	0.79	−0.43	
WD0352+052	52334.5508 52530.8999	−71.7±2.4 −78.5±2.9		−74.4±1.9	1.80	−0.75	G&L
WD0352+018	52332.5539 52538.7174	85.2±2.0 83.2±2.4		84.3±1.6	0.23	−0.20	
WD0352+096	52324.5378 52538.7292	81.4±0.7 83.0±1.0		82.1±0.8	0.61	−0.36	
HE0358−5127	51740.9117 51742.9080 51743.8849	40.2±2.1 46.9±22.6 37.9±2.0		39.0±1.5	0.42	−0.09	
WD0357+081	51802.7890 51804.8644	4.2±5.5 −10.0±5.6		−2.8±4.0	1.89	−0.77	G&L, v_{rot}
HS0400+1451	52337.5428 52538.7853	86.0±1.1 88.5±0.7		87.6±0.8	1.52	−0.66	
HS0401+1454	52674.6161	11.1±2.0		11.1±2.1	0.00	0.00	polyn., G&L
HE0403−4129	51740.9212 51743.8944	33.1±3.2 33.9±3.9		33.4±2.5	0.02	−0.05	
HE0404−1852	51895.7564 53010.6975	41.6±1.8 38.8±1.8		40.2±1.4	0.62	−0.37	
WD0406+169	52674.6065 53013.5731	91.9±1.8 90.4±1.2		90.9±1.1	0.23	−0.20	polyn.
WD0407+179	52674.5976 52695.5677 52882.9005	61.7±0.6 63.7±1.1 61.2±0.6		61.9±0.6	1.52	−0.33	G&L
WD0408−041	51802.8997 52154.8915	19.4±1.1 17.8±1.4	10.0/ 15.0 10.0/ 15.0	18.7±1.0	0.36	−0.26	G&L, +CaK
HE0409−5154	51802.8873 52165.8996 52258.7855	65.4±2.5 66.8±3.5 75.3±3.4		68.4±1.8	3.18	−0.69	
HE0410−1137	52334.5615 52338.5410	6.6±1.6 53.5±1.9		26.7±1.3	181.46	−40.63	DD SB2, G&L

Table B.1: RV measurements, continued.

object	HJD −2 400 000	RV km s ^{−1}	$\Delta\lambda$ Å	\overline{RV} km s ^{−1}	χ^2	$\log p$	comments
WD0410+117	52332.5634 52657.6788	54.0±0.9 52.6±0.8		53.2±0.7	0.51	−0.32	
HS0412+0632	52324.5473 52657.6865	32.8±1.1 34.5±1.2		33.6±0.9	0.48	−0.31	
HE0414−4039	51889.7071 51895.7438	70.8±3.2 60.8±3.7		66.5±2.4	2.40	−0.92	
WD0416−550	51743.9146 51759.9082 53010.6519	33.8±2.0 20.0±4.8 28.6±1.5		29.8±1.2	4.80	−1.04	
HE0416−3852	51889.6953 51895.7331	55.1±3.6 50.1±2.8		52.0±2.2	0.69	−0.39	
HE0416−1034	51895.7673 51924.6338	69.1±1.4 69.0±1.8		69.1±1.2	0.00	−0.01	
HE0417−3033	52271.6052 52532.8503	59.0±2.0 64.9±2.9		61.0±1.7	1.56	−0.67	
HE0418−5326	51743.9240 51761.8952	11.3±4.7 10.5±3.5		10.8±2.9	0.01	−0.04	
HE0418−1021	52530.8897 52270.6897	71.5±2.2 70.8±2.4		71.2±1.7	0.02	−0.05	
WD0421+162	52332.5713 52639.6382	75.2±1.5 75.4±1.0		75.3±1.0	0.01	−0.03	polyn.
HE0423−2822	52247.7771 52540.7808 52271.5931	68.5±9.8 88.1±7.3 37.5±14.9		75.3±5.5	5.81	−1.26	polyn., G&L, v_{rot} , ¹³
HS0424+0141	52334.5720 52337.5543	104.8±16.8 56.6±18.0	40.0 40.0	82.4±12.3	2.23	−0.87	
HE0425−2015	52540.8003 52542.8733	55.2±2.1 61.1±3.2		57.1±1.8	1.28	−0.59	
WD0425+168	52639.6446 52650.6922	73.7±0.8 78.1±1.5		75.0±0.9	2.93	−1.06	
HE0426−1011	52338.5515 52540.8223	73.4±1.0 76.3±1.1		74.7±0.9	1.69	−0.71	polyn., ¹⁴
WD0426+106	52540.8431 52657.7080	79.9±4.5 65.5±10.0		77.5±4.1	1.00	−0.50	polyn., G&L
HE0426−0455	51889.6415 51889.6466 51885.7860	15.1±8.2 24.9±1.1 25.2±1.1		25.0±0.9	0.87	−0.19	
WD0431+126	52658.6662 52659.6916	72.6±1.4 74.9±1.4		73.7±1.1	0.62	−0.37	
HE0436−1633	52315.5722 52540.8781	29.2±1.3 25.5±1.1		27.2±1.0	2.13	−0.84	
WD0437+152	52658.6739 52662.6347	21.1±2.0 19.4±2.2		20.3±1.5	0.19	−0.18	
WD0440−038	52315.5617 52657.7179	168.0±12.6 224.4±18.1	40.0 40.0	186.4±10.4	3.80	−1.29	G&L
WD0446−789	52611.7553 52608.7974	35.7±1.2 35.7±0.7		35.7±0.8	0.00	−0.00	
HE0452−3429	52331.6357 52338.5621	59.7±2.8 64.8±0.9		64.2±1.0	1.62	−0.69	
HE0452−3444	51924.6198 51891.7758	23.8±1.9 27.4±1.5		26.0±1.2	1.15	−0.55	
WD0453−295	52213.8622 52247.8269 52260.6734	109.3±2.9 149.7±2.3 44.0±1.5	30.0 30.0 30.0	83.7±1.2	852.53	<−100 DD	DAB, SB2
HE0455−5315	52247.8136 52331.6244	−73.3±8.7 −29.3±6.0		40.6±3.2	304.76	−66.18 DD	

¹³ possible second component in spectrum¹⁴ model fit relatively poor, possible second component

Table B.1: RV measurements, continued.

object	HJD −2 400 000	RV km s ^{−1}	$\Delta\lambda$ Å	\overline{RV} km s ^{−1}	χ^2	$\log p$	comments
	52532.8692	102.6±4.2					
WD0455−282	51801.8532 52260.6835	86.5±7.6 67.6±3.4	40.0 40.0	70.9±3.2	2.99	−1.08	G&L
HE0456−2347	52315.5495 52331.6583 53011.6811	36.4±2.3 40.0±3.7 35.6±5.6		37.2±1.9	0.44	−0.09	
HS0503+0154	52258.8346 52327.5268 53013.5844	15.7±20.7 15.9±8.8 3.3±11.6	40.0 40.0 40.0	11.7±6.7	0.46	−0.10	
HE0507−1855	51802.8594 51804.8497	64.3±6.2 50.4±4.4		55.1±3.6	1.94	−0.79	
HS0507+0434B	52214.8576 52327.5399 52650.7089 52258.8051	28.8±5.2 36.3±2.4 47.2±2.3 42.9±2.7		41.3±1.4	9.51	−1.63	polyn., G&L
HS0507+0434A	52331.6158 52337.5644 52258.8133 52658.6118	37.1±1.1 37.0±0.8 36.1±1.0 39.2±1.5		37.1±0.6	1.35	−0.14	
HE0508−2343	52006.5174 52008.5351	120.9±1.5 118.2±2.5		120.2±1.4	0.46	−0.30	
WD0509−007	51801.8672 52258.8207	27.7±2.5 26.4±3.0		27.1±2.0	0.07	−0.10	
WD0510−418	52213.8426 52247.8405 52327.5614 52852.9103	19.7±39.0 53.3±29.9 −18.1±20.3 36.9±6.3	40.0 40.0 40.0 40.0	32.5±5.9	4.25	−0.63	
WD0511+079	51802.8316 52154.9008	19.4±3.0 20.1±4.0		19.7±2.4	0.01	−0.04	G&L, v_{rot}
HE0516−1804	51884.8149 51885.8515	49.8±13.7 25.8±3.1		26.9±3.1	1.70	−0.72	polyn., G&L, ¹⁵
WD0518−105	51891.7526 51924.6599	128.9±17.1 131.4±9.3	40.0 40.0	130.9±8.2	0.01	−0.04	
HE0532−5605	51802.8488 51803.8974	75.7±3.4 72.0±3.8		74.1±2.6	0.31	−0.24	polyn., G&L, v_{rot}
WD0548+000	51802.8700 51803.9061	74.6±19.3 94.9±11.4	40.0 40.0	89.6±9.8	0.48	−0.31	G&L
WD0549+158	52295.6043 52542.8816 52324.5980	27.7±1.3 35.3±1.4 27.2±1.3		30.0±0.9	10.76	−2.34	G&L
WD0556+172	52295.6138 52326.5417	85.9±1.3 79.3±1.5		82.8±1.1	5.31	−1.67	
WD0558+165	52295.6248 52326.5531	78.9±1.4 80.3±1.2		79.7±1.0	0.29	−0.23	
WD0603−483	51884.8434 51924.6708 51944.7519	58.4±14.5 47.3±9.1 74.7±16.0	30.0 30.0 30.0	55.1±7.0	1.33	−0.29	
WD0612+177	52322.6775 52324.6056	47.3±1.0 46.9±0.7		47.1±0.7	0.05	−0.08	
WD0621−376	51801.8757 52006.5520	33.5±0.8 32.4±0.6	30.0 30.0	32.9±0.7	0.44	−0.30	G&L
WD0628−020	52632.8579 52637.7947	108.4±1.2 107.0±1.2		107.7±1.0	0.28	−0.23	G&L
WD0630−050	51885.8077 51888.8405	3.5±16.9 49.7±15.1	40.0 40.0	29.2±11.3	2.43	−0.92	
WD0642−285	52007.5556	44.1±1.7		44.1±1.8	0.00	0.00	
WD0646−253	52007.5639	70.9±1.0		69.0±0.9	3.48	−1.21	

¹⁵ H α core of "a" spectrum corrupted

Table B.1: RV measurements, continued.

object	HJD −2 400 000	RV km s ^{−1}	$\Delta\lambda$ Å	\overline{RV} km s ^{−1}	χ^2	$\log p$	comments
	52231.8497	66.6±1.1					
WD0659−063	51884.8578 51895.8489 51885.8277	28.2±0.8 29.1±5.3 27.7±1.6		28.1±0.9	0.06	−0.01	G&L
WD0710+216	52322.6880 52324.6158	40.8±2.0 35.2±1.1		36.7±1.1	3.15	−1.12	G&L
WD0715−703	52006.5612 52033.4908	7.2±6.2 7.3±10.6	40.0 40.0	7.2±5.4	0.00	−0.00	G&L, v_{rot}
WD0721−276	52008.5477 52033.4765	9.2±10.3 6.9±6.5	30.0 30.0	7.5±5.5	0.02	−0.05	
WD0732−427	52008.5557 52033.4983	92.2±0.8 90.9±1.6		91.8±0.9	0.23	−0.20	G&L
WD0752−676	52008.5629 52033.5068	92.3±1.5 94.2±1.6		93.2±1.2	0.36	−0.26	polyn., G&L, v_{rot}
WD0810−728	52008.5781 52033.5221 52033.5316	47.2±2.4 42.1±4.8 48.7±3.4		46.9±1.9	0.76	−0.17	
HS0820+2503	52663.6537 52688.6198	49.4±8.2 61.8±6.8	30.0 30.0	56.8±5.2	0.80	−0.43	
WD0830−535	52008.5942 52033.5506 52770.4835	39.5±2.3 45.0±5.0 42.4±2.5		41.3±1.7	0.73	−0.16	
WD0838+035	52322.7123 52326.5806	19.7±3.6 25.0±3.7	40.0 35.0/ 40.0	22.3±2.6	0.59	−0.36	G&L
WD0839−327	52008.6016 52033.5618	52.9±0.3 53.2±0.4		53.0±0.5	0.07	−0.10	G&L, v_{rot}
WD0839+231	52322.7217 52327.5967	−1.6±1.5 −2.0±1.9		−1.8±1.3	0.01	−0.04	
WD0852+192	52650.7402 52663.6723	23.7±2.1 21.5±2.0		22.5±1.5	0.32	−0.24	
WD0858+160	52663.7270 52689.6043	69.2±1.4 67.1±1.4		68.2±1.1	0.55	−0.34	
WD0859−039	52256.8531 52261.8292 52271.8497	5.1±0.6 3.0±1.2 5.0±0.8		4.6±0.6	1.15	−0.25	
WD0908+171	52329.6938 52635.8568	23.7±2.1 23.1±1.1		23.2±1.1	0.04	−0.07	
WD0911−076	51657.5806 51660.6279	56.7±1.3 54.5±1.7		55.8±1.2	0.52	−0.33	
WD0916+064	52008.6113 52033.5744 52033.5849 52992.7959	15.3±18.1 110.5±56.0 68.2±41.6 24.8±14.4	40.0 40.0 40.0 40.0	27.5±10.7	2.13	−0.26	
PG0922+162B	52320.7143 52327.6333	74.6±2.8 97.6±25.2		74.9±2.9	0.48	−0.31	
PG0922+162A	52322.7422 52327.6179	74.3±2.4 75.4±3.3		74.7±2.0	0.04	−0.08	
WD0922+183	52329.6812 52636.8425	35.8±3.9 29.6±2.2		31.1±2.0	1.04	−0.51	
WD0928−713	52044.5067 52258.7424 52258.7676 52387.6135	77.5±1.0 73.5±4.5 73.5±1.0 72.0±0.9		74.3±0.7	6.65	−1.08	G&L
HS0926+0828	52329.7058 52663.6819	52.5±2.9 46.2±2.8		49.2±2.1	1.38	−0.62	
HS0929+0839	52663.7362	39.3±2.0		40.8±1.9	1.12	−0.54	¹⁶

¹⁶ H α core of b spectrum corrupted

Table B.1: RV measurements, continued.

object	HJD −2 400 000	RV km s ^{−1}	$\Delta\lambda$ Å	\overline{RV} km s ^{−1}	χ^2	$\log p$	comments
	52690.5600	45.3±3.7					
HS0931+0712	52322.7528	22.8±15.1	30.0	18.1±9.9	0.10	−0.12	
	52327.6568	14.6±13.0	30.0				
HS0933+0028	52656.6680	31.4±13.6	40.0	38.6±6.7	0.22	−0.19	
	52663.6980	40.9±7.7	40.0				
HS0937+0130	52356.6246	47.9±3.7		43.1±2.4	1.66	−0.70	
	52636.8520	39.6±3.1					
WD0937−103	52322.7635	67.6±2.2		70.8±1.7	2.59	−0.97	
	52327.6866	75.0±2.6					
WD0939−153	51657.5924	41.6±1.3		40.9±0.9	0.22	−0.20	polyn.
	51660.6385	40.4±1.1					
HS0940+1129	52663.7462	72.4±2.5		70.0±1.9	1.04	−0.51	
	52690.5719	67.4±2.6					
HS0943+1401	52663.7555	46.8±2.0		46.9±1.9	0.00	−0.01	
	52695.5935	46.9±4.0					
HS0944+1913	52663.7650	66.2±0.8		67.3±0.8	1.74	−0.73	
	52695.5836	68.9±1.0					
WD0945+245	52317.6963	89.8±1.9		92.1±1.6	1.84	−0.76	polyn., G&L
	52327.6969	95.5±2.4					
HS0949+0935	52263.8412	35.9±3.7		35.0±2.6	0.05	−0.09	
	52327.7067	34.3±3.5					
HS0949+0823	52663.7756	29.5±3.2		29.3±1.4	7.80	−1.00	
	52663.7857	35.0±2.8					
	52684.6887	25.1±3.1					
	52684.6966	34.8±3.2					
	52992.7845	23.2±2.7					
WD0950+077	52009.5816	18.8±1.0		19.4±0.8	0.34	−0.25	
	52356.6573	20.1±1.0					
WD0951−155	51657.6033	31.7±1.7		28.3±1.2	3.41	−1.19	
	51660.6485	25.9±1.4					
WD0954+134	52328.6859	13.6±3.0		11.8±2.4	0.52	−0.33	
	52329.7169	9.1±3.6					
WD0955+247	52260.8537	58.7±0.9		57.6±0.7	1.07	−0.52	G&L
	52272.8556	56.7±0.7					
WD0956+045	51924.6892	61.8±2.4		65.5±1.2	1.78	−0.39	
	51924.7132	67.8±2.7					
	51946.6652	66.1±1.4					
WD0956+020	51657.6136	57.5±0.8		58.5±0.8	1.21	−0.57	
	51660.6641	60.0±1.2					
PG0959−085	51706.5129	42.1±6.7	30.0	42.9±5.1	0.02	−0.05	G&L
	51703.5093	44.0±7.9	30.0				
WD1000−001	52009.6047	72.9±2.0		72.5±1.8	0.07	−0.10	
	52033.6012	71.4±3.7					
WD1003−023	51924.7023	31.9±1.3		31.3±1.0	0.15	−0.15	
	51946.6753	30.9±1.2					
HS1003+0726	52418.5841	55.2±5.8		54.7±1.3	0.38	−0.08	
	52656.7130	53.9±1.6					
	53011.7997	56.2±2.3					
WD1010+043	52328.6974	64.1±4.8		61.0±3.5	0.51	−0.32	
	52329.7280	57.4±5.1					
HE1012−0049	51655.6269	25.2±2.0		26.0±1.8	0.32	−0.24	
	51681.4868	28.3±3.5					
HS1013+0321	52418.5953	37.5±2.6		38.0±1.6	0.03	−0.06	G&L
	52663.7072	38.3±2.0					
WD1013−010	52663.7957	183.4±1.0		168.0±0.9	176.49	−39.55	DD
	52684.7071	153.5±1.0					G&L, v_{rot}
WD1015−216	51655.6784	7.8±2.7		7.6±2.2	0.01	−0.03	
	51681.4990	7.3±3.7					

Table B.1: RV measurements, continued.

object	HJD −2 400 000	RV km s ^{−1}	$\Delta\lambda$ Å	\overline{RV} km s ^{−1}	χ^2	log p	comments
WD1015+076	51924.7469	16.4±8.4		16.4±8.4	0.00	0.00	
WD1015+161	52322.7865 52327.7170	63.9±1.5 66.1±0.9		65.4±0.9	0.78	−0.42	
WD1017−138	52387.6762 52656.7210	49.3±3.4 50.4±2.6	30.0 30.0	50.0±2.1	0.04	−0.08	
WD1017+125	51924.7369 51939.8475	8.9±1.7 18.3±1.8		13.5±1.3	7.50	−2.21	
WD1019+129	51924.8406 51939.8575	70.8±1.5 67.4±1.1		68.7±1.0	1.61	−0.69	
WD1020−207	51655.6891 51681.5085	77.1±0.9 77.2±1.4		77.1±0.9	0.00	−0.00	
WD1022+050	51919.8946 53013.8146	103.8±1.5 25.1±1.0		52.7±1.0	841.49	<−100	DD polyn., G&L
WD1023+009	52330.7550 52656.7033	33.9±6.5 34.5±13.1	40.0 40.0	34.0±5.8	0.00	−0.01	
WD1026+023	52009.7189 52418.6043 52656.7276	16.9±1.0 14.4±1.2 14.8±0.6		15.3±0.6	1.39	−0.30	G&L
WD1031−114	52087.4720 52089.4805	34.7±0.6 36.7±0.7		35.7±0.6	1.35	−0.61	
WD1031+063	52009.7294 52663.7166	46.9±2.1 49.1±3.3		47.5±1.9	0.17	−0.17	
WD1036+085	52009.7412 52656.7444	17.1±8.6 19.2±2.0		19.1±2.1	0.03	−0.07	
HS1043+0258	52663.8213 52684.7354	20.3±2.0 19.7±1.5		20.0±1.3	0.03	−0.06	
WD1049−158	52387.6333 52616.8086	69.6±1.1 71.1±1.1		70.3±0.9	0.42	−0.29	
WD1053−550	52044.5187 52069.5214	19.4±0.9 19.2±0.8		19.3±0.8	0.01	−0.04	
WD1053−290	51657.6374 51681.5652	19.7±1.1 15.8±2.2		18.8±1.1	1.24	−0.57	polyn., G&L, v_{rot}
WD1053−092	51703.4915 51706.4974	19.0±2.9 24.5±3.1		21.6±2.1	0.95	−0.48	
HS1053+0844	52322.7977 52327.7283	23.8±3.9 27.2±1.9		26.4±1.8	0.33	−0.25	
WD1056−384	52044.5273 52069.5281	41.8±1.2 41.7±1.3		41.7±1.0	0.00	−0.02	
WD1058−129	51681.6696 51683.5080 51920.8751 52087.5514 52387.7118	55.1±5.9 77.9±2.7 66.1±5.1 71.1±2.7 64.2±3.6		70.3±1.6	10.06	−1.40	
HS1102+0934	52330.7772 52336.7983 52657.7283	138.6±3.5 76.0±2.6 156.7±3.7		113.6±1.9	218.35	−47.41	DD
WD1102−183	51657.6487 51683.5160 52087.5433	62.1±1.2 59.4±0.9 58.7±1.1		59.9±0.7	2.19	−0.48	polyn., G&L
HS1102+0032	52393.7094 52657.7357	57.2±2.1 53.7±1.6		55.0±1.4	0.89	−0.46	
WD1105−048	52387.6951 52656.7676	47.4±0.5 48.4±0.5		47.9±0.6	0.46	−0.30	G&L, ¹⁷
HE1106−0942	51739.4668 51743.4954	129.7±2.4 128.3±3.3		129.2±2.0	0.07	−0.10	DAO, G&L
HS1115+0321	52393.7011	34.1±1.5		34.7±0.9	0.09	−0.12	

¹⁷ unusually bad model fit

Table B.1: RV measurements, continued.

object	HJD −2 400 000	RV km s ^{−1}	$\Delta\lambda$ Å	\overline{RV} km s ^{−1}	χ^2	log p	comments
	52656.7756	34.9±0.8					
WD1115+166	52330.6807 52336.8111	33.3±1.7 65.7±1.6	30.0 30.0	49.6±1.3	97.54	−22.28	DD
WD1116+026	52663.8385 52684.7530	46.1±1.5 47.4±1.4		46.8±1.1	0.18	−0.17	G&L
HE1117−0222	51656.5634 51681.5835	43.0±1.0 36.4±1.5		40.7±1.0	6.02	−1.85	
WD1121+216	52327.7376 52288.8680	61.5±0.5 62.1±0.5		61.8±0.6	0.16	−0.16	G&L
WD1122−324	51657.6597 51683.5262	2.9±1.2 2.8±1.4		2.9±1.0	0.00	−0.00	
WD1123+189	52330.6921 52336.8192	13.8±10.0 7.8±15.3	40.0 40.0	12.0±8.4	0.06	−0.10	G&L
HE1124+0144	51727.4800 51728.4838	72.5±1.2 72.2±1.3		72.3±1.0	0.01	−0.04	
WD1124−293	51657.6709 51681.5945	29.4±0.7 29.2±1.5	10.0/ 15.0 10.0/ 15.0	29.4±0.8	0.00	−0.02	polyn., G&L, +CaK
WD1124−018	52328.8413 52330.7891	−17.2±2.5 79.2±2.2		38.1±1.7	454.57	<−100	DD
WD1125−025	52657.7604 52658.7043	55.8±3.8 53.6±5.0	30.0 30.0	55.0±3.1	0.07	−0.10	
WD1125+175	52328.7660 52330.8128	14.9±14.5 5.0±7.2	40.0 40.0	7.0±6.5	0.22	−0.19	
WD1126−222	51657.6823 51683.5356	54.3±2.9 49.0±4.7		52.8±2.5	0.52	−0.33	polyn., G&L, v_{rot}
WD1129+071	52657.8575 52663.8644	12.7±1.0 10.2±1.4		11.7±1.0	1.02	−0.50	
WD1129+155	52322.8171 52327.7452	36.3±1.6 39.0±1.4		37.8±1.2	0.77	−0.42	G&L
WD1130−125	51681.6895 51683.5543	51.2±3.2 61.4±1.2		59.9±1.3	4.81	−1.55	G&L
HS1136+1359	52393.6906 52657.7707	13.0±6.3 18.0±7.6		15.0±4.9	0.15	−0.15	
HS1136+0326	52657.7808 52658.7136	22.6±2.6 29.4±6.1		23.7±2.5	0.62	−0.36	
WD1141+077	51920.8833 53013.8200	38.9±2.1 29.0±3.3	30.0 30.0	35.8±1.8	3.55	−1.23	G&L
WD1144−246	51656.7204 51681.6283	−4.3±2.5 −9.1±3.2		−6.1±2.0	0.77	−0.42	
HS1144+1517	52328.7957 52330.8408	32.7±1.8 35.5±3.0		33.5±1.6	0.36	−0.26	
WD1145+187	52322.8263 52327.7537	40.0±1.4 42.0±1.3		41.1±1.1	0.56	−0.34	
WD1147+255	52657.7908 52663.8467	59.4±3.8 63.7±3.0		62.0±2.4	0.45	−0.30	G&L
WD1149+057	51924.8597 51946.6901	15.9±18.0 2.1±2.3		2.3±2.4	0.34	−0.25	G&L, ¹⁸
WD1150−153	51657.6935 51683.5645	25.3±0.9 20.8±0.9	10.0/ 15.0 10.0/ 15.0	23.0±0.8	4.75	−1.53	G&L, +CaK
HE1152−1244	51656.5947 51683.5778	31.5±1.1 30.1±1.1		30.8±0.9	0.35	−0.25	
WD1152−287	51736.5345 51736.5425 51740.4619	113.0±11.0 87.4±3.5 92.4±2.6	30.0	91.4±2.1	3.08	−0.67	
HS1153+1416	52657.7997 52684.7633	10.9±4.5 9.4±2.3		9.7±2.1	0.05	−0.08	
WD1155−243	51740.4953	44.3±1.5		45.4±1.1	0.49	−0.32	

¹⁸ spectrum 2001−02−04T06:25:52 not fitted, poor quality

Table B.1: RV measurements, continued.

object	HJD −2 400 000	RV km s ^{−1}	$\Delta\lambda$ Å	\overline{RV} km s ^{−1}	χ^2	log p	comments
	51743.5091	46.3±1.3					
WD1159−098	51728.5035 51731.4596	72.5±1.1 74.6±1.0		73.7±0.9	0.86	−0.45	G&L
WD1201−001	51742.5076 51739.4982	55.5±1.4 58.4±2.0		56.5±1.2	0.72	−0.40	
WD1201−049	52322.8366 52327.7629	31.2±13.7 5.4±14.1	40.0 40.0	18.6±9.8	1.01	−0.50	G&L
WD1202−232	51657.7037 51681.6363	23.1±0.4 23.8±0.7	10.0/ 15.0 10.0/ 15.0	23.3±0.6	0.19	−0.18	polyn., G&L, v_{rot} , +CaK
WD1204−322	51657.7234 51681.6440 53013.8274	13.6±1.5 16.7±2.4 14.8±1.8		14.6±1.1	0.64	−0.14	
WD1204−136	51657.7127 51681.6534 53013.8387	37.3±1.4 37.4±3.2 37.7±1.3		37.5±1.0	0.02	−0.00	polyn., G&L, v_{rot}
HS1204+0159	52328.8176 52329.7974	21.0±3.0 31.8±4.2		24.6±2.5	2.49	−0.94	
WD1207−157	51740.5046 51743.5349	6.4±1.8 7.4±2.6		6.7±1.6	0.06	−0.09	
WD1210+140	52657.8068 52658.7568	67.8±2.5 −62.9±2.6		6.5±1.9	726.43	<−100	DD G&L
WD1214+032	52657.7496	36.4±1.3		36.4±1.4	0.00	0.00	polyn., G&L, v_{rot}
HE1215+0227	51738.4628 51741.4753	29.4±13.9 33.6±7.1	40.0 40.0	32.8±6.4	0.04	−0.08	
WD1216+036	52069.5569 52080.5550	36.7±1.3 33.5±1.7		35.4±1.1	1.16	−0.55	
WD1218−198	51684.6079 51685.6803	−0.2±13.8 −1.6±12.2	40.0 40.0	−1.0±9.2	0.00	−0.02	
WD1220−292	51684.5611 51685.6900	18.6±0.8 22.0±1.8		19.3±0.9	1.46	−0.65	
HE1225+0038	51656.6225 51681.6629 51730.4803	11.3±0.7 10.4±1.4 11.5±1.0	10.0/ 15.0 10.0/ 15.0 10.0/ 15.0	11.2±0.7	0.20	−0.04	polyn., G&L, +CaK
WD1229−012	51684.5779 51686.5580	17.6±0.8 16.9±0.7		17.2±0.7	0.12	−0.14	G&L
WD1230−308	51684.5871 51686.5948	58.4±3.4 46.8±6.9		56.1±3.1	1.34	−0.61	
WD1231−141	51684.5981 51686.6044	6.6±1.4 13.0±1.3		10.1±1.1	5.19	−1.64	
HE1233−0519	51737.4654 51741.4860	62.3±8.6 44.7±5.2	40.0 40.0	49.5±4.5	1.80	−0.74	G&L, ¹⁹
WD1233−164	52387.4971 52657.8130 52658.7388	65.4±4.7 62.0±2.4 59.1±2.2		61.0±1.6	1.02	−0.22	
WD1236−495	52044.5600 52068.5906	74.4±1.9 72.1±1.5		73.0±1.3	0.43	−0.29	polyn., G&L
WD1237−028	52080.4824 52117.5042	57.8±3.1 63.3±1.9		61.7±1.7	1.26	−0.58	polyn., G&L
WD1241+235	52322.8816 52326.8787	8.9±3.0 8.7±2.2		8.7±1.8	0.00	−0.01	
WD1241−010	51684.6160 51686.5644	0.5±0.6 −5.4±0.6		−2.4±0.7	11.94	−3.26	
HS1243+0132	52393.7289 52656.8442	49.0±3.7 43.5±3.7		46.2±2.7	0.62	−0.36	
WD1244−125	51687.6284 51730.4725	29.2±1.1 26.4±1.2		27.9±0.9	1.33	−0.60	polyn.
HE1247−1130	52387.5492	18.3±4.2		18.4±3.5	0.00	−0.02	

¹⁹ magnetic

Table B.1: RV measurements, continued.

object	HJD −2 400 000	RV km s ^{−1}	$\Delta\lambda$ Å	\overline{RV} km s ^{−1}	χ^2	$\log p$	comments
	52393.7210	18.8±5.9					
EC12489−2750	51738.5636 51741.4973	39.0±3.4 16.3±7.4	40.0 40.0	35.0±3.1	4.47	−1.46	G&L
HS1249+0426	52080.5201 52113.5070	22.8±3.3 32.8±5.1		25.7±2.8	1.55	−0.67	polyn., G&L
WD1249+160	52326.8886 52328.7291	11.3±1.3 10.6±1.0		10.9±0.9	0.09	−0.11	
WD1249+182	52328.8518 52329.8201	−2.4±1.4 −4.4±1.2		−3.5±1.0	0.53	−0.33	polyn.
HE1252−0202	51738.5729 51741.5065	23.4±1.9 25.8±2.4		24.4±1.6	0.34	−0.25	
WD1254+223	52328.8609 52329.8809	8.1±3.1 8.7±3.9	40.0 40.0	8.3±2.5	0.01	−0.04	G&L
WD1257+047	51684.6222 51686.5802	43.5±1.5 40.2±1.4		41.8±1.1	1.20	−0.56	
WD1257+032	51939.8754 51942.8896	22.3±1.3 25.4±0.9		24.2±0.9	1.67	−0.71	²⁰
WD1257+037	51683.6735 51686.6252	101.7±5.7 99.2±6.1		100.6±4.2	0.05	−0.08	polyn., G&L, v_{rot}
HE1258+0123	51703.5253 51727.6046	41.1±3.5 40.3±3.6		40.7±2.6	0.01	−0.04	
WD1300−098	52080.5322 52136.5167	39.3±5.6 27.0±11.3		36.8±5.1	0.55	−0.34	G&L, ²¹
HS1305+0029	52080.5679 52656.8630	37.6±2.3 36.7±1.3		36.9±1.3	0.07	−0.10	
WD1305−017	52658.7638 52684.7734 52684.8071	−4.1±55.4 30.9±29.7 6.5±20.8	40.0 40.0 40.0	12.9±16.3	0.32	−0.07	DAO
HE1307−0059	51739.5103 51742.5189	50.0±2.0 52.6±1.9		51.4±1.5	0.49	−0.32	
HS1308+1646	52658.8029 52684.7878	48.0±3.7 44.5±3.6		46.2±2.6	0.27	−0.22	G&L, v_{rot}
WD1308−301	51687.6460 51703.5561	66.9±0.5 65.8±0.6		66.4±0.6	0.52	−0.33	G&L
HE1310−0337	51736.6041 51740.5418	55.6±7.4 38.0±5.4	30.0	44.1±4.4	2.12	−0.84	
WD1310−305	52378.7125 52659.7641 52658.7452	34.0±1.0 35.2±1.1 36.9±1.5		35.1±0.8	1.18	−0.26	G&L
EC13123−2523	51656.6350 51659.7365	30.6±1.3 23.1±2.7	30.0 30.0	29.0±1.3	3.33	−1.17	G&L
WD1314−153	52387.5661 52659.7707 52658.7707	108.8±1.2 107.4±1.1 105.3±1.2		107.2±0.8	1.99	−0.43	
WD1314−067	51947.7127 51948.8802	26.6±2.9 30.4±2.0		29.2±1.7	0.64	−0.37	
HE1315−1105	51657.5720 51683.6385	31.9±1.2 31.4±1.2	10.0/ 15.0 10.0/ 15.0	31.7±1.0	0.04	−0.08	polyn., G&L, +CaK
WD1323−514	52044.5684 52068.5973	−2.5±1.0 −3.8±0.8		−3.3±0.8	0.39	−0.27	
HE1325−0854	51684.5305 51686.5484	0.3±0.7 1.7±1.1		0.8±0.8	0.45	−0.30	
HE1326−0041	51738.5839 51741.5177	25.9±2.3 32.2±2.2		29.1±1.7	2.15	−0.85	
WD1326−236	51739.5221	8.0±1.7		6.6±1.0	0.43	−0.29	polyn.

²⁰ H α core of 2001/01/30 spectrum somewhat corrupted²¹ possibly magnetic

Table B.1: RV measurements, continued.

object	HJD −2 400 000	RV km s ^{−1}	$\Delta\lambda$ Å	\overline{RV} km s ^{−1}	χ^2	$\log p$	comments
	51742.5301	6.1±0.9					
WD1327−083	52382.7000 52684.7967 52658.7768	40.0±0.3 40.8±0.3 40.3±0.4		40.4±0.4	0.29	−0.06	G&L
HE1328−0535	51738.5953 51741.5280	30.6±13.6 −24.4±19.0	40.0 40.0	12.0±11.0	3.25	−1.15	
WD1328−152	51755.5256 52087.5228	−1.8±2.3 7.9±3.3	30.0 30.0	1.5±1.9	3.31	−1.16	G&L
WD1330+036	51684.6300 51687.5609	18.9±1.0 24.3±1.1		21.4±0.9	5.37	−1.69	
WD1332−229	51684.6404 51686.6366	13.4±1.9 19.4±1.8		16.5±1.4	2.71	−1.00	
WD1334+039	51755.5175 52136.5070	204.3±17.1 176.2±10.0		183.4±8.6	1.18	−0.56	G&L, ²²
HS1334+0701	52078.5495 52387.7572	−36.1±2.0 −59.4±2.7		−44.8±1.7	26.19	−6.51	DD polyn.
WD1334−160	51703.5671 51706.5492	52.3±1.3 51.7±0.9		51.9±0.9	0.08	−0.11	
WD1334−678	51755.5377 52044.5783	64.7±0.9 67.9±1.7		65.5±0.9	1.34	−0.61	G&L
HE1335−0332	51740.5520 51743.5467	49.8±5.3 61.5±4.4		56.7±3.4	1.67	−0.71	
HS1338+0807	52080.5960 52140.4947	70.5±5.0 72.2±2.8		71.8±2.5	0.05	−0.08	
HE1340−0530	51741.5685 51743.5565	19.9±6.7 34.5±9.6	40.0 40.0	24.7±5.5	0.90	−0.46	
WD1342−237	51739.5323 51742.5398	54.4±2.1 43.9±2.6		50.2±1.7	5.41	−1.70	polyn., G&L
WD1344+106	51755.5603 52066.6052	−11.6±0.7 −9.2±0.7		−10.4±0.7	1.92	−0.78	polyn., G&L
WD1348−273	52387.5731 52659.8176 52658.7926	61.4±2.0 53.3±2.3 60.8±4.0		58.2±1.5	3.86	−0.84	G&L
WD1349+144	51947.8050 51948.8908	29.2±2.8 −43.4±2.0		−18.3±1.7	239.52	−53.30	DD SB2
WD1350−090	51739.5514 51742.5478	53.4±1.3 55.1±1.3		54.3±1.0	0.43	−0.29	polyn., G&L, ²³
WD1356−233	51703.5780 51706.5594	−22.8±1.0 −19.2±1.0		−21.0±0.8	2.61	−0.97	polyn., G&L
WD1401−147	51739.5432 51742.5626	19.3±2.2 9.5±2.3		14.6±1.7	5.06	−1.61	polyn., G&L
WD1403−077	51947.7238 51950.8265	45.8±20.3 23.7±13.3	40.0 40.0	30.4±11.2	0.48	−0.31	
WD1410+168	52387.7646 52770.5395	2.7±2.2 4.1±1.9		3.6±1.5	0.12	−0.14	
HS1410+0809	52387.6042	66.7±4.0		66.7±4.1	0.00	0.00	
WD1411+135	52080.6076 52140.5131	42.4±3.8 48.3±2.4		46.6±2.1	1.00	−0.50	
WD1412−109	52137.5668 52140.5473	20.1±2.3 19.5±2.9		19.8±1.9	0.01	−0.04	
HE1413+0021	51738.6274 51741.5480	31.6±1.6 32.7±1.6		32.1±1.2	0.12	−0.14	
HE1414−0848	51684.6867 51687.6106 52080.6207	−106.3±2.0 128.9±3.1 135.4±3.0		53.2±1.2	4901.98	<−100	DD SB2, polyn., G&L

²² fit without model spectrum²³ magnetic

Table B.1: RV measurements, continued.

object	HJD −2 400 000	RV km s ^{−1}	$\Delta\lambda$ Å	\overline{RV} km s ^{−1}	χ^2	$\log p$	comments
	52137.5343	128.0±1.9					
WD1418−088	51739.5605 51742.5722	−37.1±1.5 −30.9±1.6		−34.1±1.2	4.09	−1.36	G&L, v_{rot}
WD1420−244	51684.6506 51687.5902	25.0±2.7 21.2±2.2		22.7±1.8	0.67	−0.38	
WD1422+095	51739.5691 51742.5541	−0.4±1.0 −0.6±0.9		−0.5±0.8	0.01	−0.03	polyn., G&L
WD1426−276	51730.6705 51731.6164	73.2±1.3 76.2±1.3		74.7±1.0	1.27	−0.58	
HE1429−0343	51739.5781 51742.5825	59.2±3.0 54.3±5.4		58.0±2.7	0.35	−0.26	polyn., G&L
HS1430+1339	52143.5108 52140.5360	23.3±2.3 13.9±2.5		18.9±1.8	4.14	−1.38	polyn., G&L
WD1425−811	52386.6998 52720.8732	30.8±1.1 34.0±0.7		32.8±0.8	2.23	−0.87	polyn., G&L
WD1431+153	52136.5291 52142.4997	11.9±2.0 10.2±1.7		10.9±1.4	0.21	−0.19	polyn.
HS1432+1441	52142.5121 52137.5026	74.7±1.3 71.8±1.2		73.2±1.0	1.23	−0.57	
WD1434−223	51684.6615	−73.3±4.5		−73.3±4.6	0.00	0.00	
HE1441−0047	51738.6668 51741.5595	27.1±5.5 18.4±4.9		22.3±3.7	0.80	−0.43	G&L, v_{rot}
HS1447+0454	52078.5930 52137.5456	−1.6±0.7 −3.9±0.8		−2.6±0.7	1.48	−0.65	polyn., G&L
WD1448+077	51755.5806 52078.5403	−107.2±0.9 −106.1±1.2		−106.8±0.8	0.27	−0.22	
WD1449+168	52393.7762 52387.7490	54.7±3.1 53.6±1.6		53.9±1.5	0.06	−0.09	
WD1451+006	51684.6722 51687.6004	1.8±1.6 4.3±1.5		3.2±1.2	0.65	−0.38	
WD1457−086	51738.6775 51741.5907	22.3±2.1 19.4±1.5	10.0/ 15.0 10.0/ 15.0	20.4±1.3	0.62	−0.37	G&L, +CaK
WD1500−170	51703.6251 51706.5792	−8.1±2.9 −8.8±2.6	30.0 30.0	−8.5±2.0	0.02	−0.05	
WD1501+032	51947.8351 51950.8464	−17.2±1.1 −15.9±0.9		−16.5±0.8	0.32	−0.24	
WD1503−093	51696.7399 51701.7063	1.0±1.7 −1.1±1.3		−0.3±1.1	0.47	−0.31	G&L
WD1507+220	52387.7919 52771.5979 52799.5451 53065.8615	−51.4±1.1 −40.9±4.5 −52.1±1.7 −53.0±0.9		−52.0±0.7	4.21	−0.62	
WD1507+021	52443.5669	34.9±2.4		34.9±2.5	0.00	0.00	
WD1507−105	51696.7505 51701.7202	−17.9±4.4 −15.9±0.9		−16.0±1.1	0.12	−0.14	G&L
HE1511−0448	51696.7628 51701.7314 51701.7425 52108.5059 52078.6243	−32.9±18.1 −71.3±2.2 −73.5±4.0 −105.1±2.2 −66.7±3.3	30.0 30.0 30.0 30.0 30.0	−82.6±1.4	89.86	−17.85	DD G&L
WD1511+009	51947.8452 51950.8559	13.2±3.5 18.2±3.6		15.6±2.5	0.56	−0.34	
WD1515−164	51703.6359 51706.5904	46.0±1.1 46.4±1.4		46.2±1.0	0.02	−0.06	
HS1517+0814	52080.6468 52116.4862	46.5±2.2 44.7±1.4		45.2±1.3	0.25	−0.21	
HE1518−0344	51730.6513 51731.6442	27.2±3.8 18.7±5.7		24.6±3.2	0.87	−0.46	

Table B.1: RV measurements, continued.

object	HJD −2 400 000	RV km s ^{−1}	$\Delta\lambda$ Å	\overline{RV} km s ^{−1}	χ^2	$\log p$	comments
HE1518−0020	51739.6020 51743.6499	32.1±0.9 27.9±3.5		31.7±1.1	0.73	−0.40	polyn.
HE1522−0410	51738.6884 51743.6697 51755.6030	29.9±2.2 34.6±6.7 18.0±3.6		27.1±1.9	5.29	−1.15	polyn., G&L
HS1527+0614	52080.6602 52116.4978	67.7±1.6 61.4±1.2		63.7±1.1	4.81	−1.55	
WD1527+090	52112.5350 52141.5256	22.7±1.1 26.2±1.0		24.5±0.9	2.44	−0.93	
WD1524−749	51739.6435 51743.6871 51755.5938	204.1±1.5 216.4±12.6 205.8±1.7	30.0	204.9±1.2	0.77	−0.17	
WD1531+184	52443.5796	31.9±1.6		31.9±1.7	0.00	0.00	
WD1531−022	52112.5272 52137.5846	43.7±1.6 43.9±1.4		43.8±1.2	0.00	−0.02	polyn., G&L, ²⁴
WD1532+033	52089.5361 52116.5083	11.2±6.9 16.8±9.2	40.0 40.0	13.2±5.6	0.14	−0.15	
WD1537−152	51727.6270 51731.6538	−0.8±1.6 4.5±1.5		2.0±1.2	2.74	−1.01	
WD1539−035	52136.5635 52141.5355	45.6±1.3 46.1±1.3		45.8±1.0	0.04	−0.07	polyn., G&L
WD1543−366	51731.6836 51739.6611	75.0±6.0 95.5±4.9	40.0 40.0	87.2±3.8	4.03	−1.35	
WD1544−377	51739.6693 52771.7871	22.4±0.5 19.4±0.7		21.1±0.6	3.27	−1.15	G&L, v_{rot}
WD1547+057	52088.5733 52089.5602	48.6±2.8 46.4±2.8		47.5±2.0	0.17	−0.17	
WD1547+015	52116.5185 52089.5473	−76.1±25.0 −106.1±53.8	40.0 40.0	−81.4±22.7	0.15	−0.16	G&L
WD1548+149	51979.7720 52033.6489	18.5±1.7 18.7±1.4		18.6±1.2	0.00	−0.02	
WD1550+183	52387.8695 52862.5458	9.2±3.2 12.9±1.5		12.1±1.5	0.60	−0.36	
WD1555−089	51740.6666 51743.6785	69.6±1.0 71.5±2.7		69.9±1.1	0.24	−0.20	
WD1609+135	51701.7588 51705.7321	108.1±0.8 106.5±0.9		107.4±0.7	0.73	−0.41	polyn., G&L
WD1609+044	52089.5710 52117.5209	38.9±1.8 36.1±1.6		37.4±1.3	0.65	−0.38	
HS1609+1426	52088.5505 52088.5844 52136.5755	−18.3±1.6 −14.2±1.7 −14.8±2.3		−15.9±1.1	1.71	−0.37	
WD1614+136	52116.5931 52117.5316	1.6±0.8 1.3±0.9		1.5±0.8	0.03	−0.06	
WD1614+160	52443.6108 52862.5546	−23.1±0.9 −23.5±1.2		−23.3±0.9	0.02	−0.05	
HS1614+1136	52443.6006 52839.6581	18.1±1.6 17.5±2.4		17.9±1.4	0.02	−0.05	
WD1614−128	51701.7691 51703.6054	87.4±1.2 84.7±1.1		86.0±0.9	1.20	−0.56	
WD1615−154	51701.7757 51703.5985	9.7±1.2 8.0±1.6		9.0±1.1	0.34	−0.25	
HS1616+0247	52443.5912 52542.5008	10.4±1.7 10.8±1.8		10.6±1.3	0.01	−0.04	
WD1619+123	52490.6177 52839.6684	15.1±1.2 15.4±1.3		15.3±1.0	0.02	−0.05	
WD1620−391	52386.7099	43.7±0.4		44.0±0.6	0.28	−0.23	

²⁴ possibly composite

Table B.1: RV measurements, continued.

object	HJD −2 400 000	RV km s ^{−1}	$\Delta\lambda$ Å	\overline{RV} km s ^{−1}	χ^2	$\log p$	comments
	52771.8007	44.4±0.4					
WD1625+093	51705.7430 51730.6808	66.0±2.4 67.3±1.8		66.8±1.5	0.10	−0.13	polyn., G&L, v_{rot}
WD1636+057	51705.7553 51731.6634	78.2±1.5 78.3±1.0		78.3±1.0	0.00	−0.02	polyn., G&L
WD1640+113	52108.5450 52116.5359	15.5±2.0 13.6±1.3		14.2±1.2	0.31	−0.24	
HS1641+1124	52116.6050 52117.5424	33.4±4.4 33.1±2.7		33.1±2.4	0.00	−0.02	polyn., G&L
HS1646+1059	52117.5830 52137.5955	10.7±1.8 15.1±2.2		12.6±1.5	1.26	−0.58	
HS1648+1300	52116.5561 52117.5730	−26.3±1.3 −27.8±1.4		−27.0±1.1	0.31	−0.24	
WD1655+215	52521.5373 52541.4905	46.6±0.8 45.7±0.6		46.1±0.7	0.28	−0.23	polyn., G&L
HS1705+2228	52521.5239 52538.5146	−42.7±0.9 −44.4±1.2		−43.4±0.9	0.50	−0.32	
WD1716+020	52387.8828 52815.7186	−19.3±0.7 −18.3±0.7		−18.8±0.7	0.34	−0.25	G&L
WD1733−544	51730.7009 51731.6743	29.9±1.1 33.3±1.0		31.7±0.9	2.06	−0.82	polyn., G&L
WD1736+052	51688.9114 51696.8023 51730.6909	52.6±1.4 45.1±2.5 52.3±1.2		51.4±1.0	4.05	−0.88	polyn., G&L
WD1755+194	52443.6515 52536.5186 52720.8940	45.2±2.1 51.2±4.2 42.2±2.9		45.2±1.7	1.72	−0.37	
WD1802+213	52465.7191 52482.7154	51.8±3.1 60.0±3.0		56.1±2.2	2.02	−0.81	
WD1821−131	51696.8167 51699.7714	−7.3±2.6 −15.4±1.5		−13.1±1.4	3.84	−1.30	G&L, v_{rot}
WD1824+040	51681.7166 51682.8934 52033.8512 52078.7260 52116.5739 52117.5931 52139.5153	35.0±1.3 −17.1±0.6 −15.7±0.9 4.2±0.6 18.7±0.5 80.6±0.5 11.2±1.5		19.5±0.4	5002.02	<−100	DD polyn., G&L
WD1826−045	52387.8877	−2.0±0.8		−2.0±1.1	0.00	0.00	G&L
WD1827−106	52387.9019 52815.7261	−38.8±1.6 −37.9±2.1		−38.4±1.3	0.06	−0.09	
WD1834−781	51731.6991 51738.7184	93.0±0.9 91.5±1.0		92.3±0.8	0.48	−0.31	
WD1840+042	52387.8932 52815.7363	1.1±0.7 3.4±0.8		2.2±0.7	1.51	−0.66	polyn., G&L
WD1845+019	52033.8574 52065.8166	−30.7±2.3 −30.7±1.9		−30.7±1.5	0.00	−0.00	SB2, ²⁵
WD1844−223	51981.8792 52033.8447	14.8±2.5 5.0±3.5	30.0 30.0	11.4±2.1	2.85	−1.04	
WD1857+119	51681.7265 51690.8904 51682.9007	−26.0±3.1 −31.1±1.8 −23.3±2.4		−27.7±1.4	3.77	−0.82	polyn., G&L
WD1911+135	51681.7336 51682.9090	16.6±3.1 17.5±0.9		17.4±1.0	0.04	−0.07	
WD1914+094	51689.9170 51690.9000 52033.8651	4.4±4.0 8.8±16.1 11.1±12.4	30.0 30.0 30.0	3.5±2.9	0.49	−0.04	

²⁵ H α emission from M dwarf/BD (physical?) companion

Table B.1: RV measurements, continued.

object	HJD −2 400 000	RV km s ^{−1}	$\Delta\lambda$ Å	\overline{RV} km s ^{−1}	χ^2	$\log p$	comments
	52065.8244	1.0±4.5	30.0				
WD1914−598	52033.8749 52065.8342	69.3±1.2 70.8±1.1		70.1±0.9	0.34	−0.25	
WD1918+110	51687.9081 51688.8802	75.9±1.8 73.9±1.6		74.8±1.3	0.36	−0.26	
WD1919+145	52426.9175 52765.9026	49.0±0.5 50.0±0.4		49.5±0.6	0.39	−0.28	G&L
WD1932−136	51687.9186 51688.8904	1.6±1.2 2.2±2.1		1.8±1.2	0.03	−0.07	
WD1943+163	52465.7391 52482.7348	31.5±3.6 33.1±0.9		33.0±1.1	0.11	−0.13	
WD1948−389	52033.8900 52065.8605	15.5±14.8 −23.3±8.2	40.0 40.0	−14.2±7.2	3.08	−1.10	
WD1950−432	52033.8978 52065.8671	−32.0±14.6 −41.9±8.7	40.0 40.0	−39.3±7.5	0.20	−0.18	
WD1952−206	51731.7224 51738.7046	38.8±0.7 38.8±0.9		38.8±0.7	0.00	−0.01	
WD1952−584	52138.5001 52140.5756	−0.1±6.3 8.9±8.7	30.0 30.0	3.0±5.1	0.40	−0.28	
WD1953−011	51681.7530 51682.9210	51.9±3.2 53.5±1.4		53.2±1.4	0.11	−0.13	G&L, ²⁶
WD1953−715	52387.8272 52388.7837	24.9±1.1 25.0±1.3		24.9±1.0	0.01	−0.03	
WD1959+059	51705.8690 51731.7293	−9.9±5.5 −5.1±3.6		−6.5±3.0	0.30	−0.24	polyn., G&L
WD2004−605	51738.7355 51743.7136	19.5±5.2 −2.6±16.5	40.0 40.0	17.4±5.0	0.95	−0.48	
WD2007−219	51738.7112 51761.7859	−21.2±0.7 −19.1±1.0		−20.3±0.8	1.05	−0.51	polyn., G&L
WD2007−303	52387.8119 52765.9107	72.9±0.3 74.3±0.3		73.6±0.5	1.14	−0.54	G&L
WD2014−575	51738.7420 51743.7253	66.5±0.9 72.0±2.1		67.6±1.0	2.88	−1.05	
WD2018−233	52033.9041 52117.6127	1.2±1.7 1.5±1.1		1.4±1.1	0.02	−0.05	
WD2020−425	51738.7493 51761.7932	67.6±6.5 −146.6±2.2		−123.7±2.1	563.95	<−100	DD SB2
WD2021−128	52033.9322 52065.8521	43.7±2.7 47.1±1.8		46.0±1.6	0.58	−0.35	
WD2029+183	52388.9019 52491.7102	−149.7±1.3 −143.7±1.4		−146.9±1.1	4.51	−1.47	polyn., G&L
WD2032+188	52521.5515 52527.5155	−23.1±1.1 −26.7±2.1		−24.0±1.1	1.11	−0.54	²⁷
WD2039−202	52387.8173 52812.9050	−2.8±0.4 −1.9±0.3		−2.3±0.5	0.36	−0.26	G&L
WD2039−682	52387.8350 52414.9160	57.7±1.1 56.1±1.2		57.0±1.0	0.40	−0.28	polyn., G&L, v_{rot}
HS2046+0044	52521.6321 52521.6406 52538.5098	−5.9±8.4 5.8±4.6 30.1±4.8		14.4±3.1	11.70	−2.54	
WD2046−220	52033.9120 52117.6210	−15.1±1.6 −14.2±1.3		−14.6±1.1	0.09	−0.12	
WD2051+095	51705.8880 51731.7382	15.5±1.6 17.2±1.2		16.5±1.1	0.33	−0.25	
WD2051−208	52140.6206	162.0±4.4		161.3±2.9	0.03	−0.07	polyn., G&L, ²⁸

²⁶ possibly magnetic, variable line profile²⁷ one spectrum not fitted -- poor quality²⁸ magnetic

Table B.1: RV measurements, continued.

object	HJD −2 400 000	RV km s ^{−1}	$\Delta\lambda$ Å	\overline{RV} km s ^{−1}	χ^2	$\log p$	comments
	52142.5386	160.7±3.8					
HS2056+0721	52140.6095 52142.5612	42.7±2.8 39.1±2.3		40.6±1.8	0.52	−0.33	
WD2056+033	52142.5492 52140.6309	−5.0±14.5 −13.9±15.7	40.0 35.0/ 40.0	−9.1±10.7	0.10	−0.13	
HS2058+0823	52145.5785 52141.5514	−2.3±6.0 −0.2±4.9	30.0 30.0	−1.0±3.8	0.04	−0.08	
WD2058+181	52465.7932 52527.5379 52538.6254	−47.0±1.1 −44.6±14.7 −45.4±1.4	30.0	−46.4±1.0	0.41	−0.09	
HS2059+0208	52521.6507 52539.5339	3.8±3.2 10.2±2.8		7.4±2.2	1.26	−0.58	
WD2059+190	52539.5437 52540.5599	6.3±1.8 9.4±2.3		7.5±1.5	0.61	−0.36	G&L
HS2108+1734	52465.7845 52527.5498 52861.6698	45.7±3.7 16.0±14.6 45.8±3.5	30.0 30.0 30.0	44.9±2.5	2.36	−0.51	
WD2105−820	52423.8069 52772.8885	41.1±1.3 40.7±4.5		41.1±1.4	0.01	−0.03	G&L, v_{rot} , ²⁹
WD2115+010	52145.5885 52144.6099	14.5±1.7 17.5±1.6		16.1±1.3	0.81	−0.43	
WD2115−560	52387.8721 52772.9009	2.5±1.2 5.7±1.1		4.2±0.9	1.74	−0.73	polyn., G&L
WD2120+054	52539.5538 52540.5707	−8.2±7.7 −1.7±7.8	30.0 30.0	−4.9±5.5	0.21	−0.19	
WD2122−467	52423.8161 52479.7642 52482.7441 52531.5638	24.8±2.1 24.3±2.0 24.2±1.6 23.5±4.0		24.3±1.1	0.06	−0.00	
WD2124−224	51739.6787 51761.8000	27.3±5.5 40.8±4.2	40.0 40.0	35.8±3.4	2.22	−0.87	
HS2130+1215	52540.5904 52541.5500	6.3±6.2 −8.5±9.8	30.0 30.0	2.1±5.3	0.95	−0.48	
HS2132+0941	52145.6098 52141.5713	−2.9±1.1 −5.4±1.2		−4.1±0.9	0.98	−0.49	polyn.
HE2133−1332	52172.5668 52142.5815	7.6±0.9 10.7±0.8		9.3±0.7	2.53	−0.95	G&L
WD2134+218	52465.8060 52527.6108	26.3±0.8 28.4±1.2		27.0±0.8	0.79	−0.43	
WD2136+229	52465.8213 52535.5780	−48.4±0.9 −46.1±1.1		−47.4±0.9	1.01	−0.50	polyn., G&L
HE2135−4055	51681.9070 52772.9085	67.6±0.8 66.0±0.8		66.8±0.7	0.67	−0.39	polyn., G&L, ³⁰
WD2137−379	51685.9061 51686.9041	−7.9±2.7 −14.7±1.9		−12.4±1.6	2.33	−0.90	
HS2138+0910	52145.6206 52141.5817	−25.0±1.4 −23.6±1.1		−24.2±1.0	0.28	−0.22	polyn., G&L
WD2139+115	51701.8743 51704.9340	19.3±1.3 17.3±2.2		18.7±1.2	0.33	−0.25	
HE2140−1825	52078.8893 52141.5928	6.3±1.1 6.8±0.8		6.6±0.8	0.05	−0.09	
WD2146−433	52069.9243 52138.5643	28.4±9.6 25.5±4.0	30.0 30.0	25.9±3.7	0.05	−0.08	G&L
HS2148+1631	52540.6005 52541.5637	3.2±1.4 7.6±1.7		5.0±1.2	1.99	−0.80	
HE2148−3857	51685.9153	45.7±3.4		46.5±2.6	0.06	−0.09	

²⁹ possibly magnetic or rapidly rotating³⁰ bad model fit for temperature

Table B.1: RV measurements, continued.

object	HJD −2 400 000	RV km s ^{−1}	$\Delta\lambda$ Å	\overline{RV} km s ^{−1}	χ^2	$\log p$	comments
	51686.8938	47.4±3.9					
WD2149+021	52540.6630 52861.8031	28.3±0.4 28.1±0.3		28.2±0.5	0.02	−0.05	G&L
WD2150+021	52540.6126 52541.5843	57.7±17.1 51.6±14.6	40.0 40.0	54.2±11.1	0.04	−0.08	
WD2152−045	52172.5390 52540.6700 52813.9033	22.0±10.3 9.6±1.9 14.1±1.9	30.0	12.1±1.4	2.05	−0.45	
WD2151−307	51739.6851 51761.8089	50.0±1.7 46.4±3.3		49.1±1.6	0.49	−0.31	
WD2152−548	51739.6912 51743.7666 51761.8136	−25.9±4.7 −43.0±6.2 −14.9±7.7	40.0 40.0 40.0	−28.9±3.4	5.13	−1.11	
WD2153−419	51696.8595 51699.7474	19.6±14.3 7.1±10.3	40.0 40.0	11.3±8.3	0.30	−0.23	G&L
WD2154−061	52172.5490 52540.6858	51.0±8.8 38.7±13.2	40.0 40.0	47.2±7.3	0.35	−0.26	
HE2155−3150	52078.8999 52138.5872	33.6±2.1 31.1±1.5		32.0±1.3	0.47	−0.31	
WD2157+161	52540.6224 52541.6021 52870.7390	−6.0±1.6 −10.9±1.7 −10.5±1.5		−9.1±1.0	2.93	−0.64	
HE2159−1649	51885.5213 51891.5256 52141.6240	32.5±1.7 45.7±3.5 38.3±1.2		37.1±1.0	7.49	−1.63	
WD2159−414	51705.8995 51708.8509	−88.5±14.6 −68.5±6.8	40.0 40.0	−72.1±6.2	0.89	−0.46	
WD2200−136	51885.5317 52540.7062 52172.6033 52540.6967	159.7±1.5 1.0±1.7 127.6±5.3 8.3±2.4		75.4±1.1	2991.48	<−100	DD SB2
WD2159−754	51884.5341 52142.6261	141.8±1.0 141.0±0.8		141.3±0.8	0.16	−0.16	G&L
HE2203−0101	52540.6335 52141.6349	29.0±1.1 23.5±1.4		26.7±1.0	4.27	−1.41	
WD2204+070	51701.8636 51704.9233 52142.6409	37.2±1.8 40.3±2.6 43.5±2.8		39.5±1.4	1.98	−0.43	
WD2205−139	51885.5404 52540.7279 52172.6137 52541.6140	46.0±2.2 46.9±2.1 48.3±5.3 52.8±1.7		49.1±1.2	4.04	−0.59	
WD2207+142	51690.9132 51696.8388	24.9±1.5 29.6±2.0		26.7±1.3	1.78	−0.74	G&L
HE2209−1444	51885.5488 52172.6360	81.6±1.7 −23.4±5.8		72.0±1.8	171.53	−38.47	DD SB2, G&L
HS2210+2323	52541.6239 52542.5192	50.1±2.1 50.4±2.3		50.2±1.6	0.01	−0.03	
WD2211−495	51739.6977 51743.7728	25.8±0.5 26.9±1.4	30.0 30.0	26.0±0.7	0.22	−0.20	G&L
HS2216+1551	52542.5294 52543.6272	−57.9±3.6 71.9±2.8		23.5±2.3	450.49	−99.25	DD SB2
HE2218−2706	52162.5351 52146.6637	−37.9±1.5 −33.2±0.7		−34.4±0.8	3.62	−1.24	
HE2220−0633	52541.6768 52144.6289	46.0±0.9 44.6±1.9		45.7±1.0	0.24	−0.21	
HS2220+2146B	52542.5809 52543.6348	37.7±2.3 37.6±2.3		37.6±1.7	0.00	−0.01	

Table B.1: RV measurements, continued.

object	HJD −2 400 000	RV km s ^{−1}	$\Delta\lambda$ Å	\overline{RV} km s ^{−1}	χ^2	$\log p$	comments
HS2220+2146A	52542.5753 52543.6397	25.9±3.4 30.0±2.8		28.3±2.2	0.51	−0.32	
WD2220+133	51884.5480 52172.6482 52883.7377	30.8±4.5 40.0±19.3 30.2±2.8		30.5±2.4	0.15	−0.03	
HE2221−1630	52434.9024 52144.6391	44.7±1.8 46.8±1.8		45.8±1.3	0.35	−0.25	polyn., G&L
HS2225+2158	52542.6019 52543.6470	17.4±2.3 23.9±2.3		20.7±1.7	2.16	−0.85	
WD2226+061	51696.8863 51701.8340	35.3±3.1 36.3±1.0		36.2±1.1	0.05	−0.09	
WD2226−449	52146.6723 52144.6859 52423.9030	55.8±0.5 55.6±0.5 56.3±0.5		55.9±0.5	0.23	−0.05	G&L
HS2229+2335	52542.6112 52543.6562	−14.6±1.5 −9.4±1.4		−11.9±1.1	3.12	−1.11	
HE2230−1230	52079.9102 52144.6621	13.3±1.8 15.5±2.0		14.3±1.4	0.35	−0.26	
HE2231−2647	52162.5437 52163.6549 52396.9065	−17.0±1.6 −17.7±2.1 −15.8±1.5		−16.6±1.1	0.30	−0.06	
HS2233+0008	52542.6199 52543.6649	41.7±0.9 42.5±1.0		42.1±0.8	0.13	−0.15	
WD2235+082	51884.5591 52153.5777 52153.5896 52172.6689	39.1±4.7 26.0±5.0 23.2±4.0 21.9±5.9	40.0 40.0 40.0 40.0	27.7±2.4	4.74	−0.72	G&L
HE2238−0433	52172.7058 52542.6322 52804.9072	62.5±14.4 43.4±7.1 44.8±4.8		45.7±3.9	0.87	−0.19	
HS2240+1234B	52541.7294 52542.6506	37.0±1.5 37.6±1.2		37.4±1.0	0.04	−0.08	
HS2240+1234A	52541.7164 52542.6596	40.1±1.7 36.6±2.3		38.8±1.5	0.80	−0.43	
WD2240−045	51696.8981 51701.8527	−70.6±5.3 −80.3±5.7	40.0 40.0	−75.1±3.9	0.90	−0.46	G&L
WD2240−017	51705.9082 51736.6808 51736.6885 52856.7489	32.1±1.6 28.6±4.8 31.7±7.2 28.7±3.6		31.2±1.5	0.59	−0.05	
WD2241−325	52437.9168 52479.7742	2.3±4.7 0.7±6.1	30.0 30.0	1.7±3.8	0.03	−0.06	
HS2244+2103	52543.6836 52544.5849	28.8±3.1 28.4±2.6		28.6±2.1	0.00	−0.02	
HS2244+0305	52541.7407 52542.6710	23.6±24.9 −101.4±27.9	40.0 40.0	−31.7±18.6	6.54	−1.98	G&L
HE2246−0658	52172.7133 52541.7486 52803.9317	67.3±13.1 48.4±3.1 59.7±13.4		49.9±3.0	1.48	−0.32	
WD2248−504	52423.9109 52416.9152	12.4±2.2 20.3±3.7		14.5±1.9	1.89	−0.77	
HE2251−6218	52153.5505 52154.5156	23.0±1.8 26.0±2.0		24.3±1.4	0.62	−0.37	
WD2253−081	51737.7520 51742.7655 52823.9128	1.8±1.6 20.1±7.3 −0.7±2.0		1.4±1.3	4.40	−0.95	polyn., G&L
WD2253+054	51761.8331 51762.6777	35.1±2.9 42.5±8.2		36.4±2.0	1.70	−0.20	polyn., G&L, v_{rot}

Table B.1: RV measurements, continued.

object	HJD −2 400 000	RV km s ^{−1}	$\Delta\lambda$ Å	\overline{RV} km s ^{−1}	χ^2	$\log p$	comments
	52856.7626	40.3±3.6					
	52862.7332	31.9±4.3					
WD2254+126	51705.9157	22.2±2.3		23.0±1.3	0.13	−0.03	G&L
	51737.7311	23.0±2.1					
	51740.7086	23.8±2.2					
HS2259+1419	52543.6936	−28.2±1.1		−28.0±0.9	0.03	−0.07	G&L
	52542.6901	−27.8±1.2					
WD2303+017	52172.7344	13.5±16.8	40.0	41.6±3.0	3.30	−0.46	
	52531.5554	38.2±9.4	40.0				
	52856.7721	41.2±3.3	40.0				
	52862.7228	57.2±9.4	40.0				
WD2303+242	52542.6998	13.1±1.8		10.6±1.4	1.91	−0.78	G&L
	52543.7029	8.2±1.8					
WD2306+130	52172.7456	33.4±1.2		33.7±0.8	0.05	−0.08	G&L
	52542.7097	33.9±0.8					
WD2306+124	51762.6499	36.4±2.6		39.1±1.3	0.78	−0.42	
	51802.5972	39.9±1.3					
WD2308+050	52542.7299	15.9±9.1	30.0	26.6±3.7	0.97	−0.49	
	52543.7333	28.7±4.0	30.0				
WD2309+105	51762.6581	−16.9±7.6	40.0	−16.8±2.4	0.00	−0.00	G&L
	51802.6075	−16.8±2.4	40.0				
WD2311−260	51708.8620	17.1±21.1	40.0	47.2±5.5	1.28	−0.59	G&L
	51737.7421	49.4±5.6	40.0				
WD2312−356	52154.5539	17.5±1.8		20.5±0.6	1.99	−0.13	
	52163.6750	19.5±1.7					
	52531.5852	21.2±0.8					
	52165.5311	20.6±0.9					
	52172.7562	21.2±1.1					
WD2314+064	52543.7427	27.5±1.2		27.2±1.2	0.10	−0.13	
	52544.6053	26.4±2.1					
HE2315−0511	51736.6975	72.3±32.2	30.0	27.2±5.6	4.85	−1.05	
	51736.7055	49.9±11.1	30.0				
	51742.7954	17.4±6.6	30.0				
WD2318+126	52543.7630	−11.9±1.6		−12.3±1.1	0.05	−0.09	G&L
	52544.6237	−12.6±1.4					
WD2318−226	51762.6681	48.1±15.3	30.0	43.2±3.7	0.06	−0.10	
	51802.6741	42.9±3.7	30.0				
WD2321−549	52212.7310	−13.0±33.5	40.0	7.9±6.1	0.24	−0.20	G&L
	52531.5735	8.6±6.2	40.0				
WD2322+206	52543.7737	5.9±1.1		5.0±0.9	0.52	−0.33	polyn., G&L
	52544.6333	4.2±1.0					
WD2322−181	51738.7684	24.7±1.5		24.6±1.1	0.00	−0.02	
	51741.7477	24.6±1.4					
WD2324+060	52543.8142	−6.3±0.9		−7.2±0.7	0.75	−0.41	
	52544.6724	−8.0±0.8					
WD2326+049	51762.6852	43.9±0.7	10.0/ 15.0	41.6±0.7	6.38	−1.94	polyn., G&L, +CaK
	51804.6758	39.5±0.6	10.0/ 15.0				
WD2328+107	52544.6821	44.8±1.2		44.3±0.9	0.17	−0.17	
	52547.6266	43.8±1.1					
WD2329−332	51740.7261	35.0±2.5		36.0±1.9	0.20	−0.18	
	51743.8226	37.2±2.7					
WD2330−212	52544.6920	−77.7±2.2		−55.7±1.7	122.70	−27.79	DD
	52547.5962	−27.3±2.5					
WD2331−475	51739.7628	23.4±2.6	40.0	21.9±1.9	0.36	−0.26	G&L
	51743.7885	20.4±2.6	40.0				
WD2333−165	51762.6926	69.4±0.5		69.0±0.6	0.24	−0.20	polyn.
	51804.6926	68.6±0.4					
WD2333−049	51762.7115	44.6±2.3		47.0±1.5	1.05	−0.52	polyn., G&L, v_{rot}

Table B.1: RV measurements, continued.

object	HJD −2 400 000	RV km s ^{−1}	$\Delta\lambda$ Å	\overline{RV} km s ^{−1}	χ^2	log p	comments
	51803.6089	48.6±1.8					
HE2334−1355	52544.7020	20.2±2.0		19.0±1.5	0.36	−0.26	
	52547.6063	17.9±2.1					
WD2336−187	51738.7794	11.6±3.1		−3.6±2.8	70.03	−16.23	DD
	51741.7681	−66.1±6.3					SB2, polyn., G&L
WD2336+063	52544.7122	38.9±0.8		39.0±0.8	0.01	−0.04	
	52547.6169	39.1±1.0					
MCT2343−1740	51802.6292	51.7±15.0		27.8±3.6	1.57	−0.68	
	51803.5741	26.4±3.6					
HE2345−4810	52162.6064	54.0±1.9		43.1±1.8	67.25	−15.62	DD
	52466.9007	10.0±3.5					
MCT2345−3940	51802.6167	1.6±2.3		4.6±1.4	1.48	−0.65	
	51803.5613	6.2±1.6					
WD2347+128	51802.6883	−2.2±2.4		0.7±1.6	1.33	−0.60	polyn., G&L
	51804.6838	2.8±2.0					
WD2347−192	51802.6409	32.7±4.2		31.1±2.7	0.14	−0.15	
	51761.8427	30.0±3.5					
HE2347−4608	52532.6073	48.2±1.2		48.7±1.0	0.17	−0.16	
	52542.8092	49.3±1.3					
WD2348−244	51762.7212	67.2±1.5		65.8±1.1	0.76	−0.42	polyn., G&L, v_{rot}
	51802.6514	64.6±1.4					
MCT2349−3627	51802.7047	23.1±36.0	40.0	16.9±18.6	0.02	−0.06	
	51804.6325	14.6±21.7	40.0				
WD2349−283	51762.7350	36.2±1.0		35.2±0.8	0.76	−0.42	
	51802.6635	34.3±0.9					
WD2350−248	51761.8516	62.0±2.6		62.7±2.1	0.09	−0.12	
	51803.5874	63.7±3.3					
WD2350−083	52530.8368	56.1±1.4		58.3±1.1	2.57	−0.96	
	52466.9202	60.7±1.5					
WD2351−368	51739.7706	−7.7±1.6		−7.0±1.3	0.24	−0.21	G&L, v_{rot}
	51743.7962	−6.1±1.8					
MCT2352−1249	51802.7167	−1.8±44.8	40.0	−2.1±14.3	0.11	−0.02	
	51804.6436	−18.5±40.4	40.0				
	52822.9232	0.6±16.3	40.0				
WD2353+026	52466.8883	2.2±3.2	40.0	0.3±2.8	0.77	−0.42	G&L
	52530.6840	−5.2±5.5	40.0				
WD2354−151	51761.8220	18.3±2.6	30.0	18.8±2.2	0.06	−0.09	
	51803.5982	19.8±3.8	30.0				
HE2356−4513	52163.6309	55.5±1.4		53.3±0.7	1.66	−0.19	
	52466.8676	52.8±1.2					
	52466.8740	51.6±3.7					
	52500.9107	52.6±0.9					

Appendix C: Fundamental parameters

Table C.2 lists the fundamental parameters surface temperature and gravity adopted for our targets. Most of these values are taken from Koester et al. (2009) who determined temperatures and gravities of sample stars by fitting the Balmer lines of the SPY spectra. The table lists effective temperatures and gravities, with the 3D atmosphere corrections of Tremblay et al. (2013a) for DAs with a convective envelope. White dwarf masses were estimated from interpolation in the white dwarf cooling tracks of Panei et al. (2007), Renedo et al. (2010) and Althaus et al. (2005).

Koester et al. (2009) did not derive parameters for some DAs of the sample for various reasons, including a few cases of objects overlooked. For some other cases we decided to replace the values as discussed below. Notes and references have been included in Column 5 of Table C.2 and explained in Table C.1, whenever values different from those given by Koester et al. (2009) were included.

Double-lined binaries: Light of both components is seen in the spectra of double-lined binaries. A deconvolution of both components was attempted using `FRITSB2` and the same DA model grid as used by Koester et al. (2009). An iterative procedure was carried out starting with a simple by-eye estimate of the RVs in the spectra, followed by a fit of temperatures and gravities of both components. These were then used for improved estimates of RVs from the cores of $H\alpha$ and $H\beta$ as described in 3.2. The latter two steps were repeated until the iteration came to a standstill. The relative contributions of both components were determined using mass-radius relations from the cooling tracks above. The fundamental parameters listed in Tables C.2 and B.1 correspond to the primary (i.e. the brighter component).

The fundamental parameters listed for the primaries are tentative and should be replaced by results from full orbital solutions once these are available. They were derived for the purpose of assessing the status of the primary as low-mass He core or C/O core white dwarf.

Magnetic white dwarfs: Magnetic white dwarfs included in this study have fields strong enough to induce a detectable Zeeman splitting in the cores of the Balmer lines, but the lines do not show distortion beyond that. A detailed analysis of the field structure was beyond the scope of this article and we adopted a crude approximation to derive fundamental parameters. Model spectra from standard model atmospheres were co-added after applying shifts. The π component was assumed unshifted and a symmetric shift was applied to the two σ components. Geometric effects were only taken into account by adjusting the relative strength of the π and σ components. This approach is oversimplistic and ignores subtle effects of radiation transfer and field geometry, but our main aim was to get still useful estimates of fundamental parameters, even if of somewhat limited accuracy.

Grids were constructed for a range of splits. For a given magnetic white dwarf best fit values of temperature and gravity were derived for each grid. Values corresponding to the Zeeman split yielding the smallest value of χ^2 were adopted. While we deem the accuracy of the fundamental parameters sufficient to assess the nature (high or low mass) of the white dwarfs, investigators with a specific interest in these stars are advised to carry out a more sophisticated analysis.

Table C.1: References and explanations for Table C.2

ambiguous	Koester et al. (2009) reported a cool and a hot solution. The solution yielding the smallest χ^2 is included.
BL02	Bergeron & Liebert (2002)
GBD12, phot	Giammichele et al. (2012), T_{eff} and $\log g$ derived from photometric spectral energy distribution and trigonometric parallax.
GBR11	Gianninas et al. (2011), fit of Balmer lines
KNV05	Koester et al. (2005a), helium-rich DABZ
KV12	Kawka & Vennes (2012), fit of Balmer lines
LBSS93	Liebert et al. (1993), binary of magnetic and non-magnetic WD
magnetic	magnetic DAs, Zeeman splitting of the line cores. See text for details on the fit procedure.
new	white dwarf not included in the Koester et al. (2009) analysis. Analysed using the same model grid.
new/NLTE	hot DAO white dwarfs, analysed using the grid of NLTE model atmospheres described in Napiwotzki (1999).
primary	Parameters of the primary from a simultaneous fit of primary and secondary. See text.
WB94	Wesemael et al. (1994), fit of primary and secondary parameters using lines and spectral energy distribution
HNLE97	Heber et al. (1997a): genuine DAB, helium line profile variations
K09	Koester et al. (2009): visual double
FK97	Finley & Koester (1997): visual double
J98	Jordan et al. (1998): visual double

Cool white dwarfs: It has been known for some time that the accuracy of surface gravity measurements from Balmer lines alone decreases considerably for white dwarfs at temperatures below ≈ 6500 K (see, e.g., Fig. 2 of Kawka & Vennes 2012). Higher accuracy can be achieved, if parallax measurements are available. We replaced spectroscopy-only values by the parallax based photometric values of Giammichele et al. (2012), if available. Spectroscopic-only fundamental parameters were not included when assessing the number of single and binary white dwarfs in the mass ranges in Table 3 and the discussion (Sect. 5). This is indicated by the lack of a mass entry in Table C.2. All white dwarfs are included in the numbers for the full sample.

Table C.2: Gaia DR2 IDs, effective temperatures, gravities and masses for the SPY DA white dwarfs.

object	Gaia DR2 ID	T_{eff} K	$\log g$ cm s^{-1}	M M_{\odot}	References/remarks
WD2359-434	4994877094997259264	8253	8.01	0.604	magnetic
WD2359-324	2313582750735435776	22478	7.74	0.514	
WD0000-186	2414099622710507904	15264	7.85	0.535	
HS0002+1635	2772855182928578560	25878	7.86	0.568	
WD0005-163	2416481783371550976	11860	7.60	0.435	ambiguous
WD0011+000	2545505281002947200	9423	7.77	0.492	
WD0013-241	2336189396997071616	18529	7.90	0.568	
WD0016-258	2323704339384503040	10874	7.80	0.507	
WD0016-220	2361264618662161920	13622	7.75	0.496	
WD0017+061	2747611250653031040	28149	7.75	0.526	
WD0018-339	2315346161227820032	20626	7.84	0.548	
WD0024-556	4920057871348614272	10112	8.46	0.876	
WD0027-636	4900807999725863296	58129	7.77	0.603	
WD0028-474	4978793541987799040	20453	7.83	0.54	primary
WD0029-181	2364272573237917952	13966	7.81	0.519	
HE0031-5525	4921390960477978112	11839	7.71	0.477	
MCT0031-3107	2317553529604662016	40698	7.78	0.568	
HE0032-2744	2343355051714253056	23947	7.81	0.543	
WD0032-317	2317319612801004416	36965	7.19	0.422	
WD0032-175	2364319061964016512	9602	7.82	0.509	
WD0032-177	2364311331022888704	17210	7.82	0.526	
WD0033+016	2544456862306151680	10642	8.55	0.936	
MCT0033-3440	5005361213245945856	15890	8.18	0.717	
WD0037-006	2542961560852591744	13922	7.78	0.505	primary
HE0043-0318	2529237113117694336	14086	7.73	0.49	
WD0047-524	4922382445088509312	18811	7.73	0.503	
HS0047+1903	2788992130973584640	17135	7.82	0.529	
WD0048-544	4921090656364298368	17870	7.98	0.605	
WD0048+202	2789398778477164672	20363	7.89	0.569	
HE0049-0940	2473843786029439104	13823	7.69	0.477	
WD0050-332	5006486048001153792	35570	7.87	0.596	
HS0051+1145	2774977549607430528	20963	7.93	0.589	magnetic
WD0052-147	2372473658671416960	25950	8.22	0.756	
WD0053-117	2472557872820632320	6543	6.97		
WD0058-044	2525337076653338240	17209	8.02	0.627	magnetic
WD0101+048	2552121179905893888	8399	7.77	0.488	
WD0102-185	2357946464368276224	21969	7.64	0.484	
WD0102-142	2468060664104501376	19945	7.86	0.553	
HE0103-3253	5027351170924256512	13698	7.82	0.519	
WD0103-278	5034051079388141696	14410	7.79	0.511	
MCT0105-1634	2359382697136585728	28212	7.83	0.563	
WD0106-358	5014009353235167744	29198	7.86	0.576	
HE0106-3253	5026963661794939520	17234	8.00	0.616	
WD0107-192	2354670057156360576	14304	7.79	0.51	
WD0108+143	2591091789004351104	9193	8.26	0.752	
WD0110-139	2456122476087944960	24692	7.99	0.627	
MCT0110-1617	2358739727648116608	34621	7.75	0.542	
MCT0111-3806	4988781711771040128	71306	7.19	0.497	
WD0112-195	2354521726165844096	36364	7.66	0.518	
WD0114-605	4716787269774839936	24692	7.75	0.521	
WD0114-034	2483669331171909120	19460	7.77	0.516	
WD0124-257	5037128131397095168	23042	7.79	0.53	
WD0126+101	2585189473147457408	8551	7.37	0.338	
WD0127-050	2480731779699826176	16718	7.78	0.514	
WD0128-387	5009694457291031168	13404	8.41	0.854	primary, WB94
WD0129-205	5043926824108837376	19950	7.88	0.566	
HS0129+1041	2585306399337120128	16738	7.92	0.573	
HS0130+0156	2558916466707621504	41083	7.74	0.556	
HE0130-2721	5035978214033613824	21880	7.90	0.578	

Table C.2: Gaia DR2 IDs, effective temperatures, gravities and masses, continued.

object	Gaia DR2 ID	T_{eff} K	$\log g$ cm s^{-1}	M M_{\odot}	References/remarks
HE0131+0149	2558736322894795648	15228	7.75	0.498	
WD0133-116	2457759374023232768	12556	7.79	0.506	
WD0135-052	2480523216087975040	6914	7.19		primary
MCT0136-2010	5139880551029408768	8893	8.43	0.857	primary
MCT0138-4014	4960499042889705344	21698	7.90	0.576	
WD0137-291	5023333658515040128	21550	7.75	0.515	
WD0138-236	5039292447021548416	36897	7.63	0.513	
WD0140-392	4962193390308361728	21811	7.92	0.586	
WD0143+216	98092934167683072	9195	8.07	0.638	
WD0145-221	5135466183642594304	11933	7.92	0.566	
WD0145-257	5037875455706805504	25915	7.86	0.568	
HS0145+1737	91690164426711040	18125	7.89	0.566	
HE0145-0610	2467788122659245696	8616	7.77	0.489	
HS0146+1847	95297185335797120	11500	(8.00)		KNV05, logg assumed
HE0150+0045	2510891108771852416	12993	7.68	0.471	
WD0151+017	2511623211717232640	12811	7.78	0.504	
HE0152-5009	4940662032058418944	13373	7.63	0.454	
WD0155+069	2567944320460595840	22007	7.67	0.492	
WD0158-227	5134814168951616000	67081	7.46	0.541	
HE0201-0513	2491046298280035584	24626	7.64	0.49	
HS0200+2449	105299786211260160	23281	7.86	0.563	
WD0203-138	5149462073310745344	48529	8.00	0.675	
WD0204-233	5122528470836031232	13425	7.74	0.491	
HE0204-3821	4964509614631078272	14038	7.79	0.512	
HE0204-4213	4957085334163504512	22575	7.90	0.58	
WD0204-306	5020119579868434944	5640	(8.00)		KV12, logg assumed
WD0205-365	4968128554074903808	61240	7.74	0.601	
WD0205-304	5020146620982523008	17209	7.76	0.508	
HE0205-2945	5020319141229055360	11769	7.54	0.413	primary
WD0208-263	5118133276183878400	33720	7.76	0.547	
HS0209+0832	2521867808229983744	37070	7.92	0.621	NEW, HNLE97
HE0210-2012	5125057897336633344	17612	7.80	0.521	
HE0211-2824	5116584064300345984	14469	7.95	0.585	
WD0212-231	5123291871208145792	26827	7.94	0.608	
HS0213+1145	72992389375581440	17518	7.79	0.517	
WD0216+143	75783121685634816	26637	7.79	0.54	
HE0219-4049	4951125156507440384	15373	7.89	0.558	
HE0221-2642	5118624311204821504	32008	7.72	0.525	
WD0220+222	99915890086770176	15630	7.89	0.558	
HE0221-0535	2488754366292015744	24747	7.95	0.609	
HE0222-2336	5120365044270095232	31816	7.87	0.588	
HE0222-2630	5118634309888681600	23198	7.91	0.586	
HS0223+1211	74336778563550464	14721	7.30	0.35	
HE0225-1912	5131327656235273088	20488	7.84	0.545	primary
HS0225+0010	2501224305619721984	13778	7.81	0.515	
WD0226-329	5063539946887524864	22294	7.88	0.567	
WD0227+050	2516322146457318144	19341	7.76	0.513	
WD0229-481	4939012317940174464	59082	7.71	0.587	
WD0230-144	5146358426863612160	5477	8.13	0.662	GBD12, phot
WD0231-054	2488960249844340352	17306	8.45	0.878	
HS0237+1034	24968088000745216	17481	8.10	0.67	primary
WD0239+109	25405350031335296	(6926)	(7.39)		magnetic
HS0241+1411	32880762085326336	13932	7.76	0.498	
WD0242-174	5132580858972702976	20663	7.85	0.553	
WD0243+155	33554517899463040	17611	7.96	0.596	
WD0243-026	2495751967528809216	6770	8.18	0.698	GBD12, phot
HE0245-0008	2498564582697028864	18813	7.98	0.608	
HE0246-5449	4740913887782857216	15949	7.83	0.529	
WD0250-026	5187346124402986752	15315	7.80	0.515	

Table C.2: Gaia DR2 IDs, effective temperatures, gravities and masses, continued.

object	Gaia DR2 ID	T_{eff} K	$\log g$ cm s^{-1}	M M_{\odot}	References/remarks
WD0250-007	2497895053130247040	7968	7.63	0.43	
WD0252-350	5049628376014475648	16934	7.37	0.379	
WD0255-705	4645960583300470656	10485	7.82	0.512	
HE0255-1100	5160899536860481664	20827	7.84	0.545	
HE0256-1802	5152564272353619072	26212	7.76	0.524	
HE0257-2104	5079634765595460736	17362	7.69	0.486	
WD0257+080	8578256576520320	6410	7.30		magnetic
HE0300-2313	5078074837769743744	22369	8.39	0.847	
WD0302+027	1068931460633216	35270	7.77	0.554	
HE0303-2041	5103714555575829888	9959	7.87	0.53	
HE0305-1145	5159714332045197568	26822	7.81	0.55	
WD0307+149	31047257726638592	21413	7.91	0.581	
HS0307+0746	13611477211053824	10084	7.81	0.507	
WD0310-688	4646535078125821568	16329	7.91	0.568	
HE0308-2305	5075443981321647744	23565	8.54	0.94	
WD0308+188	59077760488621184	18450	7.72	0.5	
HS0309+1001	15255418893384320	18786	7.72	0.5	
WD0315-332	5054287144220982144	49926	7.47	0.5	
HS0315+0858	14141304376849280	18783	7.87	0.557	
HE0315-0118	3262674487682440448	12720	7.74	0.491	primary
HE0317-2120	5100053078775660160	9638	7.83	0.514	
WD0317+196	59370127502651264	17735	7.78	0.514	
WD0318-021	3262366899304566272	15125	7.70	0.483	
WD0320-539	4734298439852277376	32588	7.77	0.546	
HE0320-1917	5104856776357892480	13248	7.17	0.311	
HE0324-2234	5098930339964725248	16905	7.84	0.539	
HE0324-0646	5168944835239726080	15740	7.87	0.546	
HE0324-1942	5101782335688104960	23811	8.27	0.78	primary
HE0325-4033	4849811172961336960	16737	7.70	0.486	
HS0325+2142	61497407625478272	14027	7.93	0.572	
WD0326-273	5060587895604134400	9158	7.44	0.364	
WD0328+008	3264857636738890624	34476	7.92	0.614	
HE0330-4736	4833967725801565696	13437	7.95	0.585	
HS0329+1121	13469296613857152	17376	7.86	0.545	
WD0330-009	3263351202729621376	34044	7.74	0.538	
HS0331+2240	67620897117741440	21452	7.78	0.523	
HE0333-2201	5088334621288740992	16046	8.19	0.722	
HE0336-0741	3243842361760113408	15854	7.77	0.507	
WD0336+040	3274761620869767168	8696	7.57	0.409	
HS0337+0939	12254267546754176	12843	7.88	0.547	ambiguous
HE0338-3025	5055975238166788352	9911	7.87	0.53	
WD0339-035	3249740657527506048	12758	7.86	0.535	ambiguous
WD0341+021	3270918350990573184	22153	7.27	0.378	
WD0343-007	3251501727261970432	62994	7.68	0.585	
WD0344+073	3277341526122556160	10453	7.50	0.389	
HS0344+0944	3302674308386137856	15321	8.23	0.741	
HE0344-1207	5114767980330242688	11497	7.91	0.559	
HS0345+1324	37976345646670464	25064	8.18	0.731	
WD0346-011	3251244858154433536	40455	9.31	1.293	
HS0346+0755	3277482882085624192	16796	7.72	0.494	
HE0348-4445	4835585377987834752	19951	8.07	0.658	
HE0348-2404	5083966055431334912	14735	7.94	0.582	
HE0349-2537	5083478078426926976	20974	7.91	0.578	
WD0352+049	3273625554777257472	37253	8.61	0.922	
WD0352+052	3273645105468368000	10095	7.71	0.47	
WD0352+018	3258317294901181440	22107	7.80	0.531	
WD0352+096	3302846072717868416	14465	8.18	0.709	
HE0358-5127	4828757999190736128	23376	7.93	0.593	
WD0357+081	3301319572621418368	5478	8.04	0.609	GBD12, phot

Table C.2: Gaia DR2 IDs, effective temperatures, gravities and masses, continued.

object	Gaia DR2 ID	T_{eff} K	$\log g$ cm s^{-1}	M M_{\odot}	References/remarks
HS0400+1451	39305036729495936	14623	8.25	0.754	
HS0401+1454	39124751182907520	12903	7.88	0.535	ambiguous
HE0403-4129	4842194473663089920	22702	7.94	0.597	
HE0404-1852	5095932968188685696	19218	7.67	0.483	
WD0406+169	45980377978968064	16049	8.24	0.748	
WD0407+179	46896958359881728	14421	7.77	0.504	
WD0408-041	3251748915515143296	15414	7.86	0.541	
HE0409-5154	4780544792270137088	26315	7.83	0.556	
HE0410-1137	3189613692364776576	12934	7.73	0.485	primary
WD0410+117	3304090857318319232	21074	7.84	0.549	
HS0412+0632	3297249936488848384	13694	7.78	0.507	
HE0414-4039	4841115341656167552	20941	7.93	0.592	
WD0416-550	4778802753534553472	30547	7.12	0.379	
HE0416-3852	4844370755067765504	19324	7.96	0.598	
HE0416-1034	3191249387709577088	24845	7.92	0.592	
HE0417-3033	4884691594508544128	19103	7.85	0.546	
HE0418-5326	4779427928974390272	27090	7.87	0.577	
HE0418-1021	3191269144559159936	23385	8.29	0.789	
WD0421+162	3313606340183243136	19616	8.03	0.634	
HE0423-2822	4892048018790150656	10966	7.85	0.525	
HS0424+0141	3279793505770723584	44174	7.68	0.541	
HE0425-2015	4899868157803497984	19801	8.12	0.683	
WD0425+168	3313714023603261568	24000	8.04	0.649	
HE0426-1011	3179499250541535744	18386	7.85	0.548	
WD0426+106	3305972018634634880	10009	8.13	0.674	
HE0426-0455	3202808828330265088	14129	7.99	0.604	
WD0431+126	3306722607119077120	21374	7.97	0.609	
HE0436-1633	3171373722173234048	14092	7.96	0.588	
WD0437+152	3309687027907272576	18711	7.25	0.356	
WD0440-038	3201709827802584576	68468	8.42	0.914	
WD0446-789	4622856957782901504	23627	7.69	0.501	
HE0452-3429	4873109308958466432	14825	7.81	0.519	
HE0452-3444	4873054711334208256	21206	7.84	0.548	
WD0453-295	4876689387538123008	16360	7.44	0.399	primary, WB94
HE0455-5315	4782942513595999872	24432	7.55	0.467	
WD0455-282	4880286371109059712	54386	7.68	0.567	
HE0456-2347	2960529070328892928	23645	7.79	0.534	
HS0503+0154	3229005792373924224	54563	7.54	0.526	
HE0507-1855	2975647836248304256	20421	8.27	0.775	
HS0507+0434B	3238868171156736768	11663	7.89	0.545	J98; WD0507+045A
HS0507+0434A	3238868098140387840	20838	7.90	0.574	J98; WD0507+045B
HE0508-2343	2959967254246803328	16811	7.74	0.5	
WD0509-007	3215427579684548864	31910	7.29	0.429	
WD0510-418	4812859061053900928	50490	7.68	0.557	
WD0511+079	3242153305741855744	6158	7.18		
HE0516-1804	2981590730954538112	13287	7.73	0.486	
WD0518-105	3014049448078210304	32008	8.82	1.099	
HE0532-5605	4766810380210581632	11381	8.23	0.737	
WD0548+000	3218753701142724992	44684	7.82	0.594	
WD0549+158	3348071631670500736	32959	7.73	0.531	
WD0556+172	3350123251647482624	18825	8.09	0.67	
WD0558+165	3348917053032143616	16807	8.18	0.717	
WD0603-483	5554202096021588992	34731	7.84	0.581	
WD0612+177	3370342445848382080	25624	7.81	0.548	
WD0621-376	5575007845317435648	57806	7.27	0.475	
WD0628-020	3117320802840630400	6443	7.20		
WD0630-050	3103530586268279936	42451	8.34	0.842	
WD0642-285	2918665577420228480	9104	7.54	0.397	
WD0646-253	2921786919133198848	27990	7.79	0.544	

Table C.2: Gaia DR2 IDs, effective temperatures, gravities and masses, continued.

object	Gaia DR2 ID	T_{eff} K	$\log g$ cm s^{-1}	M M_{\odot}	References/remarks
WD0659-063	3052844272764398208	6046	6.95		
WD0710+216	3367112974037883904	10167	7.73	0.479	
WD0715-703	5267418883330985856	44915	7.67	0.541	
WD0721-276	5612710511362093184	36520	7.70	0.53	
WD0732-427	5536077746353130240	14995	8.00	0.611	
WD0752-676	5273943488410008832	5735	8.23	0.726	GBD12, phot
WD0810-728	5220896587855584384	30598	7.84	0.573	
HS0820+2503	679177201586401280	33367	7.66	0.513	
WD0830-535	5321056462156468480	30050	7.76	0.537	
WD0838+035	3080056219172355840	38342	7.72	0.54	
WD0839-327	5639391810273308416	9174	7.56	0.405	
WD0839+231	665392383790872192	25852	7.64	0.493	
WD0852+192	660409908193185024	15130	7.85	0.536	
WD0858+160	610478649930041856	16064	7.77	0.51	
WD0859-039	5762406957886626816	23731	7.79	0.533	
WD0908+171	607984785759304192	17640	7.83	0.534	
WD0911-076	5744058376561655168	18175	7.85	0.547	
WD0916+064	585877867532382592	43048	7.37	0.482	
PG0922+162B	630770819920096768	25783	9.04	1.2	FK97
PG0922+162A	630770819920096640	23537	8.23	0.754	FK97
WD0922+183	632366829767058816	24532	8.16	0.717	
WD0928-713	5219215228420645248	8401	7.84	0.514	
HS0926+0828	588078329602228992	12250	7.83	0.519	ambiguous
HS0929+0839	588063421770438400	15707	7.77	0.509	
HS0931+0712	3852811476713249536	36719	7.16	0.412	
HS0933+0028	3840288524603932800	32219	8.10	0.698	
HS0937+0130	3846451454781376512	19717	8.31	0.8	
WD0937-103	5740410334419524864	17562	8.50	0.913	
WD0939-153	5685624040829463552	13900	7.77	0.503	
HS0940+1129	612988182140954240	15176	7.84	0.531	ambiguous
HS0943+1401	614643325098055680	16863	8.28	0.773	
HS0944+1913	627412945768300800	17444	7.88	0.559	
WD0945+245	643183348419998336	14500	8.5	0.909	primary, LBSS93
HS0949+0935	3878937457832171776	18357	7.69	0.49	
HS0949+0823	3877952432852336128	14755	7.81	0.518	
WD0950+077	3853660510143027200	15623	7.89	0.558	
WD0951-155	5686109578292348032	17973	7.83	0.534	
WD0954+134	614972658894818688	16462	7.68	0.479	
WD0955+247	642685200933153408	8456	7.75	0.482	
WD0956+045	3849176633005242624	18228	7.78	0.516	
WD0956+020	3834721387994870784	16495	7.81	0.521	
PG0959-085	3770623807170338304	101256	6.86	0.525	NEW/NLTE
WD1000-001	3833194887898568320	20253	7.80	0.529	
WD1003-023	3829366074878263168	20614	7.89	0.569	
HS1003+0726	3874412413432647680	9436	7.76	0.486	
WD1010+043	3860744010725801856	28617	7.90	0.594	
HE1012-0049	3830680854561582464	23204	8.07	0.667	
HS1013+0321	3859871342090899328	11781	7.83	0.521	
WD1013-010	3830623164560911872	8080	7.32	0.32	
WD1015-216	5666295485406677632	30937	7.89	0.593	
WD1015+076	3875365174618907264	27375	7.73	0.519	
WD1015+161	3888723386196630784	19948	7.92	0.585	
WD1017-138	3753200224361795968	31798	7.84	0.575	
WD1017+125	3883615188318129536	21386	7.88	0.565	
WD1019+129	3883746133280920448	18412	7.88	0.562	
WD1020-207	5667957225433304192	19920	7.93	0.585	
WD1022+050	3860381618565361024	14693	7.36	0.368	
WD1023+009	3831358664825312384	37817	7.65	0.519	
WD1026+023	3855631797052747136	12653	7.87	0.539	

Table C.2: Gaia DR2 IDs, effective temperatures, gravities and masses, continued.

object	Gaia DR2 ID	T_{eff} K	$\log g$ cm s^{-1}	M M_{\odot}	References/remarks
WD1031-114	3754712881779364992	25502	7.84	0.561	
WD1031+063	3862040300575181184	21317	7.76	0.516	
WD1036+085	3868927607051816320	22924	7.32	0.395	
HS1043+0258	3809362934711715712	13923	7.75	0.496	
WD1049-158	3557394009663078912	20037	8.28	0.778	
WD1053-550	5353122722363361920	14621	7.86	0.539	
WD1053-290	5453248339973753216	10669	7.83	0.515	
WD1053-092	3759722119317000448	22620	7.69	0.501	
HS1053+0844	3865978987449159168	16556	7.81	0.523	
WD1056-384	5393763111644515968	27974	7.90	0.59	
WD1058-129	3564376149017654272	23892	8.65	1.004	
HS1102+0934	3866880552624195584	16961	7.37	0.379	
WD1102-183	3552845261339955200	8076	7.68	0.451	
HS1102+0032	3804239558419007744	12959	8.13	0.681	
WD1105-048	3788194488314248832	15995	7.75	0.503	
HE1106-0942	3758930363570138880	72505	6.47	0.37	NEW/NLTE
HS1115+0321	3811876594386673408	14267	7.71	0.483	
WD1115+166	3970767638191849984	22090	8.12	0.69	primary, BL02
WD1116+026	3810933247769901696	12354	7.90	0.557	
HE1117-0222	3790471336376946304	14709	7.98	0.599	
WD1121+216	3978879594463069312	7434	8.19	0.705	GBD12, phot
WD1122-324	5402827451143222912	21671	7.86	0.556	
WD1123+189	3977128961497893760	58126	7.50	0.524	
HE1124+0144	3798659326454564224	16246	7.74	0.5	
WD1124-293	3482983495102507904	9353	7.83	0.514	
WD1124-018	3796545519645331584	23942	7.63	0.486	
WD1125-025	3787451081014802304	31755	8.16	0.729	
WD1125+175	3973707423046985984	61213	7.49	0.531	
WD1126-222	3541237717085787008	12006	7.88	0.545	
WD1129+071	3910382871911470848	14599	7.83	0.526	
WD1129+155	3966519331420622080	17739	8.03	0.632	
WD1130-125	3586028453547223552	14436	8.32	0.795	
HS1136+1359	3918029283792258304	23921	7.83	0.55	
HS1136+0326	3800633813114930688	14087	7.90	0.56	
WD1141+077	3910122047137575424	62493	7.55	0.551	
WD1144-246	3491591640356263424	30500	7.16	0.39	
HS1144+1517	3924401920043360896	15385	7.77	0.508	
WD1145+187	3974868644764927744	27167	7.80	0.545	
WD1147+255	4005438916307756928	9863	7.78	0.497	
WD1149+057	3897445571422443904	11108	7.85	0.527	
WD1150-153	3571559292842744960	12369	7.93	0.569	
HE1152-1244	3574739561506431104	13467	7.75	0.494	
WD1152-287	3480134832273157760	20620	7.63	0.476	
HS1153+1416	3923263135234800768	15553	7.79	0.512	
WD1155-243	3491050989871968768	14011	7.88	0.549	
WD1159-098	3575770010060921728	9232	8.27	0.756	
WD1201-001	3698872156539379968	19853	8.29	0.789	
WD1201-049	3597350571454888448	57260	7.62	0.556	GBR11
WD1202-232	3489719481290397696	8618	7.80	0.499	
WD1204-322	3466326581136347520	21263	8.00	0.623	
WD1204-136	3570694595665791232	10988	7.97	0.584	
HS1204+0159	3891718417216600448	24756	7.75	0.521	
WD1207-157	3569231970322760448	16885	7.78	0.512	
WD1210+140	3920848710779658880	32127	6.92	0.334	
WD1214+032	3701290326205270528	6295	6.84		
HE1215+0227	3701048502366477824	59691	7.59	0.555	
WD1216+036	3701701509194344576	14404	7.77	0.504	
WD1218-198	3514997902152549632	35013	7.91	0.611	
WD1220-292	3474544434120772736	17702	7.89	0.563	

Table C.2: Gaia DR2 IDs, effective temperatures, gravities and masses, continued.

object	Gaia DR2 ID	T_{eff} K	$\log g$ cm s^{-1}	M M_{\odot}	References/remarks
HE1225+0038	3696778892558087552	9340	7.83	0.512	
WD1229-012	3695495693769418112	19540	7.50	0.433	
WD1230-308	3470463802872604032	22764	8.28	0.784	
WD1231-141	3528008496258850560	17217	7.92	0.578	
HE1233-0519	3679712857186869504	15854	8.34	0.812	magnetic
WD1233-164	3523347735187987072	24892	8.21	0.745	
WD1236-495	6127333286605955072	11444	8.52	0.917	
WD1237-028	3682835848166848896	9885	8.15	0.683	
WD1241+235	3956176053739681664	26982	7.77	0.533	
WD1241-010	3683519503881169920	23459	7.38	0.414	
HS1243+0132	3702195464793095936	21644	7.82	0.539	
WD1244-125	3528847870307147136	14011	7.90	0.557	
HE1247-1130	3529574716212596736	28110	7.84	0.565	
EC12489-2750	3495397496775173248	61045	7.63	0.567	
HS1249+0426	3705386281897262848	11539	7.85	0.528	
WD1249+160	3931446491043126784	25792	7.21	0.379	
WD1249+182	3940955205038857728	19911	7.73	0.504	
HE1252-0202	3682458814461982592	15934	7.81	0.52	
WD1254+223	3944400490365194368	39537	7.59	0.51	
WD1257+047	3705070756419217408	21759	7.95	0.6	
WD1257+032	3692337037379978112	17579	7.81	0.526	
WD1257+037	3704392873140270336	5616	8.19	0.7	GBD12, phot
HE1258+0123	3690323316193465344	11387	7.77	0.497	
WD1300-098	3626022634955198592	15327	8.14	0.691	
HS1305+0029	3690709554012428416	14725	7.85	0.534	
WD1305-017	3685650597933742592	48200	7.83	0.603	NEW/NLTE
HE1307-0059	3685854179383579136	18191	7.91	0.572	
HS1308+1646	3936999437080327040	10732	7.99	0.598	
WD1308-301	6182607385393358848	14422	7.90	0.559	
HE1310-0337	3636072278607729920	18943	7.83	0.535	
WD1310-305	6182345731690327808	20353	7.82	0.536	
EC13123-2523	6192859060011793536	75463	7.68	0.612	
WD1314-153	3607725941130742528	16152	7.72	0.492	
WD1314-067	3628421666247974016	16832	7.85	0.54	
HE1315-1105	3623233040812235904	9047	7.83	0.513	
WD1323-514	6070021243006871040	19357	7.76	0.514	
HE1325-0854	3629976620502866944	17021	7.81	0.523	
HE1326-0041	3638786388700921472	18671	7.84	0.542	
WD1326-236	6194788080147917824	14029	7.91	0.563	
WD1327-083	3630035787972473600	14699	7.79	0.512	
HE1328-0535	3631829778632099328	36420	7.87	0.597	
WD1328-152	3604813197389660288	61253	7.72	0.593	
WD1330+036	3712812452150011648	17408	7.83	0.534	
WD1332-229	6195269769319451904	20264	7.86	0.555	
WD1334+039	-	4971	7.94	0.55	GBD12, phot
HS1334+0701	3718352444565698432	16891	7.27	0.353	
WD1334-160	3603920565746668032	18653	8.32	0.8	
WD1334-678	5850533227210203520	8761	7.67	0.451	
HE1335-0332	3634151534873010176	20188	8.47	0.896	
HS1338+0807	3724583445679765632	24440	7.65	0.493	
HE1340-0530	3632418223511334016	32936	7.91	0.606	
WD1342-237	6191268135405788544	11061	7.88	0.542	
WD1344+106	3725570772761744384	7059	8.09	0.644	GBD12, phot
WD1348-273	6177238676273826304	9787	7.78	0.495	
WD1349+144	3728966476985207936	19917	7.86	0.553	primary
WD1350-090	3618657732410663808	9261	7.94	0.565	magnetic
WD1356-233	6275184065428686464	9447	7.83	0.516	
WD1401-147	6301064404482150912	11955	7.94	0.573	
WD1403-077	3616104975648612608	49033	7.81	0.599	

Table C.2: Gaia DR2 IDs, effective temperatures, gravities and masses, continued.

object	Gaia DR2 ID	T_{eff} K	$\log g$ cm s^{-1}	M M_{\odot}	References/remarks
WD1410+168	1233014608793947776	21323	7.76	0.515	
HS1410+0809	3674476639217656576	16217	8.37	0.83	
WD1411+135	1227001444126009728	18562	8.11	0.677	
WD1412-109	6304590503913422464	26226	7.81	0.549	
HE1413+0021	3653928308787745792	14544	8.11	0.673	
HE1414-0848	3638957019161984640	11133	7.84	0.522	primary
WD1418-088	6329136310728635776	8024	7.75	0.478	
WD1420-244	6272562623549966208	20917	8.16	0.71	
WD1422+095	1176717792385803136	12905	7.84	0.528	
WD1426-276	6223132497775520512	18087	7.66	0.479	
HE1429-0343	3642258577702062720	11320	7.85	0.527	
HS1430+1339	1179764607826002688	9962	8.05	0.627	
WD1425-811	5772718006135360128	12305	7.83	0.521	
WD1431+153	1228266814506156928	14003	7.88	0.549	
HS1432+1441	1227992486355023616	16204	7.75	0.501	
WD1434-223	6278550873112595968	27690	7.37	0.431	
HE1441-0047	3650552739370519680	15775	8.03	0.626	
HS1447+0454	1158347014670132864	13991	7.82	0.519	
WD1448+077	1161215296909017728	14921	7.69	0.477	
WD1449+168	1188119762325721600	22346	7.79	0.526	
WD1451+006	3651184550535258496	25483	7.89	0.582	
WD1457-086	6332172027974304512	21448	7.92	0.584	
WD1500-170	6305900675097580800	31757	7.93	0.611	
WD1501+032	1154004081179409920	14741	7.93	0.576	
WD1503-093	6319913126159509888	13111	7.94	0.578	
WD1507+220	1261751715280478848	19872	7.75	0.509	
WD1507+021	4420242631507777920	20222	7.80	0.525	
WD1507-105	6318882711964895872	10031	7.40	0.356	
HE1511-0448	6335184655474717312	50899	7.45	0.497	
WD1511+009	4419865155422033280	28041	7.82	0.557	
WD1515-164	6259147585259050496	14248	7.97	0.593	
HS1517+0814	1163912467652160896	14494	7.76	0.501	
HE1518-0344	4413820521529120640	28493	7.81	0.552	
HE1518-0020	4415725940820061824	15392	7.82	0.523	
HE1522-0410	4401558183740868480	10320	7.86	0.531	
HS1527+0614	4429106481934491136	14925	7.77	0.505	
WD1527+090	1165354855109711232	21197	7.85	0.551	
WD1524-749	5792402116129561984	23091	7.74	0.515	
WD1531+184	1209640499120458752	13910	7.76	0.5	
WD1531-022	4403768373911022080	19234	8.35	0.824	
WD1532+033	4427107020039299968	61907	7.76	0.608	
WD1537-152	6265082680310200448	16954	7.94	0.586	
WD1539-035	4402583302239225600	9826	7.98	0.587	
WD1543-366	6009760034351291904	42701	8.97	1.176	
WD1544-377	6009537829925128064	10525	7.83	0.517	
WD1547+057	4426435871273922560	24355	8.36	0.831	
WD1547+015	4423116892346484480	76588	7.50	0.57	
WD1548+149	1192764133804981376	21452	7.86	0.557	
WD1550+183	1202826348825240832	14860	8.25	0.753	
WD1555-089	4347700805681797120	14531	7.94	0.582	
WD1609+135	4458207634145130368	9227	8.29	0.77	
WD1609+044	4437271867601913472	29593	7.79	0.548	
HS1609+1426	4464512882357505280	14387	7.82	0.522	
WD1614+136	4463466804419970304	22015	7.21	0.362	
WD1614+160	4465105351622152704	17961	7.82	0.528	
HS1614+1136	4454017257893306496	14137	7.98	0.599	
WD1614-128	4330093466990008448	16293	7.75	0.502	
WD1615-154	4328293291578459392	29465	8.03	0.656	
HS1616+0247	4436059415517432064	18468	7.96	0.597	

Table C.2: Gaia DR2 IDs, effective temperatures, gravities and masses, continued.

object	Gaia DR2 ID	T_{eff} K	$\log g$ cm s^{-1}	M M_{\odot}	References/remarks
WD1619+123	4460086458999242368	16853	7.68	0.483	
WD1620-391	6018034958869558912	24677	7.93	0.596	
WD1625+093	4452521234885949184	6410	7.40		
WD1636+057	4435778215414219520	8442	8.18	0.7	
WD1640+113	4447202622266019072	19718	7.85	0.551	
HS1641+1124	4447022061837071744	12323	7.87	0.537	
HS1646+1059	4447685097411960064	19890	7.78	0.52	
HS1648+1300	4449098970582483712	18693	7.79	0.519	
WD1655+215	4565048312887877888	9173	7.76	0.488	
HS1705+2228	4568179481487112832	15702	7.75	0.5	
WD1716+020	4387171623850187648	13787	7.64	0.458	
WD1733-544	5921433963191695872	6187	7.18		
WD1736+052	4485626636646013696	8830	7.80	0.501	
WD1755+194	4551645369227445888	24439	7.80	0.54	
WD1802+213	4576304838064664064	16787	7.64	0.47	
WD1821-131	4152557420406043264	6505	8.75		GBR11
WD1824+040	4284122782775063552	14787	7.46	0.398	
WD1826-045	4257461275049675008	9035	7.72	0.47	
WD1827-106	4154963942133386880	13726	7.56	0.428	ambiguous
WD1834-781	6364918198670588928	17723	7.77	0.513	
WD1840+042	4280632829779587072	8766	7.86	0.523	
WD1845+019	4279269469712040832	29941	7.92	0.602	primary
WD1844-223	4078868662206175744	32443	7.99	0.64	
WD1857+119	4313658585693385984	9821	7.74	0.483	
WD1911+135	4320094439580536320	14004	7.86	0.539	
WD1914+094	4309015794737134080	32525	7.85	0.579	
WD1914-598	6446197877766956800	19756	7.84	0.543	
WD1918+110	4309653752003973760	19268	7.81	0.529	
WD1919+145	4319908862597055232	15252	8.01	0.616	
WD1932-136	4183272552601606400	16931	7.73	0.497	
WD1943+163	1820678800523761152	19763	7.79	0.523	
WD1948-389	6690659513515872000	37199	7.75	0.55	
WD1950-432	6685284241684914688	40835	7.60	0.515	
WD1952-206	6865430941202657408	13814	7.81	0.517	
WD1952-584	6447181214823340800	33509	7.75	0.541	
WD1953-011	4235280071072332672	7868	8.23	0.731	GBD12, phot
WD1953-715	6422236358302245248	19267	7.87	0.559	
WD1959+059	4248931504366754304	10891	7.85	0.523	
WD2004-605	6443328221136801920	40994	8.39	0.873	
WD2007-219	6853784501721502720	9739	7.81	0.507	
WD2007-303	6749419923164242816	15436	7.80	0.518	
WD2014-575	6468623688724871808	26804	7.93	0.602	
WD2018-233	6849796229451135104	15585	7.81	0.52	
WD2020-425	6679362959252072832	34004	8.30	0.813	primary
WD2021-128	6876934409805839872	20753	7.82	0.538	
WD2029+183	1815528000815020288	13719	7.64	0.457	
WD2032+188	1815657193425348096	18199	7.36	0.381	
WD2039-202	6857939315643803776	19738	7.79	0.521	
WD2039-682	6424566979354709248	16943	8.34	0.81	
HS2046+0044	4228449385142100480	127096	8.15	0.718	
WD2046-220	6808699474099687808	23413	7.83	0.548	
WD2051+095	1750545141328217984	15274	7.79	0.513	
WD2051-208	6857295585945072128	16139	9.47	1.337	magnetic
HS2056+0721	1737897841324840832	27289	8.32	0.815	
WD2056+033	1731395432637342336	51835	7.70	0.565	
HS2058+0823	1738071701601163264	36844	7.78	0.56	
WD2058+181	1765090584946772736	17349	7.75	0.506	
HS2059+0208	1730310347805122816	18641	7.84	0.542	
WD2059+190	1789361097242243584	6237	6.90		

Table C.2: Gaia DR2 IDs, effective temperatures, gravities and masses, continued.

object	Gaia DR2 ID	T_{eff} K	$\log g$ cm s^{-1}	M M_{\odot}	References/remarks
HS2108+1734	1788040794231829376	28812	8.31	0.81	
WD2105-820	6348672845649310464	10263	7.88	0.538	magnetic
WD2115+010	2691277330022787712	25815	7.75	0.523	
WD2115-560	6462911897617050240	9575	7.75	0.483	
WD2120+054	1738521539295354240	35559	7.68	0.521	
WD2122-467	6575491133702739584	16334	8.05	0.643	
WD2124-224	6828157565735439232	47780	7.71	0.56	
HS2130+1215	1769941011771984768	32995	7.74	0.534	
HS2132+0941	1742342784582615936	13480	7.70	0.476	
HE2133-1332	6842831888437047680	9810	7.53	0.4	
WD2134+218	1793946026371051648	18001	7.86	0.551	
WD2136+229	1794118516552814336	10040	7.80	0.503	
HE2135-4055	6578616598584224640	19211	7.96	0.6	
WD2137-379	6585878288771383296	21013	7.86	0.555	
HS2138+0910	1741417790361772160	9228	7.61	0.429	
WD2139+115	1766702297192943488	15551	7.79	0.515	
HE2140-1825	6836795672680406272	13984	7.75	0.496	
WD2146-433	6565941703417200128	62792	7.23	0.48	
HS2148+1631	1772852278044283904	16776	7.79	0.517	
HE2148-3857	6585056369469080448	26758	8.02	0.644	
WD2149+021	2693940725141960192	17926	7.86	0.55	
WD2150+021	2693914886618675456	40874	7.66	0.525	
WD2152-045	2670147461020069632	19837	7.38	0.397	
WD2151-307	6616313457820826496	28580	8.27	0.789	
WD2152-548	6461145119869641728	45171	7.88	0.617	
WD2153-419	6572442909513784576	46503	7.94	0.645	
WD2154-061	2668622270889053568	36259	7.74	0.545	
HE2155-3150	6615959586875261056	16302	7.83	0.532	
WD2157+161	1775640227215432320	19188	7.89	0.566	
HE2159-1649	6826770115204739072	19486	7.84	0.544	
WD2159-414	6571754443436630272	54343	7.71	0.575	
WD2200-136	2612442135856683648	25261	7.52	0.462	primary
WD2159-754	6358158435541361792	8903	8.36	0.815	
HE2203-0101	2677321641247692032	18047	7.87	0.555	
WD2204+070	2721868041314138240	24454	7.95	0.607	
WD2205-139	2612155476855186176	25231	8.25	0.768	
WD2207+142	2735175263041913088	7255	7.49	0.369	
HE2209-1444	2600033326799287296	8471	7.62	0.429	primary
HS2210+2323	1879147564661258240	23233	8.24	0.76	
WD2211-495	6560067493827212544	62336	7.54	0.548	
HS2216+1551	2735823425146356224	19163	8.04	0.638	primary
HE2218-2706	6621832284637642240	15039	7.79	0.514	
HE2220-0633	2625750938132516224	15523	7.88	0.555	
HS2220+2146B	1874954645786146304	14601	8.24	0.755	K09
HS2220+2146A	1874954641491354624	18743	8.08	0.653	K09
WD2220+133	2734319087081051264	22583	8.30	0.795	
HE2221-1630	2595728287804350720	9889	7.89	0.545	
HS2225+2158	1874832084599745920	25989	7.86	0.567	
WD2226+061	2709363196787375488	16429	7.66	0.472	
WD2226-449	6520516480027596288	13974	7.74	0.493	
HS2229+2335	1875647956587976576	19300	7.90	0.571	
HE2230-1230	2601689466188247808	20949	7.81	0.532	
HE2231-2647	6621374578563035776	21592	7.70	0.5	
HS2233+0008	2654170736729886976	24529	7.99	0.626	
WD2235+082	2716039358376761088	36519	7.73	0.542	
HE2238-0433	2625067484281097856	17542	8.18	0.716	
HS2240+1234B	2731502443233585280	15636	7.86	0.542	J98, WD2240+125A
HS2240+1234A	2731501687319341568	14022	7.99	0.601	J98, WD2240+125B
WD2240-045	2625078449333017856	44102	7.72	0.556	

Table C.2: Gaia DR2 IDs, effective temperatures, gravities and masses, continued.

object	Gaia DR2 ID	T_{eff} K	$\log g$ cm s^{-1}	M M_{\odot}	References/remarks
WD2240-017	2652784694950778624	9090	7.78	0.493	
WD2241-325	6603807092875065728	32316	7.95	0.621	
HS2244+2103	2836176779127265792	24113	7.89	0.578	
HS2244+0305	2656542452030717952	60460	7.54	0.542	
HE2246-0658	2611423167751076224	11512	7.99	0.601	
WD2248-504	6514042654346344704	16336	7.74	0.498	
HE2251-6218	6394778525002127104	18033	7.83	0.534	
WD2253-081	2610488514148351360	6233	6.85		
WD2253+054	2711324446359728384	6244	8.64		GBR11
WD2254+126	2719012579552367488	11893	7.85	0.529	
HS2259+1419	2816082757452460416	13057	7.77	0.502	ambiguous
WD2303+017	2658537614663492352	40977	7.67	0.528	
WD2303+242	2842650153836732928	11261	7.83	0.517	
WD2306+130	2814942392095501952	13955	7.81	0.516	
WD2306+124	2811882073278282496	20360	7.99	0.619	
WD2308+050	2662658107503521536	36062	7.61	0.507	
WD2309+105	2810585920868186240	57007	7.82	0.617	
WD2311-260	2379935013296113664	51160	7.77	0.589	
WD2312-356	6554999363696189056	15122	7.82	0.522	
WD2314+064	2664365374183501312	17981	7.88	0.556	
HE2315-0511	2633791288709297792	33451	7.72	0.529	
WD2318+126	2811363550466857344	13965	7.80	0.512	
WD2318-226	2385336982642954496	29851	7.89	0.591	
WD2321-549	6499376994593401344	43583	7.78	0.577	
WD2322+206	2825795087259417984	13026	7.79	0.508	
WD2322-181	2393546245693497728	21683	7.90	0.577	
WD2324+060	2661500871515095680	16261	7.83	0.529	
WD2326+049	2660358032257156736	11658	7.90	0.552	
WD2328+107	2762605088857836288	22390	7.78	0.523	
WD2329-332	2325117757286653440	20457	7.91	0.581	
WD2330-212	2388953031573382784	26442	7.44	0.445	
WD2331-475	6528109879126984960	51573	7.88	0.629	
WD2333-165	2395444208921491456	13791	7.84	0.529	
WD2333-049	2633120655335891968	10602	7.79	0.503	
HE2334-1355	2432056468657830784	30498	7.29	0.421	
WD2336-187	2393875961742886656	7810	7.46	0.362	primary
WD2336+063	2756675044691990272	17012	8.03	0.629	
MCT2343-1740	2394370123500185344	21827	7.88	0.569	
HE2345-4810	6524412152806190336	29352	7.32	0.425	
MCT2345-3940	6534665545408513792	19197	7.87	0.555	
WD2347+128	2769930207121379968	10933	7.79	0.501	
WD2347-192	2390888829168611968	26272	7.94	0.606	
HE2347-4608	6530721803358467968	17738	7.30	0.366	
WD2348-244	2338349628107880192	11567	7.86	0.534	
MCT2349-3627	2311200968031379584	44455	7.88	0.615	
WD2349-283	2334079090586541440	17427	7.73	0.499	
WD2350-248	2338275136195124864	28867	8.38	0.849	
WD2350-083	2442099751463686528	18529	7.79	0.52	
WD2351-368	2310942857676734848	14438	7.87	0.544	
MCT2352-1249	2421871039614828672	40294	7.95	0.64	
WD2353+026	2739782629080048000	61740	7.59	0.558	
WD2354-151	2419140746085234688	34984	7.20	0.414	
HE2356-4513	6530974072557448064	17418	7.86	0.548	